

UC San Diego

UC San Diego Electronic Theses and Dissertations

Title

Topological Photonics Light Sources

Permalink

<https://escholarship.org/uc/item/5p5941xw>

Author

Bahari, Babak

Publication Date

2019

Peer reviewed|Thesis/dissertation

UNIVERSITY OF CALIFORNIA SAN DIEGO

Topological Photonics Light Sources

A dissertation submitted in partial satisfaction of the requirements for the
degree Doctor of Philosophy

in

Electrical Engineering (Photonics)

by

Babak Bahari

Committee in charge:

Professor Boubacar Kanté, Chair
Professor Yeshaiahu Fainman
Professor Eric Fullerton
Professor George Papen
Professor Justin Roberts
Professor Ivan Schuller

2019

Copyright
Babak Bahari, 2019
All rights reserved.

The dissertation of Babak Bahari is approved, and it is acceptable in quality and form for publication on microfilm and electronically:

Chair

University of California San Diego
2019

DEDICATION

*To my parents, who are the soul of my life and to
my wife, who gave the actual meaning to my life.*

EPIGRAPH

Never give up without any try

—Babak Bahari

TABLE OF CONTENTS

Signature Page.....	iii
Dedication.....	iv
Epigraph.....	v
Table of Contents.....	vi
List of Figures.....	x
Acknowledgements.....	xv
Vita.....	xx
Abstract of the Dissertation.....	xxiii
Chapter 1: Overview	1
1.1. Introduction	1
1.2. Topological Insulators	3
1.3. Bound States in the Continuum.....	4
1.4. Scope of This Thesis	7
References	9
Chapter 2: 2D Topological Cavity.....	12
2.1. Introduction	12
2.2. Berry Phase, Berry connection, and Chern Number	14
2.3. Topological Waveguide Design	17
2.4. Topological vs Non-topological Cavity	20
2.5. Chapter Summary	24
References	25
Chapter 3: Topological Laser	28
1.1. Introduction	28
3.2. Design of topological cavities	30

3.2.1. Band Diagram Calculation	31
3.2.2. Trivial and Non-trivial Waveguides.....	33
3.3. Device Fabrication.....	37
3.4. Device Characterization	41
3.4.1. Field Intensity Imaging	41
3.4.2. Photoluminescence Measurement.....	42
3.5. Geometry-independent Cavities	46
3.5.1. Far-field Intensity Imaging.....	47
3.5.2. Photoluminescence Measurement.....	48
3.6. Chapter Summary	49
References	51
Chapter 4: Topological OAM.....	53
4.1. Introduction	53
4.2. Theoretical Design of Topological Rings	55
4.3. Device Fabrication.....	59
4.4. Device Characterization	60
4.4.1. Far-field and Interference Imaging	61
4.4.2. Photoluminescence Measurement.....	62
4.4.3. Second Order Correlation Measuring	62
4.4.4. Full Wave Half Maximum Measuring	65
4.5. Multiplexing Multiple Topological Rings.....	68
4.6. Chapter Summary	72
References	74
Chapter 5: Bound States in the Continuum	78
5.1. Introduction	78
5.2. Theoretical Design of Extended PhC Cavity	82
5.2.1. Band Diagram Calculation	84
5.2.2. Vortex Behavior of BIC Singularities.....	85
5.2.3. Robustness of BIC Singularities	87

5.3. Device Fabrication and Characterization	88
5.4. Device Characterization	89
5.4.1. Photoluminescence Measurement	89
5.4.2. Band Diagram Characterization	90
5.4.3. Steering behavior.....	91
5.4.4. Polarization Vortex	93
5.4.5. Topological Charge Conservation.....	94
5.4.6. Wavelength Scaling.....	96
5.5. Chapter Summary	97
References	99
Chapter 6: Summary and Outlook	102
Appendix 1	106
A1.1. Other Arbitrary Geometry Cavities	106
A1.2. Field Intensity Imaging.....	106
A1.3. Photoluminescence Measurement	107
Appendix 2.....	110
A2.1. Second Order Correlation Measurement.....	110
References	112
Appendix 3.....	113
A3.1. Vortex Behavior of BIC Singularities	113
Appendix 4.....	116
A4.1. Rigorous Coupled Wave Analysis (RCWA).....	116
Reference.....	124
Appendix 5.....	125
A5.1. Experiment Setup	125
A5.2. Effective Mode Gain	126
A5.3. Far-field Patterns	127
Appendix 6.....	129

A6.1. Controlling the Number of beams using Boundaries	129
--	-----

LIST OF FIGURES

Figure 1-1 Illustration of the adiabatic and non-adiabatic processes. In an adiabatic process, a wave (or generally a particle).	2
Figure 1-2 Representative dispersion band of a topological insulator, showing Dirac dispersing surface states lying in the bulk.....	4
Figure 1-3 Schematic demonstration of bound states for a structure in space. By exciting the mode of structure (red), if the excitation.....	5
Figure 2-1 (a) Schematic of the star-shaped unit cell of a PhC with square lattice that is periodic in two directions with the p , b , and	18
Figure 2-2 (a) Schematic of the unit cell of PhC with an air hole and a triangular lattice. The periodicity and radius of the holes.	19
Figure 2-3 (a) Schematic of an edge waveguide formed by placing non-trivial and trivial PhCs next to each other..	20
Figure 2-4 (a) Schematic of a topologically trivial PhC cavity made of triangular PhC. Cavity and waveguide are formed.....	21
Figure 2-5 (a,b) Normalized field intensity map inside the cavity when excited from both ends at the resonance frequency	22
Figure 2-6 (a) Schematic of a topologically non-trivial PhC cavity made of a non-trivial PhC as a core of the cavity and a trivial.....	23
Figure 2-7 (a-c) Normalized field intensity profile inside the cavity when it is excited from both ends of the waveguide with a frequency.....	24
Figure 3-1 Schematic of an arbitrarily-shaped and integrated topological cavity. The topological structure is an arbitrarily-shaped.....	30
Figure 3-2 (a) Schematic of a PhC with a star-shaped unit cell and a square lattice. The dimensions of the unit cell are $p=1084$ nm.....	32
Figure 3-3 (a) Schematic of a PhC with cylindrical air holes unit cell and a triangular lattice. The periodicity, p' , and radius of	33
Figure 3-4 Edge waveguide formed by two trivial and non-trivial PhCs. Edge mode is excited using a point source (S) located.....	34

Figure 3-5 Electric (a-c) and magnetic (d-f) fields intensity distribution inside the edge waveguide. Dominant field components.	35
Figure 3-6 Full wave three-dimensional simulations of non-trivial (a) and trivial (b) waveguides. The waveguides	36
Figure 3-7 (a) Full-wave simulation of a supercell consisting of seven trivial and six non-trivial unit cells in one	37
Figure 3-8 Flow chart of the fabrication. Step 1: InGaAsP MQWs wafer. Step 2: Removal of the protective layer	39
Figure 3-9 Top view SEM of a fabricated squared-shaped topological cavity where the trivial and non-trivial.....	41
Figure 3-10 Real space camera images of the top of the device without (a) and with (b) EMF under optical pumping using a laser with a.....	42
Figure 3-11 Emission spectra of the square cavity when it is pumped with the pump power density of.....	43
Figure 3-12 Photoluminescence spectrum of the square cavity when the EMF is (a) $B_0 = +100 Oe$, and (b).....	44
Figure 3-13 (a) Evolution of the output power collected by a lensed fiber coupled to the output of the trivial	45
Figure 3-14 Top view SEM of a fabricated topological cavity with a random geometry formed by the trivial and.....	47
Figure 3-15 Real space camera images of the top of the device with (a) and without (b) EMF under optical pumping	47
Figure 3-16 Photoluminescence spectrum of the square cavity when the EMF is (a) $B_0 = +100 Oe$, and (b) $B_0 = -100 Oe$	48
Figure 3-17 (a) Evolution of the output power as a function of the pump power density (light-light curve) for the.....	49
Figure 4-1 Schematic of a topological ring formed at the interface of two PhCs. Both PhCs are patterned on	57
Figure 4-2 (a) Schematic of a ring-resonator of radius a . The propagating mode can be in-plane or out-of-plane	58
Figure 4-3 (a) Field intensity profile of an OAM mode with $\ell = 100$. (b) The interference pattern of two OAM beams	59

Figure 4-4 Top view SEM of a topological ring formed by trivial and non-trivial PhCs. The structure is fabricated.....	60
Figure 4-5 (a) Real-space camera image of the emission from the topological ring when it is optically pumped from the top with.....	61
Figure 4-6 (a) Photoluminescence of the topological ring for three different pump powers as a function of the	62
Figure 4-7 Second-order intensity correlation at the zero-delay, $g_2(0)$. Clearly, the photon bunching peak	63
Figure 4-8 Intensity correlation histograms (a-e), and the corresponding normalized $g_2(\tau)$ (f-j) in the SpE,.....	65
Figure 4-9 The pulse FWHM of the topological device is plotted along with that of the pump laser. Evidently, the $g_2(\tau)$	68
Figure 4-10 Schematic of a topological multiplexer formed by placing three different topological rings in which trivial and.....	69
Figure 4-11 Top view SEM images of three different topological rings designed for topological charges of	70
Figure 4-12 (a-c) Real-space camera images of the rings when they optically pumped with an optical pump power.....	71
Figure 4-13 Field intensity profile of the beam when it interferes with an OAM beam with the opposite ℓ number ($-\ell$).....	72
Figure 4-14 Field intensity profile of the beam when it interferes with an OAM beam with the opposite ℓ number ($-\ell$).....	72
Figure 5-1 schematic of 1D, 2D, and 3D PhCs.	79
Figure 5-2 (a) schematic of PhC slab with different configurations of either rod-base or hole-base, and different.....	80
Figure 5-3 schematic of the PhC slab made of InGaAsP MQWs bonded on a glass substrate using a PMMA resist.	84
Figure 5-4 Band diagram (a) and quality factor (b) of the square lattice PhC with a periodicity of $p = 950 \text{ nm}$, and radius.....	85
Figure 5-5 (a) Polarization map of the PhC within the Brillouin zone at different momentum pairs (k_x, k_y) . At each point.....	86

Figure 5-6 Quality factor of modes 1-3 as a function of the radius of holes in reciprocal space (k-space). The quality factors of	88
Figure 5-7 (a) Microscope image of the fabricated PhC arrays. The sample contains different 200×200 arrays with the radii	89
Figure 5-8 (a) The emission power evolution as a function of the pump power in a broader wavelength range for a sample with a	90
Figure 5-9 Experimental (color plot) and theoretical (blue dots) band diagrams measured/calculated along the ΓX	91
Figure 5-10 Experimental k-space images of the emission from lasers with different radii. The distance of the bright	92
Figure 5-11 Far-field radiation pattern measurements (a-c) and corresponding simulations (d-f) of the	94
Figure 5-12 Reciprocal space images of the vortex laser when the only mode lasing is the one beaming along ΓX	96
Figure 5-13 Lasing wavelength as a function of the radius of holes from 180 nm to 350 nm. Each point corresponds to a.....	97
Figure A1-1 (a,b) Top view SEM of a fabricated topological cavity with random geometry formed by the trivial and.	106
Figure A1-2 IR camera image of two different cavities with arbitrary shapes shown in Fig. A1-1a (a), and Fig. A1-1b (b).	107
Figure A1-3 Emission spectra of the cavity shown in Fig. A1-1a with an EMF of $B_0 = +100 Oe$ (a),	108
Figure A1-4 Emission spectra of the cavity shown in Fig. 3-18b with an EMF of $B_0 = +100 Oe$ (a), and.....	109
Figure A3-1 Quality factor map in the Brillouin zone for modes 1 (a), 2 (b), and 3 (c). For the simulation,	113
Figure A3-2 Far-field patterns of the (a) mode 1, and (b) mode 3. To calculate the far-field profile, we extracted the.....	115
Figure A4-1 (a) Dispersion band diagram and (b) quality factor of the PhC when the periodicity and radius of holes.	123
Figure A4-2 Fourier coefficients of the mode 1 at Γ point. Amplitudes and phases of the dominant Floquet-Bloch.....	123

Figure A4-3 Fourier coefficients of the mode 3 at BIC singularity along ΓX direction. Amplitudes and phases of	124
Figure A4-4 Fourier coefficients of the mode 3 at a non-BIC point along ΓX direction. Amplitudes and phases	124
Figure A5-1 Schematic of the set-up used for measurements. The incident pump power on the samples is finely	126
Figure A5-2 (a) Gain spectrum measurement of the unpatterned InGaAsP, bonded on a glass substrate using PMMA,	127
Figure A5-3 Far-field measurements of two different arrays with radii of (a) 250 nm, and (b) 225 nm. To measure the	128
Figure A6-1 SEM image of arrays with dimensions of (a) 10×200 , (b) 15×200 , and (c) 25×200	130
Figure A6-2 Reciprocal space measurement for finite arrays with dimensions of (a) 10×200 , (b) 15×200 , and.....	131

ACKNOWLEDGMENTS

Finally, I arrived. At this moment, I should thank many people that helped me to finish this important chapter of my life. I am very delighted that I spent my PhD here at the University of California San Diego (UCSD), which is one of the best schools in the world. I learned many things at UCSD, and had a very joyful life with many ups and downs at San Diego, which ended up with making me stronger and more knowledgeable, with more valuable life and academic experiences.

First, I would like to thank Prof. Boubacar Kanté for all he gave me. He spent countless times to guide and show me the right direction of doing research, and supported me in every single step of my PhD. I learned from him to be ambitious and have big dreams in science to achieve the best results. During all this time, our relationship was more like two friends. It was a great honor to me to work with him, and I am quite sure that we will keep this relation forever.

I also would like to thank my committee members and collaborators. Prof. Yeshaiahu Fainman and his group members, especially, Dr. Felipe Valini, Si Hui Pan, and Dr. Abdelkrim El Amili for all supports and contributions at different stages of my research. Prof. George Papen for many things. First of all, for the great course on laser physics that broadened my

insight in the laser realm. Second, for fruitful discussions about my research and sharing all his experiences eagerly. Prof. Eric Fullerton for having key conversations on processing magnetic materials, and introducing many useful references that saved quite a lot of my time. Prof. Ivan Schuller for decisive comments on my research that helped to improve the quality of my thesis. Finally, Prof. Justin Roberts for having a great discussion about topology, and letting me to know a mathematician's vision about topology. For sure, all of those insights helped me to better understand the concept of topology.

I want to especially thank my colleague and friend, Dr. Abdoulaye Ndao, for helping me to do my PhD with a very high quality factor! I also like to thank all my colleagues in our group: Dr. Thomas Lepetit, Prof. Qing Gu, Dr. Ricardo Tellez-Limon, Dr. Matthieu Dupre, Dr. Hadiseh Nasary, Dr. Quynh Le Van, Dr. Ashok Kodigala, Li-Yi Hsu, Junhee Park, Jeongho Ha, Wanwoo Noh, Zhetao Jia, Rushin Contractor, and Mutasem Ayed Odeh. All of the researches that I have involved and published papers were as a result of team works. Definitely, without the help of my colleagues, I could not have any of those accomplishments. Part of these team works are nano3 staff, Bernd Fruhberger, Dr. Maria Isabel Montero Ramirez, Larry Grissom, Ivan Harris, Ryan Anderson, Sean Parks, and Dr. Xuekun Lu. I thank all of them for their

assist in the cleanroom, which helped me to fabricate all of the chips used in my thesis.

I want to thank my collaborator, Prof. Daryl Preece, for fruitful discussions and sharing his experiences on structured light.

I would like to thank Julie Moritz for helping me whenever I need any assist.

In the United States, I have many friends that helped me in different situations. I thank all of them. But I would like to especially thank my very close friends Mohsen Imani and his wife, Haleh Alimohammadi. Both of them are kind of like my family here in the US that always support me and they are available whenever I need them.

Finally, and the most important one, I would like to deeply thank my family, my parent, who are the soul of my life, my grandparents, brothers, and especially my lovely wife. Whatever I have is because of them, and their non-stop support. All my accomplishments are indeed from them, and if I have any achievement is dedicated to them.

Chapter 2, in part, is a reprint of the material as it appears in B. Bahari, A. Ndao, F. Valini, A. E. Amili, Y. Fainman, and B. Kanté, “Experimental

demonstration of non-reciprocal lasing in topological cavities of arbitrary geometries,” *Science* 358, 636-640 (2017). The dissertation author was the primary researcher and author of this paper.

Chapter 3, in part, is a reprint of the material as it appears in B. Bahari, A. Ndao, F. Valini, A. E. Amili, Y. Fainman, and B. Kanté, “Experimental demonstration of non-reciprocal lasing in topological cavities of arbitrary geometries,” *Science* 358, 636-640 (2017), and B. Bahari, and B. Kanté, “Experimental demonstration of non-reciprocal lasing in topological cavities of arbitrary geometries,” United States patent (US Provisional Patent Application No. 62/540,809), 2017. The dissertation author was the primary researcher and author of this paper and patent.

Chapter 4, in part, is a reprint of the material as it appears in B. Bahari, L. Hsu, S. H. Pan, D. Preece, A. Ndao, A. El Amili, Y. Fainman, and B. Kanté, “Topological lasers generating and multiplexing topological light,” *arXiv:1904.11873* (2019), and B. Bahari, and B. Kanté, “Topological integration of unbounded orbital angular momentum laser,” United States patent (Under process), 2018. The dissertation author was the primary researcher and author of this paper and patent.

Chapter 5, in part, is a reprint of the material as it appears in B. Bahari, F. Vallini, T. Lepetit, R. Tellez-Limon, J. Park, A. Kodigala , Y. Fainman, and B. Kanté, “Integrated and steerable vortex lasers using bound states in continuum,” *arXiv:1707.00181* (2017), and B. Bahari, and B. Kanté, “Photonic generation and steering of coherent vortex beams,” United States patent (US Provisional Patent Application No. 62/506,765), 2016. The dissertation author was the primary researcher and author of this paper and patent.

VITA

- 2019 Doctor of Philosophy, Electrical Engineering (Photonics), University of California San Diego, USA
- 2014 Master of Science, Electrical Engineering (Fields and Waves), University of Tehran, Tehran, Iran
- 2011 Bachelor of Science, Electrical Engineering (Fields and Waves), Khajeh Nasir University of Technology, Tehran, Iran

JOURNAL PUBLICATIONS

1. **B. Bahari**, A. Ndao, F. Valini, A. E. Amili, Y. Fainman, and B. Kanté, “Experimental demonstration of non-reciprocal lasing in topological cavities of arbitrary geometries,” *Science* **358**, 636-640 (2017).
2. A. Kodagala, T. Lepetit, Q. Gu, **B. Bahari**, Y. Fainman, and B. Kanté, “Lasing Action from Photonic Bound States in the Continuum,” *Nature* **541**, 196-199 (2017).
3. A. Kodagala, Q. Gu, T. Lepetit, **B. Bahari**, and B. Kanté, “Mechanically Stable Conjugate and Suspended Lasing Membranes of Bridged Nano-Cylinders,” *Optical Materials Express* **7**, 2980-2992 (2017).
4. **B. Bahari**, R. Tellez-Limon, and B. Kanté, “Topological THz Circuits using Semiconductors,” *Applied Physics Letters* **109**, 143501 (2016).
5. J. Li, W. Liu, T. Li, I Rozen, J. Zhao, **B. Bahari**, B. Kanté, and J. Wang, “Swimming Micro-Robot Optical Nanoscopy for Sub-Diffraction Imaging,” *Nano Letters* **16**, 6604-6609 (2016).
6. **B. Bahari**, R. Tellez-Limon, and B. Kanté, “Directive and Enhanced Spontaneous Emission using Shifted Cubes Nanoantenna,” *Journal of Applied Physics* **120**, 093106 (2016).
7. R. Tellez-Limon, **B. Bahari**, Hsu Li, J. Park, A. Kodigala, and B. Kanté, “Integrated metaphotonics: symmetries and confined excitation of LSP resonances in a single metallic nanoparticle,” *Optics Express* **24**, 13875-13880 (2016).
8. **B. Bahari**, L. Hsu, S. H. Pan, D. Preece, A. Ndao, A. El Amili, Y. Fainman, and B. Kanté, “Topological lasers generating and multiplexing topological light,” *arXiv:1904.11873* (2019).
9. **B. Bahari**, F. Vallini, T. Lepetit, R. Tellez-Limon, J. Park, A. Kodigala, Y. Fainman, and B. Kanté, “Integrated and steerable vortex lasers using bound states in continuum,” *arXiv:1707.00181* (2017).

Patents

1. **B. Bahari**, and B. Kanté, “Topological integration of unbounded orbital angular momentum laser,” United States patent (Under process), 2018.
2. **B. Bahari**, and B. Kanté, “Experimental demonstration of non-reciprocal lasing in topological cavities of arbitrary geometries,” United States patent (US Provisional Patent Application No. 62/540,809), 2017.
3. **B. Bahari**, and B. Kanté, “Photonic generation and steering of coherent vortex beams,” United States patent (US Provisional Patent Application No. 62/506,765), 2016.

ABSTRACT OF THE DISSERTATION

Topological Photonics Light Sources

by

Babak Bahari

Doctor of Philosophy in Electrical Engineering (Photonics)

University of California San Diego, 2019

Professor Boubacar Kanté, Chair

In integrated photonics, cavity resonators play an important role. They are the basis of light sources, which are one of the fundamental building blocks of any integrated circuit. So far, cavities are designed base on their size, shape, and photon lifetime, and requiring any extra features increase their complexity. However, cavities can present some topological behaviors with peculiar characteristics that can enhance their functionalities. Two of these topological behaviors, which are the main focus of this thesis, are Topological

insulators (TIs), and Bound states in the continuum (BIC). In the following thesis, we explored theoretically and experimentally the topological singularities in cavities made of periodic structures, and their applications in designing integrated light sources (i.e., lasers). Structures are constructed on a gain material of InGaAsP multiple quantum wells, which emits in the telecommunication wavelength range ($\lambda \sim 1.55 \mu m$), and operates at room temperature.

In the first part of the thesis, we study TIs and design topological cavities for integrated light sources using hybrid photonic crystals (PhCs) with non-zero phase transition between them. Thus the optical wave is fully confined at the boundary of PhCs, and propagates in one direction. The topological cavities can have any arbitrary geometry while preserving high functionality. Furthermore, we demonstrate that topological cavities are able to be used to generate structured lights with very large topological charges, while they maintain small foot-print and no-complexity.

The second part is dedicated to the bound states, which are the type of topological singularities with positive energies in the continuum region. These topological singularities offer many unique characteristics such as tunability of their position in the reciprocal space and carrying non-zero topological charges. Furthermore, the number of singularities can be controlled by crystal

symmetry. In this thesis, we present the first experimental demonstration of simultaneously generation and steering multiple vortex beams from an extended PhC cavity.

Our results indicate the application of the topological behavior of cavities as an extra degree of freedom in designing integrated photonic chips with enhanced functionalities.

Chapter 1: Overview

1.1. Introduction

It is over a century that field of quantum mechanics has been developed. In 1980s Berry pointed out a feature that had been observed before that time, which was related to the existence of a topological phase factor that can arise in certain applications of the adiabatic theorem [1]. However, this phase factor had been discovered by Pancharatnam back in 1956 [2], but it was generalized by Berry in 1984 [3]. This topological phase factor is also known as geometrical phase, Pancharatnam–Berry phase, Pancharatnam phase, or Berry phase.

But what is this topological phase factor? Every electromagnetic wave is defined by an amplitude and a phase (for now, we are narrowing down to the electromagnetics, but it is general and can be in the other systems like electron particles). This (geometric) phase happens when both parameters are changed adiabatically and ultimately turn back to the initial state. In quantum mechanics, this is done by rotation or even translation of particle. Since the electromagnetic wave is returned to its initial state, it is expected that wave be similar to its starting point. However, if the parameters correspond to a loop instead of self-tracking cyclic vibration, then it is possible that initial and final

states have different phases (Fig. 1-1). The phase difference between the two states is called Berry phase, and it typically indicates that there are some singularities in the system (normally phase singularities) that causes this jump in the phase.

In the last decades, many researchers studied this phenomenon in different systems and using various techniques, and a wide range of problems have been discussed in particle physics and quantum field of theory, condensed matter physics, atomic and molecular physics, etc. [4]. They tried to address fundamental questions using these (geometrical or topological) singularities aiming to discover a new generation of devices useful many applications. Two of the interesting topological singularities are called

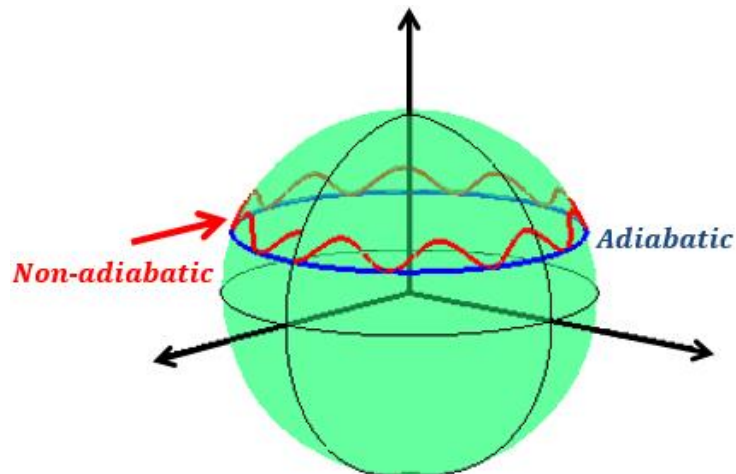


Figure 1-1 | Illustration of the adiabatic and non-adiabatic processes. In an adiabatic process, a wave (or generally a particle) returns to its initial state after a cycle. However, in a non-adiabatic process, the final state of the wave is different from the initial state when returning to the starting point, and wave experiences an extra geometrical (or Berry) phase.

“Topological insulators”, and “Bound states in the continuums” that have attracted many attentions, which are also the main scope of the present thesis.

1.2. Topological Insulators

Topological insulators (TIs) are materials with non-trivial anti-symmetric topological orders that behave as an insulator in their interior but conductor at their surface [5-11] (Fig. 1-2). However, having a conducting surface is not unique to TIs, because ordinary band insulators can also support conductive surface states. The important difference is that the surface states in TIs are symmetry protected and back-scattering is forbidden [12-16]. This is quite different from a material with broken time-reversal symmetry, e.g., magnetic materials, where the backward propagating states exist and back-scattering can happen during different processes. Therefore, in TIs propagating wave is robust to any kind of disorders, making them appealing to explore new devices and applications based on TIs.

This unique robust unidirectional wave propagation in topological systems gives us the ability to design topological components like cavity resonators, a fundamental piece of elements in many integrated photonic circuits. As a result, topological cavities can have arbitrary shapes while maintaining their functionalities. A brilliant idea is when implement

topological cavities using active materials to design topological light sources that can also take any arbitrary geometrical form while they emit coherent lights in one direction without using an optical isolator. The first part of the thesis will be dedicated to this topic.

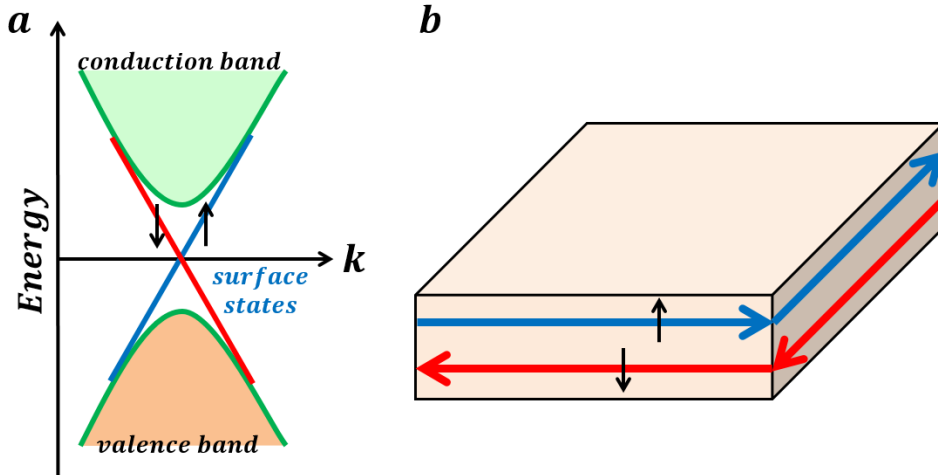


Figure 1-2 | Representative dispersion band of a topological insulator, showing Dirac dispersing surface states lying in the bulk band gap (a) with surface states on the bulk material (b).

1.3. Bound States in the Continuum

In quantum mechanics, there is an area discussing quantum states of particles that are placed in a potential domain as particles remain localized in some regions of space while they should not be [17,18]. Therefore, negative energy states are bounded and their potential vanish at infinity. These quantum states, which have discrete spectrum rather than continuous, are called bound states (Fig. 1-3).

Generally, bound states are metastable states with a net positive interacting energy, but there are some states with a very long decay time that are often considered as unstable bound states, and they are called quasi-bound states [18]. These types of singularities can happen in various systems such as single particle, random coupled particles, periodic structures, etc., but in the present thesis, we are specifically focusing on periodic structures.

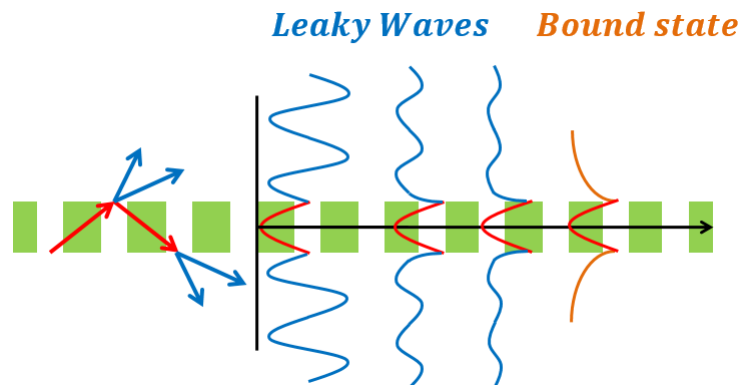


Figure 1-3 | Schematic demonstration of bound states for a structure in space. By exciting the mode of structure (red), if the excitation energy is in the continuum region, then there are some radiation in the continuum (blue). However, the excited mode is bounded at some singularities, and the radiation in the continuum is damped (orange). These states are called bound states.

Bound states are topological singularities that carry quantized phase singularities, known by topological charges [19,20]. Since the energy decays at the far away, it implies that energy is fully confined inside the system, and the quality factor diverges, the characteristic that is very important in high-Q cavity resonators. Although structures with infinite (or extremely large) lifetime are well developed, the popularity of resonators based on bound states

is in the part that they offer at least three interesting characteristics, i.e., 1) multiple beam generation, 2) steering beam, and 3) structured beam.

Generation of bound states in momentum space is highly dependent on the spatial symmetry of the periodic structure. It means that by controlling the structure symmetry, it is possible to generate multiple singularities at the same time. Moreover, the positions of these singularities in the momentum space are tunable by controlling the in-plane Floquet-Bloch waves. Since bound state singularities carry non-zero topological charges, thus their beam can have a structural behavior. All these three characteristics naturally exist at the same time in high-Q cavities based on bound states, which does not happen necessarily in other high-Q cavities.

In the second part of the thesis, which is inspired by our previous work of investigation of resonances in high-permittivity sub-wavelength dielectric cylindrical resonators in the microwave domain [21,22], we explore all aspects of the bound state singularities. We study how bound states can be used to design extended cavity resonators in topological light sources with peculiar characteristics.

1.4. Scope of This Thesis

The present thesis describes both the theory and the application of topological light sources. We study two topological singularities discussed above in details and use them as a primary tool for designing coherent integrated light sources (lasers). We demonstrate topological light sources are unique in their kind and applications that can address many fundamental questions such as compactness, flexibility in designing the shape of the cavity, all-electro-optical system (without mechanical components), generation of the tailored beams, and unidirectional emission to name but a few.

Chapter 2 presents the theory of topological insulators using Quantum Hall effect, and numerical analysis of 2-dimensional photonic systems. In this chapter, we design topological waveguides using hybrid photonic crystals (PhCs) and demonstrate the robustness of the waveguides to any kind of disorders. Photonic crystal waveguide is made of two different PhCs that are designed to have different topological phase transitions one of which is topologically trivial while the other one is topologically non-trivial. Finally, we discuss topological and non-topological (or conventional) cavities and study how topology can be used as an extra degree of freedom to design robust nonreciprocal cavity resonators with smaller footprints and large isolation ratios.

In chapter 3, based on the theoretical background of chapter 2, we use gain material of InGaAsP multiple quantum wells (MQWs), which is a gain material at telecommunication wavelength range (around $\lambda \sim 1.55 \mu\text{m}$) to design topological light sources. Since our approach is based on the Quantum Hall effect, thus magnetic material of Yttrium Iron Garnet (YIG) is used to break time-reversal symmetry. We demonstrate various topological cavities with arbitrary geometries that emit (in-plane) light in one direction with a sufficiently large isolation ratio (>10 dB).

In chapter 4, we use the same approach (chapter 3) to design and develop topological light sources that emit orbital angular momentum (OAM) beams with very large topological charges. OAM beams are the unbounded and orthogonal basis that have many applications in high capacity optical communications, imaging, and sensing. However, the generation of large topological charges is complicated. In this chapter, we design a topological system in a way that it emits light in the normal rather than in-plane direction. Then we study the possibility of the generation of OAM lights with very large topological charges using topological cavities in a fully planar structure. Finally, we demonstrate how to multiplex several of topological cavities in the same device, a characteristic that is useful, e.g., in high capacity optical communication.

In chapter 5, bound states in the continuums (BICs) are discussed in periodic structures. We theoretically study that BIC points are singularities in reciprocal space that carry non-zero topological charges, and their position can be tuned by modifying in-plane Floquet-Bloch phases. We then designed a periodic structure using gain material (InGaAsP MQWs) to make a light source that emits several vortex lights with tunable angles. All the aforementioned theoretically designed features, i.e., multiple beams, deflecting beams, and vortex characteristics are studied experimentally. Furthermore, topological charge conservation is also demonstrated.

Chapter 7, after summarizing all works done in this thesis, provides an outlook for future works on topological light sources (specifically), and topological systems (in general). We discuss current topological design, and other possible topological platforms that can be used to address further remaining questions in topological systems, and how topological photonics can pave the way toward designing whole integrated photonic circuits.

References

1. R. Shankar, Principles of Quantum Mechanics (Plenum, New York, 1980), Ch. 12.
2. S. Pancharatnam, "Generalized Theory of Interference, and Its Applications. Part I. Coherent Pencils," *Proc. Indian Acad. Sci. A* **44**, 247 (1956).

3. M. V. Berry, "Quantal Phase Factors Accompanying Adiabatic Changes," *Proc. of the Royal Soci. A* **392**, 45 (1984).
4. R. Jackiw, "Berry's phase-Topological ideas from atomic, molecular and optical physics," *Comments At Molecular Physics XXI*, 71 (1988).
5. K. von Klitzing, G. Dorda, and M. Pepper, "New Method for High-Accuracy Determination of the Fine-Structure Constant Based on Quantized Hall Resistance," *Phys. Rev. Lett.* **45**, 494 (1980).
6. D. J. Thouless, M. Kohmoto, M. P. Nightingale, and M. den Nijs, "Quantized Hall Conductance in a Two-Dimensional Periodic Potential," *Phys. Rev. Lett.* **49**, 405 (1982).
7. F. D. M. Haldane, "Model for a Quantum Hall Effect without Landau Levels: Condensed-Matter Realization of the "Parity Anomaly"," *Phys. Rev. Lett.* **61**, 2015 (1988).
8. M. Onoda and N. Nagaosa, "Quantized Anomalous Hall Effect in Two-Dimensional Ferromagnets: Quantum Hall Effect in Metals," *Phys. Rev. Lett.* **90**, 206601 (2003).
9. C. L. Kane and E. J. Mele, "Z₂ Topological Order and the Quantum Spin Hall Effect," *Phys. Rev. Lett.* **95**, 146802 (2005).
10. C. L. Kane and E. J. Mele, "Quantum Spin Hall Effect in Graphene," *Phys. Rev. Lett.* **95**, 226801 (2005).
11. D. J. Thouless, *Topological Quantum Number in Nonrelativistic Physics* (World Scientific, Singapore, 1998).
12. F. D. M. Haldane, and S. Raghu, "Possible Realization of Directional Optical Waveguides in Photonic Crystals with Broken Time-Reversal Symmetry," *Phys. Rev. Lett.* **100**, 013904 (2008).
13. Z. Wang, Y. Chong, J. D. Joannopoulos, and M. Soljacic, "Observation of unidirectional backscattering-immune topological electromagnetic states," *Nature* **461**, 772 (2009).
14. M. C. Rechtsman, J. M. Zeuner, A. Tunnermann, S. Nolte, M. Segev, and A. Szameit, "Strain-induced pseudomagnetic field and photonic Landau levels in dielectric structures," *Nature Photonics* **7**, 153 (2012).

15. M. Hafezi, S. Mittal, J. Fan, A. Migdall, and J. M. Taylor, “Imaging topological edge states in silicon photonics,” *Nature Photonics* **7**, 1001 (2013).
16. A. B. Khanikaev, S. H. Mousavi, W. -K. Tse, M. Kargarian, A. H. MacDonald, and G. Shvets, “Photonic topological insulators,” *Nature Materials* **12**, 233 (2013).
17. J. von Neumann and E. Wigner, “On some peculiar discrete eigenvalues,” *Phys. Z* **30**, 467 (1929).
18. J. J. Sakurai, *Modern Quantum Mechanics* (Revised ed.) Mass: Addison-Wesley. pp. 418 (1995).
19. N. D. Mermin, “The topological theory of defects in ordered media,” *Rev. Mod. Phys.* **51**, 591 (1979).
20. B. Zhen, C. W. Hsu, L. Lu, A. Douglas Stone, and M. Soljacic, “Topological Nature of Optical Bound States in the Continuum,” *Phys. Rev. Lett.* **113**, 257401 (2014).
21. T. Lepetit, E. Akmansoy, J.-P. Ganne, and J.-M. Lourtioz, “Resonance continuum coupling in high-permittivity dielectric metamaterials,” *Phys. Rev. B* **82**, 195307 (2010).
22. T. Lepetit and B. Kante, “Controlling multipolar radiation with symmetries for electromagnetic bound states in the continuum,” *Phys. Rev. B* **90**, 241103 (2014).

Chapter 2: 2D Topological Cavity

2.1. Introduction

By discovering topological insulators (TIs), a new paradigm of symmetry breaking has been created [1-3]. It was demonstrated that there are some topological orders in fermionic systems. In a simple language, TIs are materials that are insulator on the inside but conductor on the outside and can transport electrons without any back-scattering at the surface of the materials even in the presence of obstacles. This phenomenon was shown for the first time in the quantum by discovering integer Quantum Hall effect [1]. In this effect, it was demonstrated that in 2-dimensional electron gases in presence of strong magnetic field it exhibits a Hall conductance as a function of the magnetic field at integer numbers multiple of fundamental constant $e^2 = h$, where e is electron charge and h is Planck constant [1,4].

Following this discovery, many systems have been extensively studied and properties such as immunity to disorder have been demonstrated [5-7].

By discovering a new physics of topological phases of matter known as Quantum Spin-Hall effect or Z_2 TIs [8-11], the field of topological insulators became even more demanding and popular. Especially, now it enables to

study more range of systems beyond only electrons [12]. The recent demonstration by Raghu and Haldane of the possibility to transfer some topological properties from fermionic to bosonic systems such as light gives new degrees of freedom over the control of photons [13]. Several back-scatter immune waveguiding experiments have subsequently been proposed and demonstrated [21-14]. Discovery of the TI is motivating to explore robust topological systems in photonics [22-24]. In TI structures, unlike the phase shifters, the backward propagating mode does not exist, thus regardless of the size and shape of the device, light propagates only in one direction.

In the following, we study how to formulate and analyze a topological system. We design a topological waveguide using photonic crystals (PhCs). When the waveguide mode is excited, it propagates in one way, and it is robust to any kind of disorder. Then using topological waveguides, we explore topological cavities and compare them to conventional cavity resonators. We show how topological properties can be used as an extra degree of freedom to design, e.g., optical isolators with large isolation ratios and smaller footprints, the characteristics that are far-reaching in integrated optical circuits by today.

2.2. Berry Phase, Berry connection, and Chern Number

The Berry phase is as a phase acquired by the wave-function as the parameters appearing in the Hamiltonian are changing slowly in time. Berry phase happens in a cyclic and adiabatic evolution. Let's assume a Hamiltonian $\mathbf{H}(\mathbf{r})$ that depends on a parameter \mathbf{r} that varies with time t . Also, the n 'th eigenvalue $\varepsilon_n(\mathbf{r})$ remains non-degenerate everywhere along the path and the variation with the time is sufficiently slow. Then if a system is initially in the eigenstate of $|n(\mathbf{r}(0))\rangle$, it will remain in an instantaneous eigenstate of $|n(\mathbf{r}(t))\rangle$ up to a phase [25].

The wave-function evolves according to the time-dependent Schrodinger equation:

$$j\hbar \frac{\partial}{\partial t} |\Psi_n(t)\rangle = \mathbf{H}(\mathbf{r}) |\Psi_n(t)\rangle. \quad (2-1)$$

Thus, the state at time t can be written as [25]:

$$|\Psi_n(t)\rangle = e^{-\frac{j}{\hbar} \int_0^t dt' \varepsilon_n(\mathbf{R}(t'))} e^{j\gamma_n(t)} |n(\mathbf{R}(t))\rangle, \quad (2-2)$$

where the first term is a dynamic phase factor, the second term is the geometrical phase factor with γ_n being the Berry phase. Since $|\Psi_n(t)\rangle$ satisfies the time-dependent Schrodinger equation, it can be shown that [25]:

$$\gamma_n = j \oint_C d\mathbf{r} \langle n(\mathbf{r}) | \nabla_{\mathbf{r}} | n(\mathbf{r}) \rangle, \quad (2-3)$$

where

$$\mathcal{A}_n(\mathbf{r}) = j\langle n(\mathbf{r})|\nabla_{\mathbf{r}}|n(\mathbf{r})\rangle, \quad (2-4)$$

is called Berry connection. Using eq. (2-4), Berry curvature can be calculated as:

$$\Omega_n(\mathbf{r}) = \nabla_{\mathbf{r}} \times \mathcal{A}_n(\mathbf{r}). \quad (2-5)$$

For a closed path \mathcal{C} that forms the boundary of a surface S the closed-path Berry phase can be rewritten using Stokes theorem as:

$$\gamma_n = \int_S d\mathcal{S} \Omega_n(\mathbf{r}), \quad (2-6)$$

By analogy, we can derive similar relations for optical systems and for photons. We start with source-free Maxwell equations in linear and lossless media:

$$\nabla \times \mathbf{E} = -j\omega\mu\mathbf{H} \quad (2-7)$$

$$\nabla \times \mathbf{H} = j\omega\varepsilon\mathbf{E} \quad (2-8)$$

$$\nabla \cdot \mathbf{D} = 0 \quad (2-9)$$

$$\nabla \cdot \mathbf{B} = 0 \quad (2-10)$$

In a periodic system, mode with a wave-vector of $\mathbf{k} = k_x\hat{x} + k_y\hat{y}$ follow the Floquet-Bloch condition and are expressed as [26]:

$$\mathbf{E}_k(\boldsymbol{\rho}, z) = e^{jk \cdot \boldsymbol{\rho}} \mathbf{u}_k(\boldsymbol{\rho}, z) \quad (2-11)$$

where $\boldsymbol{\rho}$ is an n-plane vector (i.e., xy-plane), and \mathbf{u}_k is a periodic function in the in-plane direction which is also eigenmode of the wave equation in periodic systems.

Therefore, Berry connection is similarly defined as:

$$\mathcal{A}^{nn'}(k) = j \langle \mathbf{u}_{nk} | \nabla_k | \mathbf{u}_{n'k} \rangle, \quad (2-12)$$

where the brackets denote spatial integration over a unit-cell with the definition of

$$\langle \mathbf{u}_1 | \mathbf{u}_2 \rangle = \int d\mathbf{r} \varepsilon(\mathbf{r}) \mathbf{u}_1^* \cdot \mathbf{u}_2, \quad (2-13)$$

and Berry phase and Berry curvature are defined using eq. (2-3) and (2-5).

Finally, the Chern number for the n 'th band is given by [13]:

$$C_n = \frac{1}{2\pi} \int d\mathbf{k} \cdot \nabla_{\mathbf{k}} \times \mathcal{A}^n(\mathbf{k}), \quad (2-14)$$

In the dispersion band diagram, we can assign a sum of the Chern numbers to each full band gap by calculating the Chern number for each bulk mode below the band gap and adding all of them (i.e., $\Sigma C = \sum_{\text{modes below the gap}} C_n$). The band gaps that have non-zero ΣC are called a non-trivial band gaps, while those ones that have zero ΣC are called trivial band gaps.

2.3. Topological Waveguide Design

The first step to model a topological waveguide is to design a PhC waveguide with a non-zero phase transition between side walls [13]. In our approach, we use the Quantum Hall effect by using magnetic materials. By breaking time-reversal symmetry, it is possible to open a band gap in certain regions of the band diagram of the PhC. The band gap opened due to the broken time-reversal symmetry has a non-zero sum of the Chern number of all modes below the gap (i.e., $\sum C \neq 0$), thus it is referred to as a non-trivial photonic band gap.

To have a topologically non-trivial waveguide, the Chern numbers of side walls should be different [13], thus it is essential to design two different PhCs with different Chern numbers.

Figure 2-1a represents a start-shaped unit cell of a PhC with square lattice that is periodic in xy-plane. Relative permittivity, ε , of PhC in presence of an external magnetic field (EMF) is assumed to be

$$\varepsilon = 12.25 \begin{bmatrix} 1 & i0.008 & 0 \\ -i0.008 & 1 & 0 \\ 0 & 0 & 1 \end{bmatrix}, \quad (2-15)$$

Band diagram of this structure for an in-plane mode is calculated using a finite element method (Fig. 2-1b). As shown, a band gap is opened around the

frequency of $f = 194.23 \text{ THz}$. This gap that is opened due to the broken time-reversal symmetry has a non-zero topological phase invariant ($|\Sigma C| = 1$) calculated using eq. (2-14). Thus it is a non-trivial band gap.

If this non-trivial PhC is integrated with a trivial PhC or a non-trivial PhC but with different Chern number, it forms a topologically non-trivial edge waveguide in which excited edge mode propagates in one direction without any back-scattering. To design a trivial PhC, we use a PhC with an air hole unit cell and a triangular lattice made of the same material as previous PhC (Fig. 2-2a). In the band diagram

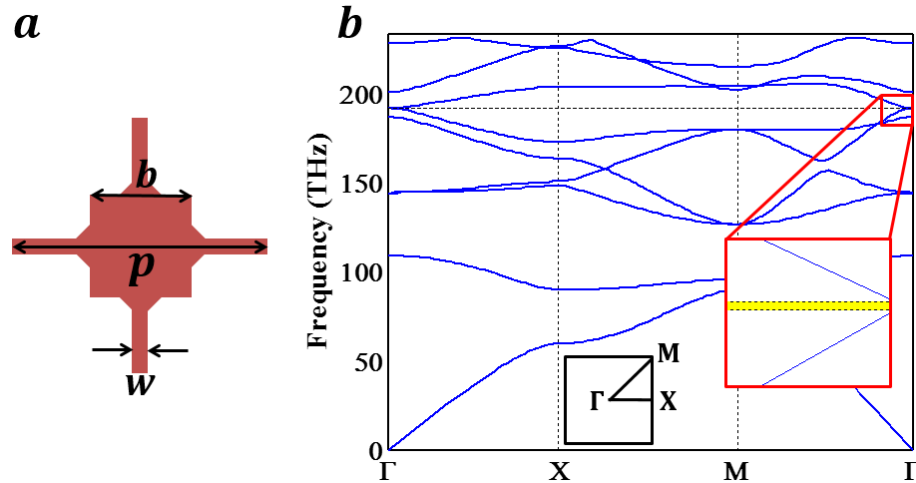


Figure 2-1 | (a) Schematic of the star-shaped unit cell of a PhC with square lattice that is periodic in two directions with the p , b , and w of 1176 nm , $0.5p$, and $0.0844p$, respectively. (b) Band diagram for an in-plane mode along irreducible Brillouin zone of the square lattice PhC.

of this unit cell, in presence of the same EMF, there is a large band gap between the first and second modes for an in-plane mode with a zero Chern number (Fig. 2-2b). By choosing the dimensions of this PhC properly, its band

gap can overlap with the band gap of the non-trivial PhC around the same frequency range.

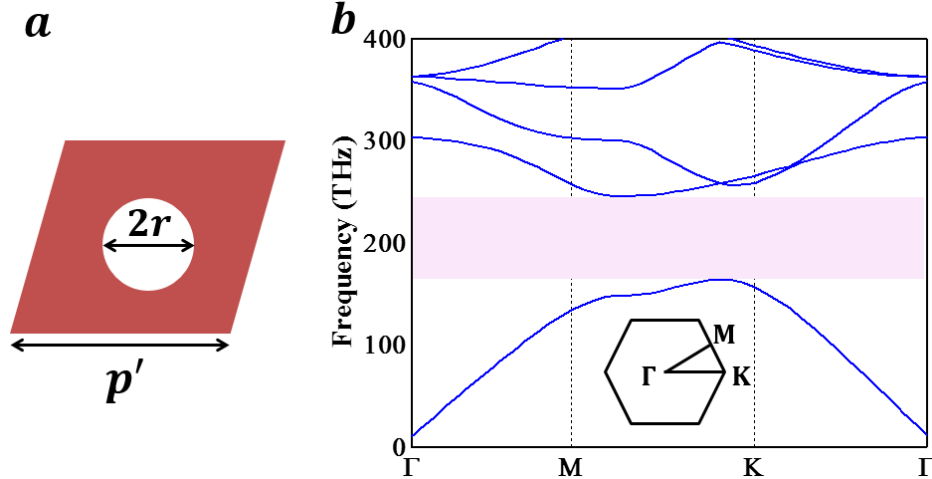


Figure 2-2 | (a) Schematic of the unit cell of PhC with an air hole and a triangular lattice. The periodicity and radius of the holes are $p' = p/3$, and $r = 0.35p'$, respectively. (b) Band diagram for an in-plane mode along irreducible Brillouin zone of the triangular lattice PhC.

By placing two semi-infinite PhCs made of these unit cells, an edge waveguide can be formed at the interface of them. To show one-way propagation, the configuration shown in Fig. 2-3a is simulated. In this structure, there are also sharp bends added to simultaneously study the robustness of the edge mode to any back-scattering. For a frequency within the band gap of both PhCs, edge mode of the structure is excited by a point source (S) and propagates in one direction regardless of the sharp bends (Fig. 2-3b). However, for a frequency that is not within the band gap of both PhCs, energy is not confined between them (Fig. 2-3c).

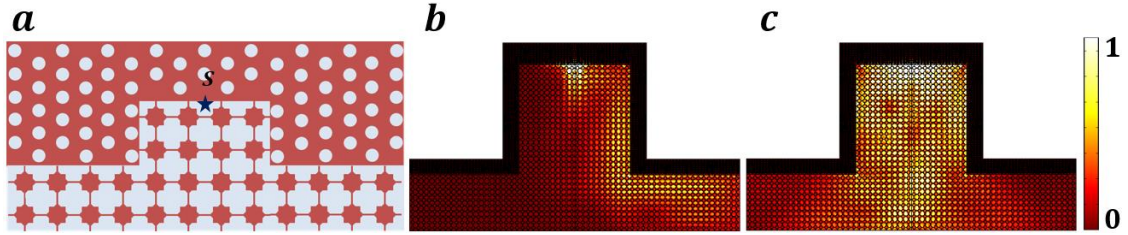


Figure 2-3 | (a) Schematic of an edge waveguide formed by placing non-trivial and trivial PhCs next to each other. Also, sharp bends are added to study the robustness of the edge waveguide to any back-scattering. The edge mode is excited by a point source (S) located at the center. (b,c) Field intensity distribution when the edge waveguide is excited with two different frequencies of $f = 194.23 \text{ THz}$ (b) and $f = 191 \text{ THz}$ (c). When the excitation frequency is within the band gap of both PhCs (b), the edge mode is confined between them and propagates in one direction without back-scattering. But the edge mode cannot be excited when the excitation frequency is out of the band gap of one or both PhCs (c).

2.4. Topological vs Non-topological Cavity

To compare the topologically trivial and non-trivial cavities, we utilize the two PhCs designed in session 2.3.

Figure 2-4a shows a cavity resonator and a waveguide close to the cavity all made of trivial PhC. Normally, in reciprocal case wave transmissions to both sides of the waveguide are the same. However, when time-reversal symmetry is broken, the dispersion curve of forward and backward wave propagations are not the same, and there is a frequency shift in the transmission curve. The amount of this shift depends on the Faraday rotation coefficient, which shows the polarization leakage from one polarization to the other one (in-plane \rightleftharpoons out-of-plane), and it is expressed by a unit of degrees

per length. To increase the frequency shift, it is needed to either increase the strength of broken time-reversal symmetry (i.e., the amplitude of the off-diagonal components in the permittivity tensor in eq. 2-15) or increase the length of the cavity. Unfortunately, the off-diagonal values cannot be increased arbitrarily because those are limited by the property of the material. Therefore, to have a large isolation ratio, the only way is to increase the length of the cavity to have enough frequency shift, which costs the large scale chip. The transmission spectrum for forward and backward propagations in the topologically trivial cavity is calculated and plotted in Fig. 2-4b. In this cavity,

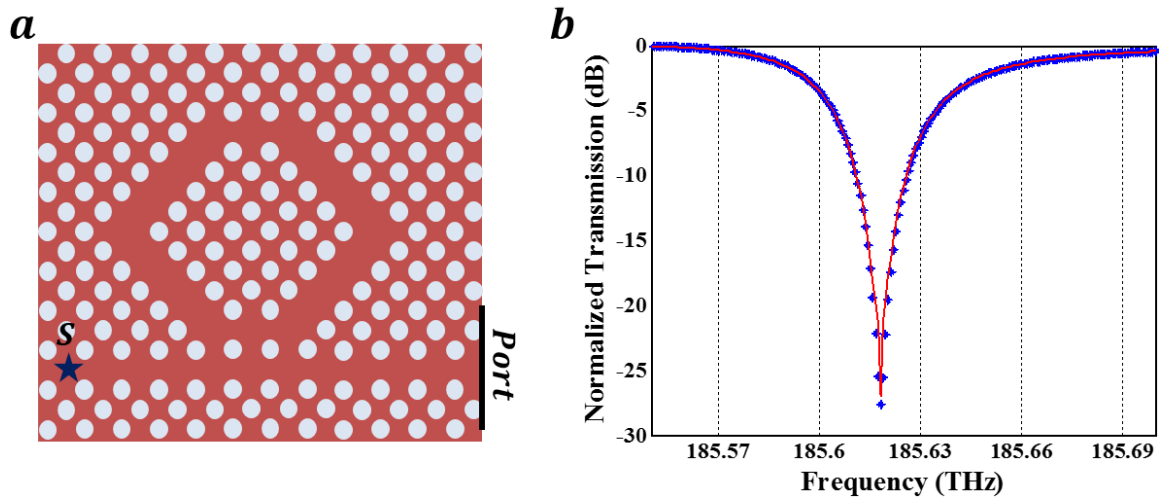


Figure 2-4 | (a) Schematic of a topologically trivial PhC cavity made of triangular PhC. Cavity and waveguide are formed by removing one line of air holes. The waveguide is excited by a point source (S) and the transmitted power is collected at the port. For the backward propagation, the position of the point source and the port are changed. (b) Normalized transmitted intensity for forward (blue stars) and backward (red solid line) wave propagations. The amount of the frequency shift is negligible, and both curves are look like the similar.

the frequency shift is very small, and the isolation between forward and backward propagations is a negligible value of $\sim 0.1\text{dB}$. Thus it looks like that structure is symmetric when excited from both sides (Fig. 2-5). Isolation ratio can be improved few decibels by increasing the length of the cavity resonator.

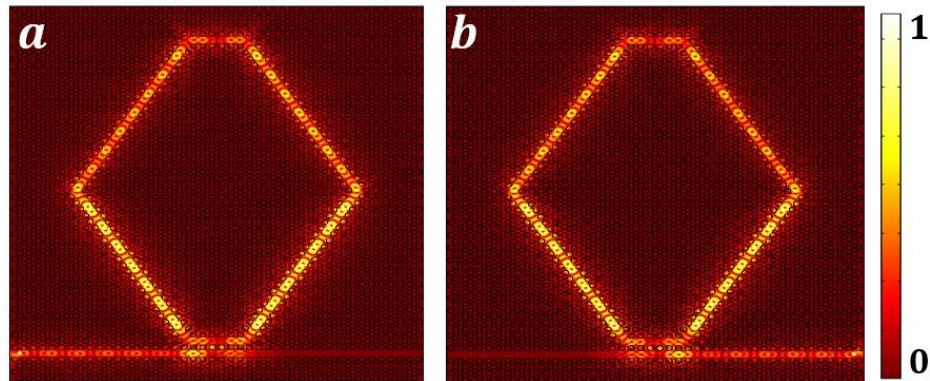


Figure 2-5 | (a,b) Normalized field intensity map inside the cavity when excited from both ends at the resonance frequency of $f = 185.627\text{ THz}$. Since the isolation ratio for the chosen cavity size is very small, thus both field distributions are pretty much the same.

Unlike the topologically trivial cavity, as discussed, in a topologically non-trivial cavity the backward propagation is forbidden. As a result, regardless of the size of the cavity, the isolation ratio is larger.

Figure 2-6a presents a topologically non-trivial cavity made of a non-trivial PhC inside the core of the cavity and a trivial PhC elsewhere. The size of the cavity is the same as for the trivial cavity. The transmission spectrum is calculated and plotted in Fig. 2-6b when the structure is excited by a point source (S). Initially, when time-reversal symmetry is not broken, there is no

non-trivial band gap, then edge mode does not exist and cavity does not resonate in a given frequency range (green line in Fig. 2-6b). The field intensity profile of this case is shown in Fig. 2-7a. By breaking time-reversal symmetry, the edge mode of the cavity is excited and it resonates around the frequency of $f = 194.23 \text{ THz}$ (blue line in Fig. 2-6b), which results in

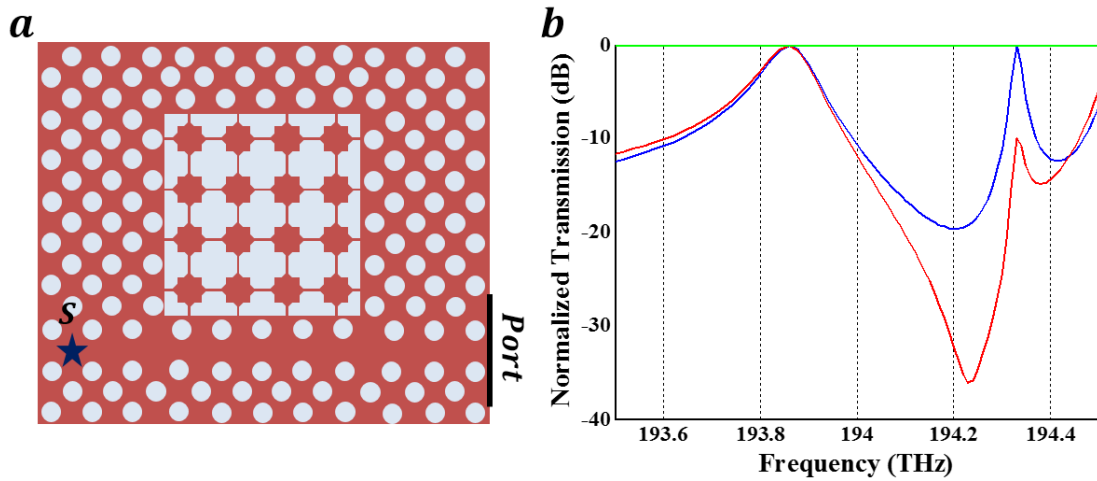


Figure 2-6 | (a) Schematic of a topologically non-trivial PhC cavity made of a non-trivial PhC as a core of the cavity and a trivial PhC elsewhere. The waveguide is excited by a point source (S) and transmitted power is collected at the port. For the backward propagation, the position of the point source and the port are changed. (b) Normalized transmitted intensity when there is no EMF (green line), and for forward (blue line) and backward (red line) wave propagations in presence of the EMF. The isolation between forward and backward propagations is about 16 dB for the same size of the cavity as a non-topological cavity shown in Fig. 2-4.

no transmission as shown in Fig. 2-7b. However, for an excitation from the opposite direction, the edge mode of the cavity cannot be excited due to the topological protection and mode is transmitted to the other side of the

waveguide (Fig. 2-7c). The isolation ration of about 16 dB is obtained for this structure.

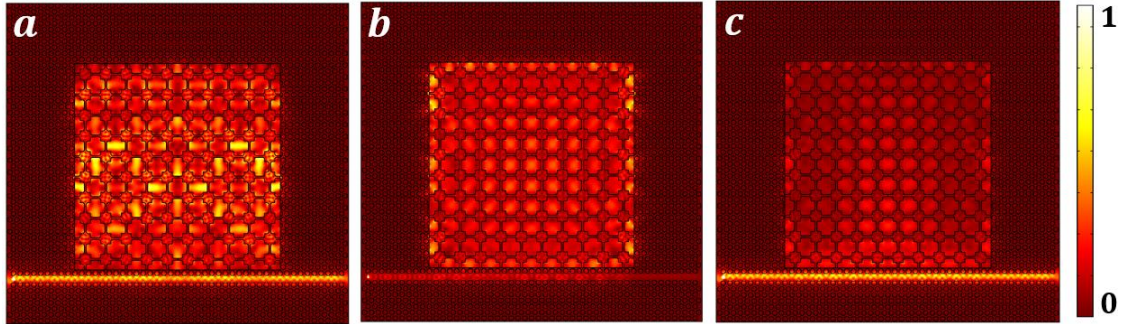


Figure 2-7 | (a-c) Normalized field intensity profile inside the cavity when it is excited from both ends of the waveguide with a frequency of $f = 194.23 \text{ THz}$, without EMF (a), with EMF and excited from the left side (b), and with EMF and excited from the right side (c). Scale bar is the same for all three field distributions.

2.5. Chapter Summary

In this chapter, we discussed how to design topological waveguide and topological cavity. We numerically demonstrated that topologically trivial edge waveguides are robust to any kind of disorders and back-scattering. The topological insulator can be used as a fundamental degree of freedom to design nonreciprocal cavities that previously use to be designed using, e.g., magnetic materials and based on solely breaking time-reversal symmetry. The theoretical results show for the same size of the cavity, while the isolation ratio for the topologically trivial cavity is negligible, for the topologically non-trivial cavity can be as large as 16 dB. This is mainly because backward propagating waves are forbidden in non-trivial cavities. Therefore, by using

the topological properties of cavities we can compensate for the weak gyromagnetism of the magnetic materials at higher frequencies which used to cost having systems like optical isolators with bulky sizes. In the next chapters, we demonstrate how topological cavities can be used to design light sources from cavities with arbitrary shapes that always emit coherent lights in one direction.

Chapter 2, in part, is a reprint of the material as it appears in B. Bahari, A. Ndao, F. Valini, A. E. Amili, Y. Fainman, and B. Kanté, “Experimental demonstration of non-reciprocal lasing in topological cavities of arbitrary geometries,” *Science* 358, 636-640 (2017). The dissertation author was the primary researcher and author of this paper.

References

1. K. von Klitzing, G. Dorda, and M. Pepper, “New Method for High-Accuracy Determination of the Fine-Structure Constant Based on Quantized Hall Resistance,” *Phys. Rev. Lett.* **45**, 494 (1980).
2. D. J. Thouless, M. Kohmoto, M. P. Nightingale, and M. den Nijs, “Quantized Hall Conductance in a Two-Dimensional Periodic Potential,” *Phys. Rev. Lett.* **49**, 405 (1982).
3. F. D. M. Haldane, “Model for a Quantum Hall Effect without Landau Levels: Condensed-Matter Realization of the "Parity Anomaly",” *Phys. Rev. Lett.* **61**, 2015 (1988).

4. K. von Klitzing, "The quantized hall effect," *Rev. Mod. Phys.* **58**, 519 (1986).
5. M. Buttiker, "Absence of backscattering in the quantum hall effect in multiprobe conductors," *Phys. Rev. B* **38**, 9375 (1988).
6. B. I. Halperin, "Quantized Hall Conductance, Current Carrying Edge States and Extended States in 2D Disordered Potential," *Phys. Rev. B* **25**, 2185 (1982).
7. A. H. MacDonald, and P. Streda, "Quantized hall effect and edge currents," *Phys. Rev. B* **29**, 1616 (1984).
8. B. A. Bernevig, L. T. Hughes, and S. C. Zhang, "Quantum spin hall effect and topological phase transition in hgte quantum wells," *Science* **314**, 1757 (2006).
9. B. A. Bernevig, and S. C. Zhang, "Quantum spin hall effect," *Phys. Rev. Lett.* **96**, 106802 (2006).
10. C. L. Kane, and E. J. Mele, "Quantum spin hall effect in graphene," *Phys. Rev. Lett.* **95**, 226801 (2005).
11. C. L. Kane, and E. J. Mele, "Z₂ topological order and the quantum spin hall effect," *Phys. Rev. Lett.* **95**, 146802 (2005).
12. T. Ozawa, H. M. Price, A. Amo, N. Goldman, M. Hafezi, L. Lu, M. Rechtsman, D. Schuster, J. Simon, O. Zilberberg, and I. Carusotto, "Topological Photonics," arXiv:1802.04173.
13. S. Raghu, and F. D. M. Haldane, "Analogues of quantum-Hall-effect edge states in photonic crystals," *Phys. Rev. A* **78**, 033834 (2008).
14. Z. Wang, Y. Chong, J. D. Joannopoulos, and M. Soljacic, "Observation of unidirectional backscattering-immune topological electromagnetic states," *Nature* **461**, 772 (2009).
15. A. B. Khanikaev, R. Fleury, S. H. Mousavi, and A. Alu, "Topologically robust sound propagation in an angular-momentum-biased graphene-like resonator lattice," *Nature Communications* **6**, 8260 (2015).

16. A. B. Khanikaev, S. H. Mousavi, W. -K. Tse, M. Kargarian, A. H. MacDonald, and G. Shvets, "Photonic topological insulators," *Nature Materials* **12**, 233 (2013).
17. Y. Plotnik, M. C. Rechtsman, D. Song, M. Heinrich, J. M. Zeuner, S. Nolte, Y. Lumer, N. Malkova, J. Xu, A. Szameit, Z. Chen, and M. Segev, "Observation of unconventional edge states in 'photonic graphene'," *Nature Materials* **13**, 57 (2014).
18. M. C. Rechtsman, J. M. Zeuner, Y. Plotnik, Y. Lumer, D. Podolsky, F. Dreisow, S. Nolte, M. Segev, A. Szameit, "Photonic Floquet topological insulators," *Nature* **496**, 196 (2013).
19. M. Hafezi, S. Mittal, J. Fan, A. Migdall, and J. M. Taylor, "Imaging topological edge states in silicon photonics," *Nature Photonics* **7**, 1001 (2013).
20. A. Slobozhanyuk, S. H. Mousavi, X. Ni, D. Smirnova, Y. S. Kivshar, and A. B. Khanikaev, "Three-dimensional all-dielectric photonic topological insulator," *Nature Photonics* **11**, 130 (2016).
21. A. Slobozhanyuk, A. N. Poddubny, A. E. Miroschnichenko, P. A. Belov, and Y. S. Kivshar, "Subwavelength Topological Edge States in Optically Resonant Dielectric Structures," *Phys. Rev. Lett.* **114**, 123901 (2015).
22. X. Cheng, C. Jouvaud, X. Ni, S. H. Mousavi, A. Z. Genack, and A. B. Khanikaev, "Robust reconfigurable electromagnetic pathways within a photonic topological insulator," *Nature Materials* **15**, 542 (2016).
23. B. Bahari, R. Tellez-Limon, and B. Kante, "Topological terahertz circuits using semiconductors," *Appl. Phys. Lett.* **109**, 143501 (2016).
24. M. Hafezi, E. A. Demler, M. D. Lukin, and J. M. Taylor, "Robust optical delay lines with topological protection," *Nature Physics* **7**, 907 (2011).
25. J. J. Sakurai, *Modern Quantum Mechanics (Revised ed.)* Mass: Addison-Wesley. pp. 418 (1995).
26. Sakoda, K., *Optical Properties of Photonic Crystals*, (2nd edition, Springer, 2001).

Chapter 3: Topological Laser

1.1. Introduction

During the past decade, topological photonics was one of the most interesting topics with high attention in exploring different platforms and techniques [1-13]. The main goal was to employ different approaches to demonstrate its physics, i.e., robust one-way edge wave without back-scattering, rather than making functional optical devices. The lack of back-scattering in topological systems proposes a range of applications in integrated photonics. For example, topological cavities with novel characteristics can be used in laser devices to improve their efficiencies. Light sources (or lasers) are one of the fundamental building blocks of any optical circuits. These sources are designed in many different classes with various specifications. Large scale sources such as fiber, Nd:YAG, CO₂ etc., are very well developed; however, still there are limitations in integrated lasers that need to be addressed before really using in the market. Any kind of lasers, regardless of their scale, face some fundamental challenges. Lasers need to be protected from instabilities and damages caused by back-reflected powers into the system. Using phase shifters or optical isolators are the most common and applicable techniques so far, especially for large scale lasers. However, when

it comes to small scales, i.e., integrated lasers, implementing these techniques are not straightforward simply because of the non-efficient phase shifters at these scales. At optical frequency ranges, lack of available materials with large enough nonreciprocity (or optical activity) is a fundamental challenge. Consequently, the size of the devices increases (toward large scale lasers), and their performances decrease. As discussed in the previous chapter, the topological properties of cavities can be used as an extra degree of freedom to overcome these kinds of problems. Using topological characteristic of a cavity, we are able to design integrated light sources that always emit in one direction and back reflected power cannot couple back into the source. Unlike phase shifters, in topological cavities, there is no state for back reflection. Thus the size and shape of the system also can be scaled arbitrarily without losing functionality. In the following, we will use the 2-dimensional design of topological cavities (presented in chapter 2) to demonstrate the first fully functional topological laser based on physics of topological insulators (TIs) [14]. Compared to the other topological lasers based on Quantum Spin-Hall effect or Z_2 TIs [15-19]; the advantages of our laser systems are in parts of unidirectional lasing, and geometry-independent cavities, which enables denser packing of components useful for all-integrated optical chips.

3.2. Design of topological cavities

The schematic of the proposed topological cavity platform is presented in Fig. 3-1. It is made of arbitrarily-shaped closed contours that constitute the cavity and a waveguide to which the cavity is evanescently coupled. The structures are made of structured InGaAsP multiple quantum wells (MQWs), bonded on Yttrium Iron Garnet (YIG) a gyrotropic material grown on Gadolinium Gallium Garnett (GGG) by molecular beam epitaxy. The YIG substrate is used to break time-reversal symmetry in the system under a static

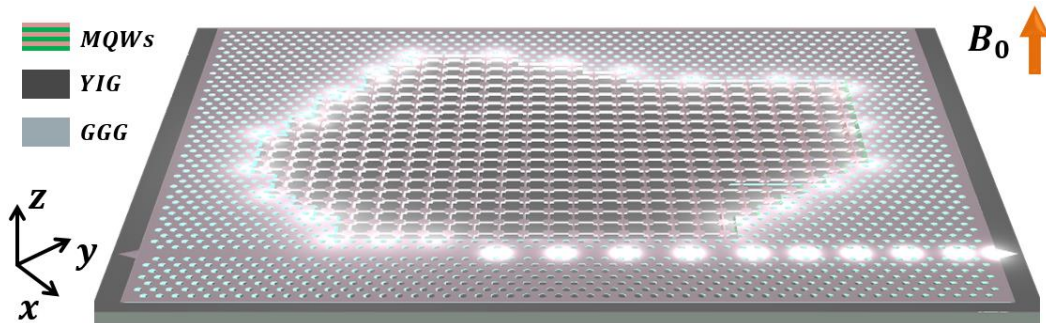


Figure 3-1 | Schematic of an arbitrarily-shaped and integrated topological cavity. The topological structure is an arbitrarily-shaped cavity formed between the boundaries of two photonic structures with distinct topological invariants. The structures are made of InGaAsP MQWs, bonded on YIG. The YIG substrate is used to break time-reversal symmetry in the system under a static EMF. The PhC enclosed by the cavity is a square lattice with a star-shaped unit cell, and the PhC outside of the cavity is made of a triangular lattice with cylindrical air holes unit cell. A defect waveguide is evanescently coupled to the cavity, and it is created by removing a line of air holes in the PhC with a triangular lattice. The topological one-way edge state circulating around the cavity is evanescently coupled to the defect waveguide resulting in emission at one output of the waveguide. The direction of emission can be reversed by flipping the sign of the EMF.

external magnetic field (EMF). The cavity is defined by two different PhCs. The PhC enclosed by the cavity is a square lattice with a star-shaped unit cell, and the PhC that is outside of the cavity constitutes the rest of the system, and it is made of a triangular lattice with cylindrical air holes unit cell. A defect waveguide coupled to the cavity is created by removing a line of air holes in the PhC with a triangular lattice. Distinct topological invariants of the two PhCs will ensure the existence of robust one-way edge states at their interface, creating a one-way topological cavity that will couple its emission either to the right or the left output of the waveguide depending on the direction of the EMF.

3.2.1. Band Diagram Calculation

Band diagrams of the two PhCs are calculated using finite-element method. Figure 3-2 presents the band diagram of the square lattice PhC in the presence of an EMF, $\mathbf{B} = B_0 \hat{\mathbf{z}}$, with $B_0 = +100 \text{ Oe}$. This magnetic field saturates the YIG material, maximizing the off-diagonal components of its dielectric permittivity tensor [20]. When there is no EMF, the band structure does not exhibit any gap in the frequency range of interest. Application of the EMF ($+B_0$) opens a narrow band gap (green shaded region in Fig. 3-2b) with a width of $\Delta\lambda \sim 42 \text{ pm}$. The topological invariant associated with the

corresponding band gap, i.e., Chern number, is $|\Sigma C| = 1$. Thus the band gap is called a non-trivial band gap.

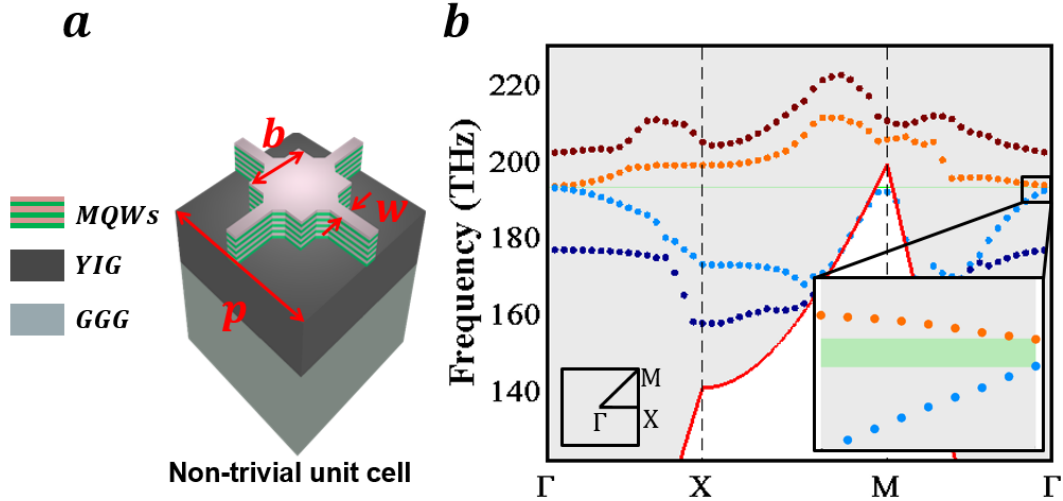


Figure 3-2 | (a) Schematic of a PhC with a star-shaped unit cell and a square lattice. The dimensions of the unit cell are $p=1084$ nm (period), $b=0.46p$, and $w=0.0844p$. (b) Photonic band diagram of a square lattice PhC. The band diagram is calculated in the presence of an EMF that saturates the YIG material, and thus maximizes the off-diagonal component of its dielectric permittivity tensor. When the EMF is zero, the band structure does not exhibit any gap in the frequency range of interest (not shown). The application of the EMF ($+B_0$) opens a narrow band gap (green shaded region) with a width of $\Delta\lambda\sim 42$ pm. The topological invariant associated with the corresponding band gap, i.e., Chern number, is $|\Sigma C| = 1$. Red solid lines represent the light-cone.

One-way interfaces can be implemented using another PhC with a different topological invariant. As seen in Fig. 3-3, the PhC with triangular lattice possesses a broadband gap regardless of the amplitude of the EMF and in particular for the value of EMF used for the non-trivial PhC. Calculations indicate a zero Chern number for this gap that is thus called a trivial band gap.

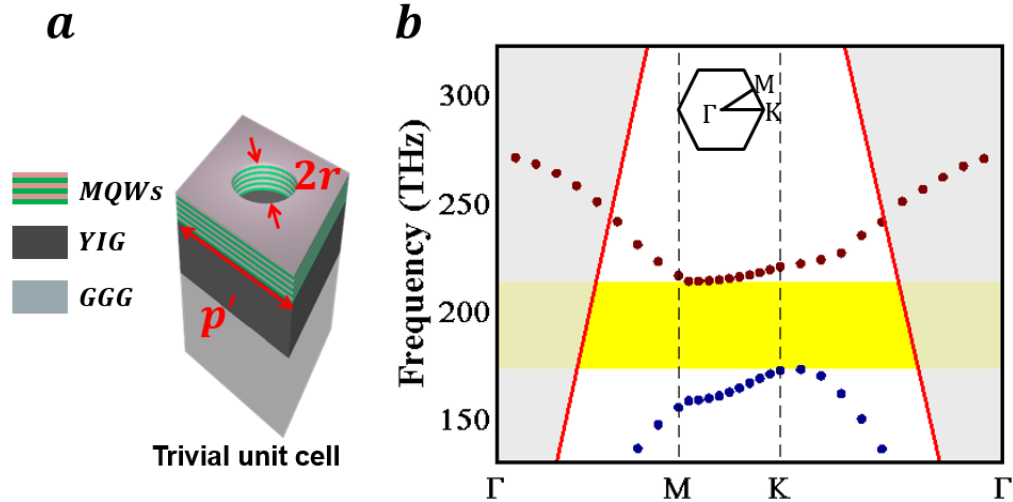


Figure 3-3 | (a) Schematic of a PhC with cylindrical air holes unit cell and a triangular lattice. The periodicity, p' , and radius of holes, r , are $p/3$ and $0.35p'$, respectively. (b) Photonic band diagram of the triangular lattice PhC in presence of the same EMF as in star-shaped PhC. A broadband gap is obtained, almost independent of the amplitude of the EMF. Calculations indicate a zero Chern number for this gap. Red solid lines represent the light-cone.

3.2.2. Trivial and Non-trivial Waveguides

Dimensions of the two PhCs have been chosen to overlap their band gaps around the telecommunication wavelength of $\lambda \sim 1.55 \mu m$. The closed contour between the trivial and non-trivial photonic structures constitutes the topological cavity that can have arbitrary geometries while maintaining its resonant frequency. The dissimilar topology of the two band gaps is numerically verified in Fig. 3-4 using a full wave three-dimensional simulation. A point source, S , with a frequency in the band gap of the two crystals, is placed at the interface between the two PhCs. The point source ensures the excitation of waves in all directions. Figure 3-4a shows that the

energy of the source is confined at the interface and propagates to the right for an EMF of $+B_0\hat{z}$. By reversing the direction of the EMF ($-B_0\hat{z}$) the propagation to the right is forbidden, demonstrating the existence of a one-way edge state.

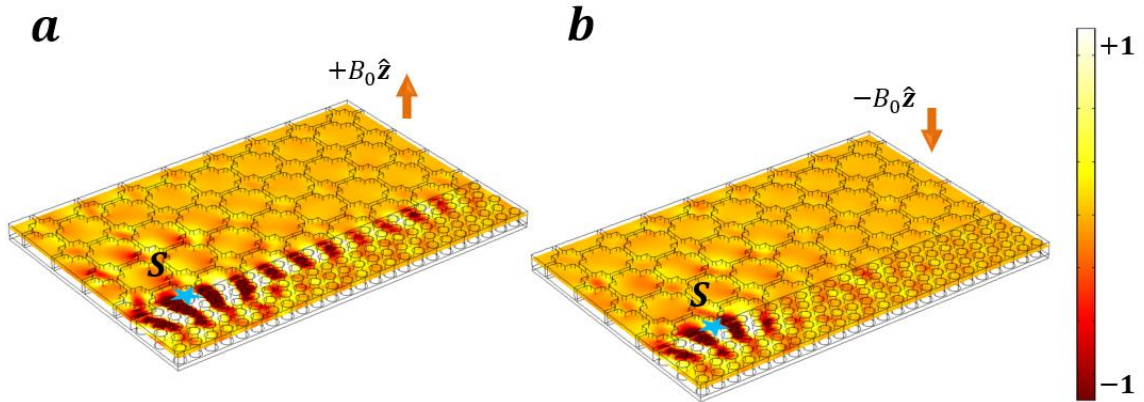


Figure 3-4 | Edge waveguide formed by two trivial and non-trivial PhCs. Edge mode is excited using a point source (S) located at the interface of two PhCs, and with a frequency that is at the band gap. The boundary between these two PhCs with overlapping band gaps supports one-way edge state that propagates either to the right (a) or to the left (b) depending on the direction of the EMF.

Field distributions inside the waveguide are plotted in Fig. 3-5, which shows that mode is predominantly in-plane with components of (E_x, E_y, H_z) .

To evaluate the cavity and the coupling lengths, we first calculate the effective index of the edge wave propagating at the interface between the trivial and non-trivial PhCs, which from now we call it non-trivial waveguide. We also calculate the effective index of the waveguide made of a line defect in the triangular PhC, which we call it trivial waveguide. Figure 3-6 shows full-wave simulations of both waveguides. The two waveguide modes are excited by a

point source at a wavelength of $\lambda_0 = 1531 \text{ nm}$, which is inside the band gap of the two PhCs. By calculating the propagation wavelengths, effective indices of 2.0 and 2.59 are obtained for non-trivial and trivial waveguides, respectively. The cavity length and the coupling length are thus chosen to be $v \times 780 \text{ nm}$, and $(2w + 1) \times 1300 \text{ nm}$, respectively, where v and w are integer numbers.

Now we have an edge mode that has a dispersion curve. To calculate its dispersion curve, we can use a full wave simulation of a supercell consisting of seven trivial and six non-trivial unit cells in one direction with an open

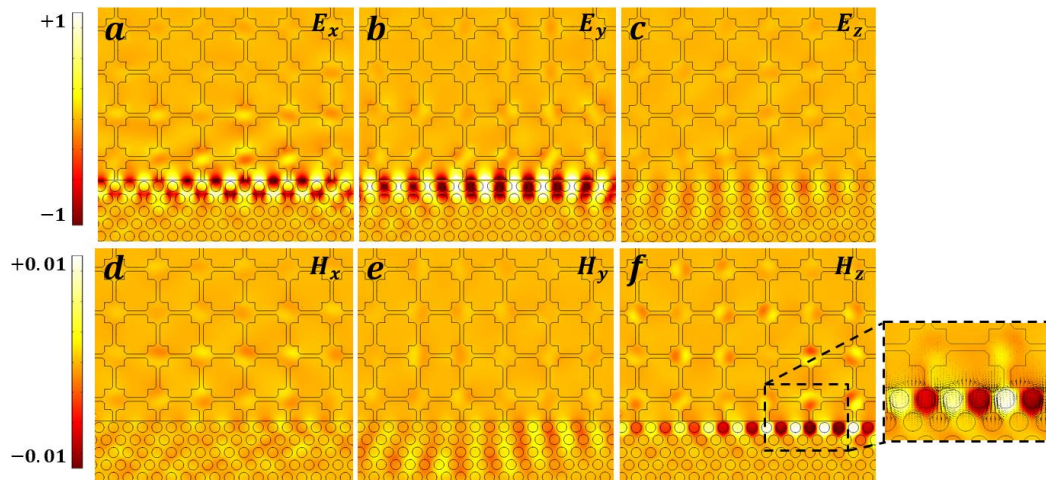


Figure 3-5 | Electric (a-c) and magnetic (d-f) fields intensity distribution inside the edge waveguide. Dominant field components are E_x , E_y , and H_z . The inset shows the total mode with H_z distribution (color plot), and E_x and E_y (vector plot).

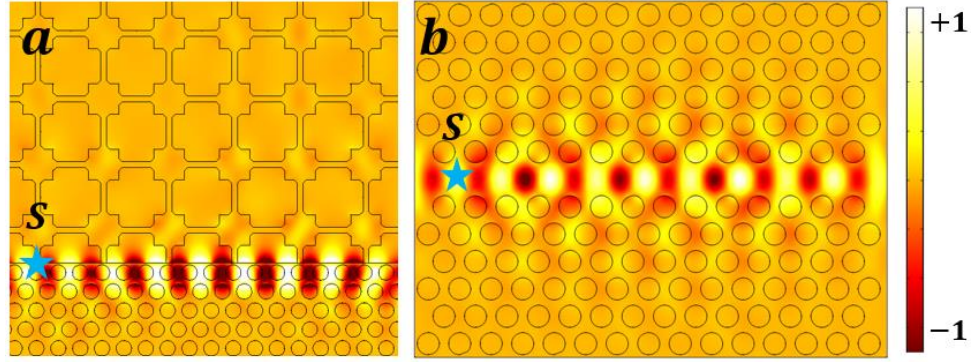


Figure 3-6 | Full wave three-dimensional simulations of non-trivial (a) and trivial (b) waveguides. The waveguides are excited by a point source, S , located at the left (star). When the excitation wavelength is within the band gap of the two PhCs, the excited mode is fully confined between two PhCs. The propagation wavelengths of $\lambda = 780 \text{ nm}$ and $\lambda = 600 \text{ nm}$ for the non-trivial and the trivial waveguides are obtained, respectively.

boundary at the ends, and with periodic boundary condition along the other direction (Fig. 3-7a). We then calculate the eigenmodes for different values of the normalized wave-vectors ($k_x a / 2\pi$) along two opposite directions from -0.5 to $+0.5$. The dispersion curve of the edge mode is plotted in Fig. 3-7b. Since the Chern number difference between side walls is $|\Delta C| = 1$, thus there is only one edge mode. Also, the sign of the slope of the edge mode is always the same due to the topological characteristic.

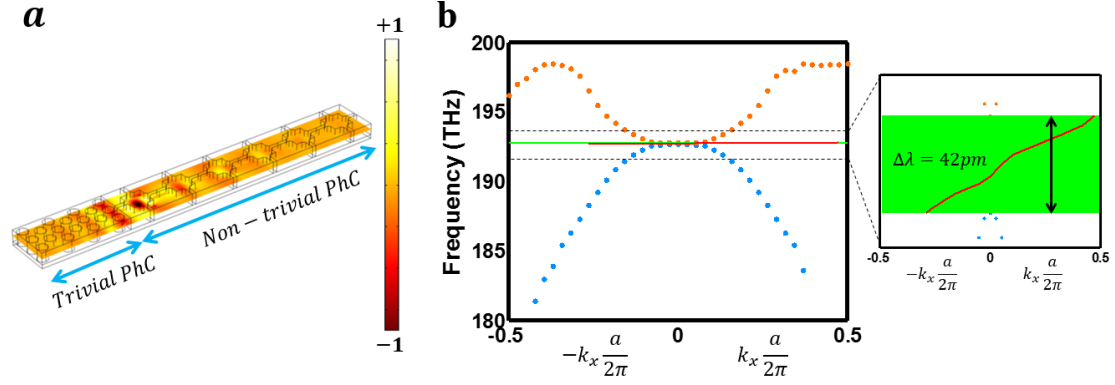


Figure 3-7 | (a) Full-wave simulation of a supercell consisting of seven trivial and six non-trivial unit cells in one direction with an open boundary at the ends, and periodic boundary condition along the other direction. Eigenfrequencies of the edge mode are calculated by changing the normalized wave-vector from -0.5 to $+0.5$ at the periodic boundary. The edge mode is fully confined at the interface of the two PhCs. (b) Dispersion band diagram of the non-trivial PhC (dotted points) with an opened band gap in presence of an EMF of $B_0 = +100 Oe$ (green shaded region). The dispersion curve of the trivial waveguide is plotted within the band gap (red solid line). Inset figure shows the zoom-in plot of the band diagram around the band gap. The dispersion curve of the trivial waveguide is represented by the red solid line.

3.3. Device Fabrication

The fabrication of nanostructures requires very high precision lithography and etching steps in order to control the position, size, and shape of patterns. We use standard nanofabrication protocol composed by electron ebeam lithography, reactive ion etching (RIE), and uniform bonding. The flow chart of the fabrication consists of several sequential steps schematically shown in Fig. 3-8. We first start by removing the protective layer on top of the InGaAsP using a chemical solution of HCl: H₂O (3:1) for 60 sec (step 2).

We then clean the InGaAsP sample using chemical baths and plasma procedures.

In the third step (step 3), the Hydrogen SilsesQuioxane (HSQ) negative tone resist is spin-coated on InGaAsP, and the image-patterning is performed by electron-beam irradiation. Using RIE ($\text{H}_2:\text{CH}_4:\text{Ar}$ (40:10:7) for seven minutes), the pattern is transferred onto the InGaAsP. Next, residual organic contamination and polymer buildup during RIE are removed with microwave oxygen (O_2) plasma treatment, and the residual HSQ layer is removed by immersing the sample into the hydrofluoric acid for about 30 sec.

For a successful bond, it is crucial to thoroughly clean the substrate in order to acquire a dust-free and chemically receptive surface for the subsequent bonding steps. The YIG is immersed in an acetone bath to remove any organic traces and then transferred to an ethanol-containing beaker. To bond the sample, 20 nm of an electron ebeam resist (PMMA) is spin coated on the YIG substrate (4000 rpm at 1000 rpm/sec) followed by a hard-bake for 5 min at 185 °C (step 5). Subsequently, the InGaAsP is bonded on the prepared YIG substrate coated with PMMA. We performed the bonding process with a clamp to apply uniform pressure. The sample is thus put into an oven for curing at 240°C for one hour under 80 kPa pressure. The curing process lasts

about five hours including about one hour of raising the temperature from room temperature to 240°C, one hour maintaining at this temperat-

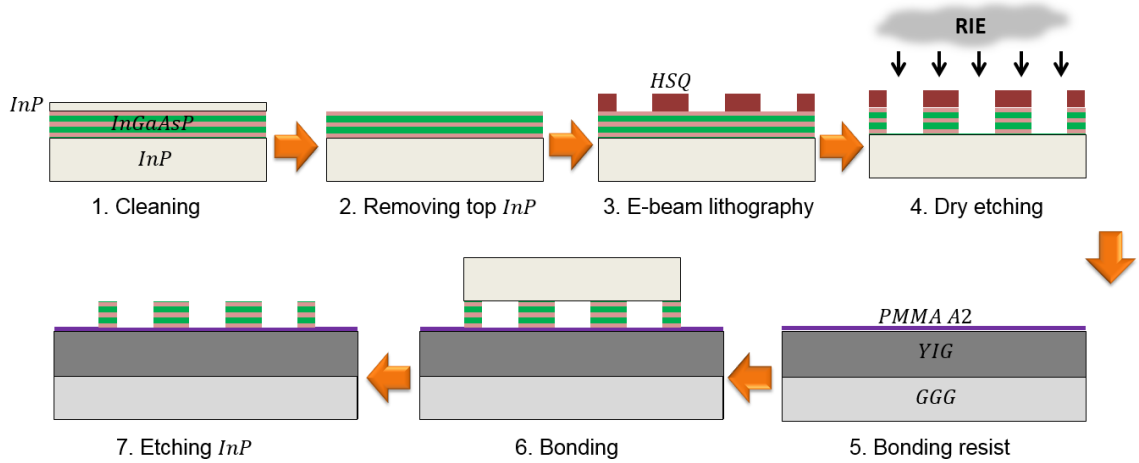


Figure 3-8 | Flow chart of the fabrication. **Step 1:** InGaAsP MQWs wafer. **Step 2:** Removal of the protective layer thin InP layer (thickness = 10 nm). **Step 3:** Spin coating HSQ resist, e-beam lithography patterning, and development. **Step 4:** Dry etch using RIE ($H_2:CH_4:Ar$ (40:10:7).) to transfer the pattern from HSQ onto the InGaAsP. **Step 5:** Cleaning the YIG substrate and coating of PMMA on the YIG and baking at 185°C for five minutes. **Step 6:** Bonding InGaAsP on the YIG and curing in the oven at 240°C for one hour, and pressure of 80 kPa. The curing process was about five hours including one hour to raise the temperature from room temperature to 240°C, one hour of curing at this temperature, and about three hours to cool down the sample to room temperature. **Step 7:** Removal of InP substrate using a solution of HCl: H_2O (3:1) to selectively etch InP without affecting the rest of materials. The etching time is about one hour.

ure, and about three hours cooling down the sample to room temperature (step

6). The last step removes the InP substrate using a chemical solution of HCl:

H_2O (3:1). The whole etching process to remove the InP lasts about one hour.

This step is also visually controllable because InGaAsP is perfectly crystalline

and is thus flat and visually reflective, whereas InP becomes rough during

etching. When hydrochloric acid reaches InGaAsP, etching stops. Finally, we remove the sample from the solution and rinsed it with Deionized (DI) water (step 7).

To demonstrate the versatility of the proposed platform, we first investigate a square cavity coupled to the waveguide. The total length of the non-trivial cavity and the coupling length between the cavity and the waveguide were optimized for the edge mode by choosing $v = 167$ and $w = 12$, which results in a cavity length of $130 \mu m$ and coupling length of $32.5 \mu m$. Figure 3-9 presents a top view Scanning Electron Micrograph (SEM) of a fabricated device where the trivial and non-trivial PhCs together with the waveguide can be seen. The fabrication is uniform over the entire area of the device.

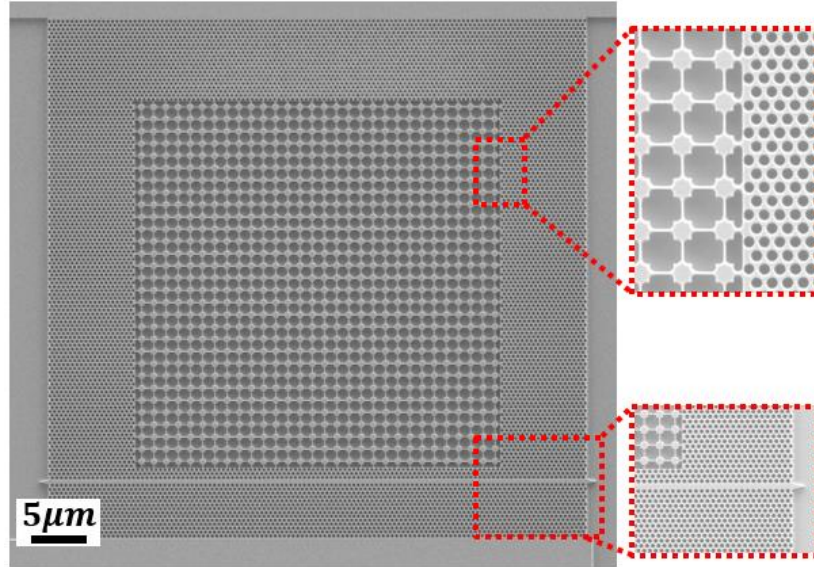


Figure 3-9 | Top view SEM of a fabricated squared-shaped topological cavity where the trivial and non-trivial PhCs together with the waveguide are visible. End of the waveguide from both sides are tapered so that waveguide mode can couple out and be collected using a lensed fiber for spectrum analyzing.

3.4. Device Characterization

3.4.1. Field Intensity Imaging

To experimentally characterize the device, we optically pumped it from the top with a pulsed laser ($\lambda_{\text{pump}} = 1064 \text{ nm}$, $T = 12 \text{ ns}$ pulse at a repetition rate $f = 275 \text{ kHz}$) using a micro-photoluminescence setup. The size of the pump beam is controlled to cover the whole area of the device. To generate the necessary EMF, we use a homemade electromagnetic solenoid coil that can generate a uniform and tunable magnetic field of $B_{\text{Max}} = 150 \text{ Oe}$ inside the solenoid. Figure 3-10 represents real space camera images of the surface of the devices without ($B_0 = 0$) and with ($B_0 = +100 \text{ Oe}$) EMF for a pump

power density of $\rho = 0.9 \mu W/\mu m^2$. An edge mode localized at the interface between the two PhCs is observed in the presence of the EMF (Fig. 3-10b) while it disappears when the EMF is turned off (Fig. 3-10a).

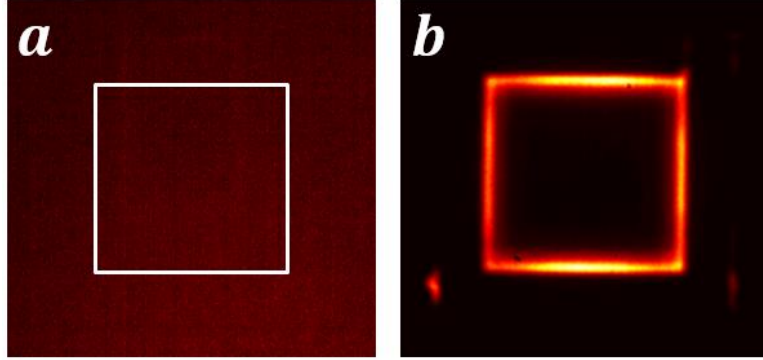


Figure 3-10 | Real space camera images of the top of the device without (a) and with (b) EMF under optical pumping using a laser with a wavelength of $\lambda_{\text{pump}} = 1064 \text{ nm}$. An edge mode localized at the interface between the two PhCs is observed in the presence of the EMF while it disappears when the EMF is turned off.

3.4.2. Photoluminescence Measurement

When the EMF is turned off, the non-trivial band gap closes, and the edge mode disappears. We pump the structure with the same power density ($\rho = 0.9 \mu W/\mu m^2$), and measure the photoluminescence using a lensed fiber. To characterize the device and demonstrate the emission of the edge mode, a lensed fiber is placed to one of the outputs of the waveguide. The outputs of the waveguides are tapered to ensure efficient coupling to the fiber. The coupling was aided by a piezoelectric positioning device with nanometer resolution. The tip of the lensed fiber is placed in front of the waveguide and

the other end of the fiber is directly connected to an optical spectrum analyzer. Fig. 3-11 shows the emission spectrum over a broad wavelength range, clearly revealing the absence of stimulated emission when the magnetic field is turned off.

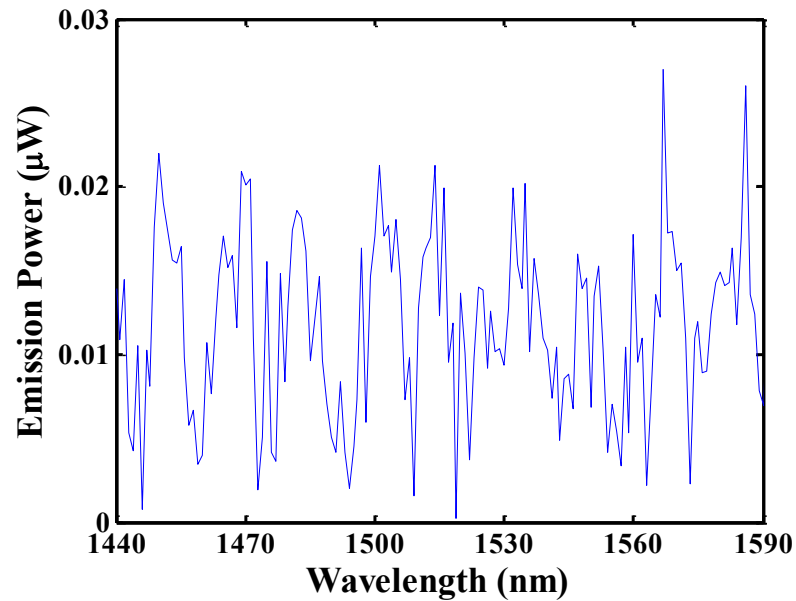


Figure 3-11 | Emission spectra of the square cavity when it is pumped with the pump power density of $\rho = 0.9\mu W/\mu m^2$ and without EMF. The emission power is collected using a lensed fiber. Without EMF the edge mode disappears and no cavity mode can be excited.

Figure 3-12 shows the photoluminescence spectrum of the cavity shown in Fig. 3-9 for the forward (Fig. 3-12a) and the backward (Fig. 3-12b) biases of EMF for different pump powers. When the EMF is reversed, cavity couples the lasing power to the opposite end of the trivial waveguide and the emission power reduces.

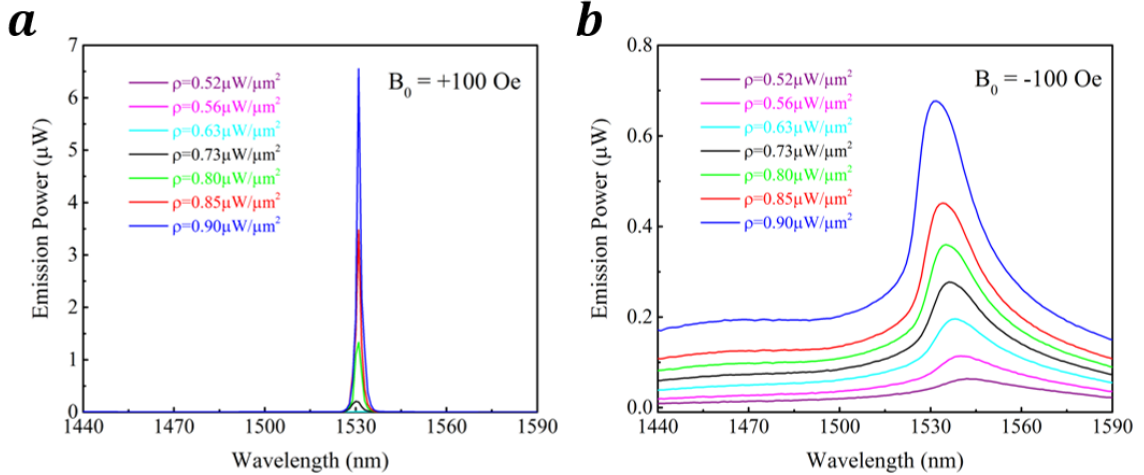


Figure 3-12 | Photoluminescence spectrum of the square cavity when the EMF is (a) $B_0 = +100$ Oe, and (b) $B_0 = -100$ Oe. Lensed fiber is fixed in one end of the trivial waveguide, and it collects the photoluminescence power for two different EMFs.

Figure 3-13a shows the evolution of the output power as a function of both pump power density and wavelength. By varying the pump power density with the EMF turned on, a threshold behavior with a clear transition from spontaneous emission to stimulated emission (i.e., lasing) is observed. Turning off the EMF results in the suppression of lasing.

To prove that lasing is from a one-way edge mode, the direction of the EMF is flipped by reversing the current in the solenoid creating $B = -B_0\hat{z}$ and the emitted power and its spectrum are measured. This is equivalent to coupling the fiber to the other end of the waveguide for a fixed direction of the EMF, with the advantage of avoiding discrepancies between the coupling efficiencies to the two ends of the waveguide, thus enabling quantitative comparison of the emissions.

Figure 3-13b presents the output emission power of the structure for two opposite values of the EMF ($+B_0$ and $-B_0$) and for the same pump power density ($\rho = 0.9 \mu\text{W}/\mu\text{m}^2$) in the lasing regime. As seen, there is a large reduction in the photoluminescence spectrum and an isolation ratio of 9.85 dB is measured. In non-topological cavities with broken time-reversal symmetry, the clock-wise (CW) and the counter clock-wise (CCW) modes of the cavity have similar characteristics, but a small wavelength shift [20]. However, in topological cavities, one of the modes,

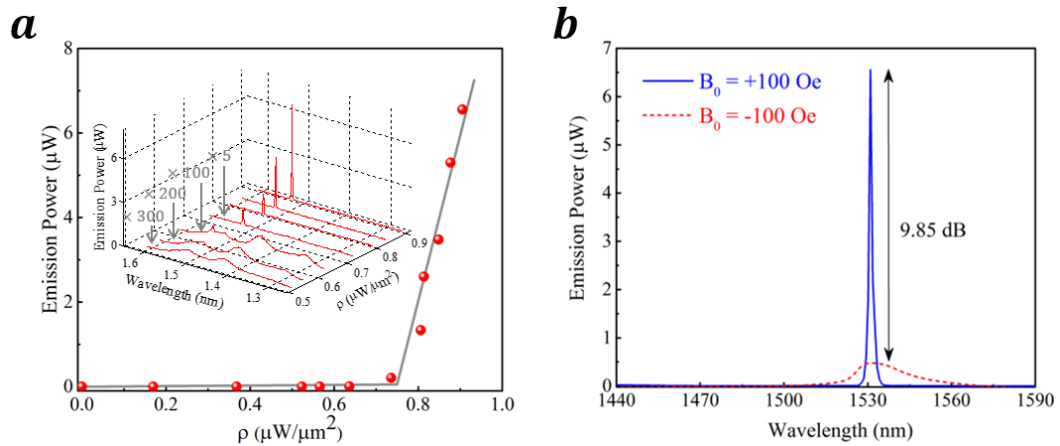


Figure 3-13 | (a) Evolution of the output power collected by a lensed fiber coupled to the output of the trivial waveguide as a function of pump power density and wavelength. Red dots are experimental measurements of the output power for different pump power densities when the EMF is turned on. Gray solid lines are linear fits to the data in spontaneous and stimulated emission regimes and clearly show a threshold behavior, i.e., lasing. No lasing is observed in the absence of EMF. (b) Emission power for a pump power density of $\rho = 0.9 \mu\text{W}/\mu\text{m}^2$ for two opposite values of the EMF ($+B_0$ and $-B_0$), which is equivalent to collecting emission from the two outputs of the waveguide with the advantage of avoiding coupling discrepancies. An isolation ratio of 9.85 dB is experimentally observed, confirming non-reciprocal lasing.

either the CW or the CCW is forbidden depending on the direction of EMF, thus cannot be excited, ensuring single mode operation. This is a fundamental difference between topological systems, as non-topological cavities will exhibit two slightly detuned modes that both lay within the broad gain bandwidth of the semiconductor and would thus give rise to mode competition.

3.5. Geometry-independent Cavities

Topological edge modes are robust against back-scattering from imperfections and sharp corners. Beyond robust and passive transport, this implies the possibility to implement deformed cavities of arbitrary geometries. Figure 3-14 shows the top view SEM of an arbitrarily-shaped cavity with the same optical length as the square cavity. We optically pump the device from the top, collect and analyze the emission from the tapered waveguide using the lensed fiber again.

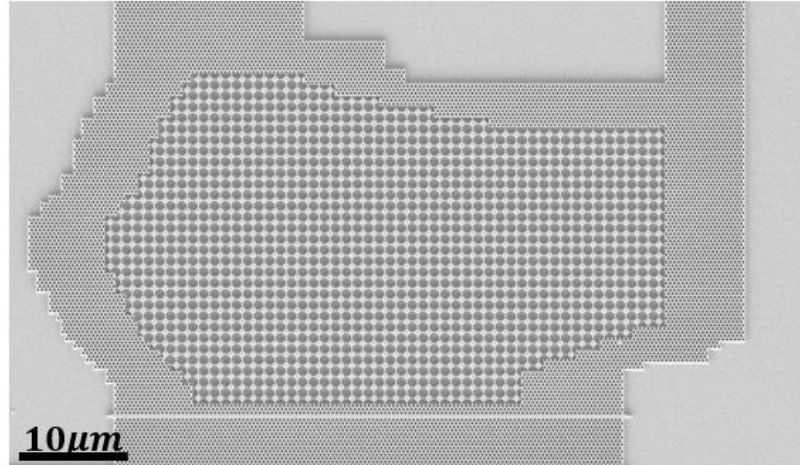


Figure 3-14 | Top view SEM of a fabricated topological cavity with a random geometry formed by the trivial and non-trivial PhCs. The optical length of the cavity is the same as the square cavity.

3.5.1. Far-field Intensity Imaging

When the EMF is turned on, real space imaging of the top of the device (Fig. 3-15a) provides evidence for an edge mode that is tightly confined at the boundary of the topologically distinct photonic structures. When EMF is turned off, the edge mode disappears (Fig. 3-15b).

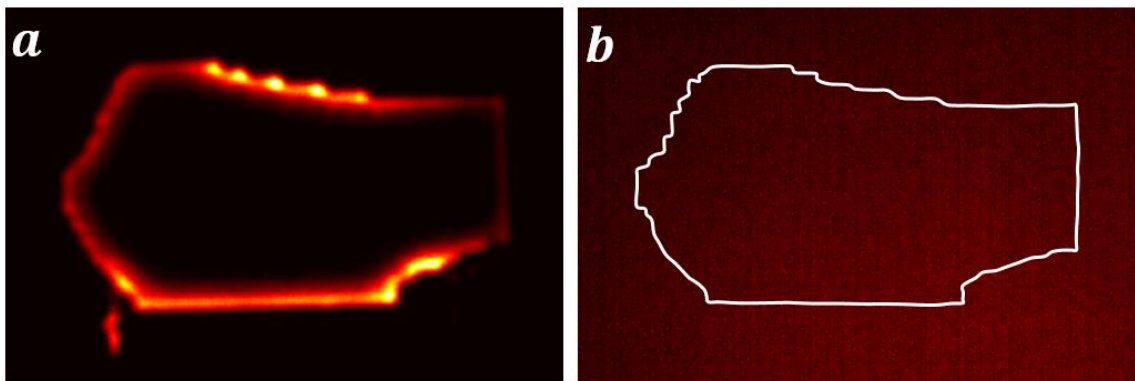


Figure 3-15 | Real space camera images of the top of the device with (a) and without (b) EMF under optical pumping using a laser with a wavelength of $\lambda_{\text{pump}} = 1064 \text{ nm}$. An edge mode localized at the interface between the two PhCs is observed in the presence of the EMF while it disappears when the EMF is turned off.

3.5.2. Photoluminescence Measurement

Figure 3-16 shows the photoluminescence spectrum of the cavity shown in Fig. 3-14 for the forward (Fig. 3-16a) and the backward (Fig. 3-16b) biases of EMF for different pump powers. When the EMF is reversed, cavity couples the lasing power to the opposite end of the waveguide.

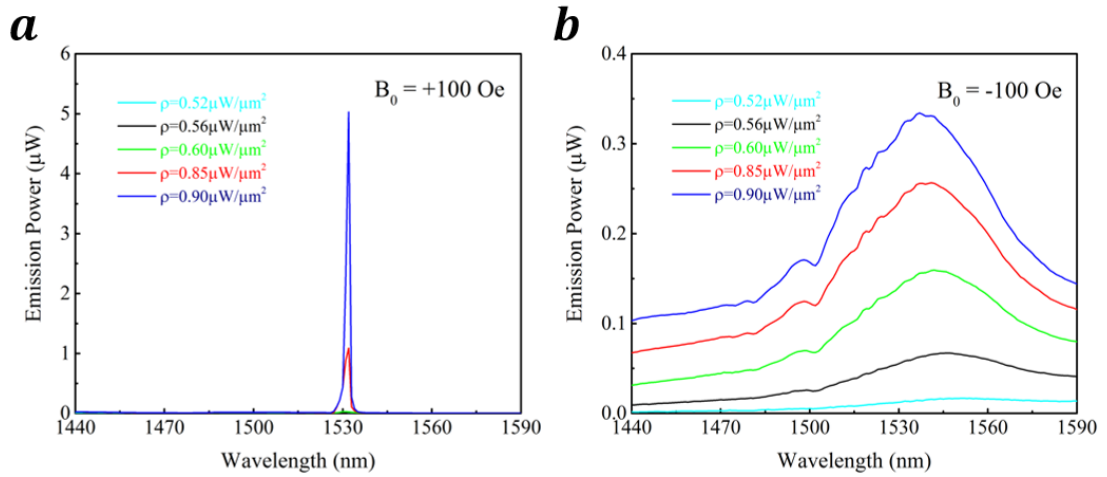


Figure 3-16 | Photoluminescence spectrum of the square cavity when the EMF is (a) $B_0 = +100$ Oe, and (b) $B_0 = -100$ Oe.

Unidirectional lasing with an isolation ratio of 11.3 dB is experimentally achieved with a pump power density of $\rho = 0.9 \mu$ W/ μ m² (Fig. 3-17).

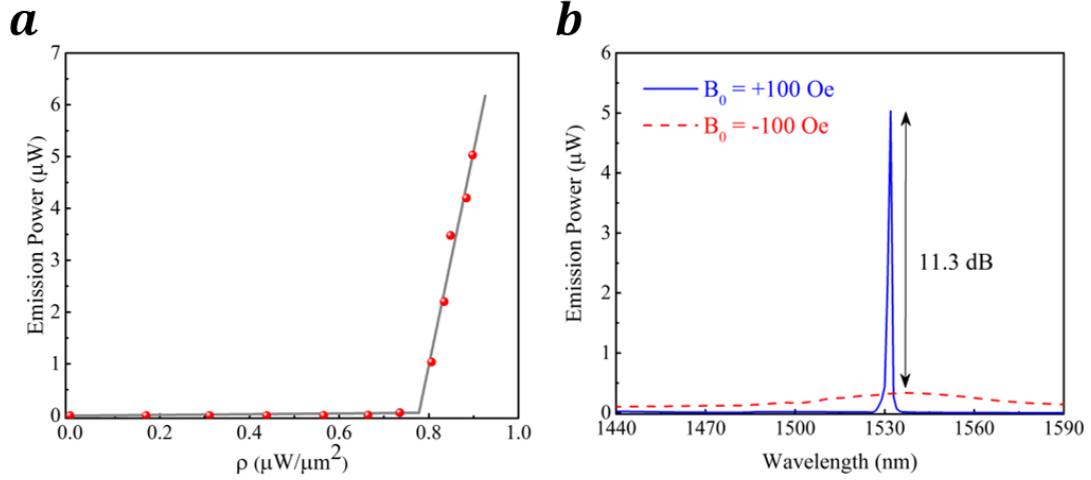


Figure 3-17 | (a) Evolution of the output power as a function of the pump power density (light-light curve) for the cavity with the random shape (Fig. 3-14). The red dots represent the experimental measurements of the output power for different pump power densities when the EMF is turned on ($B_0 = +100$ Oe). Gray solid lines represent linear fits to the data in spontaneous and stimulated emission regimes and clearly show a threshold behavior, i.e., lasing. (b) Emission power for a pump power density of $\rho = 0.9 \mu\text{W}/\mu\text{m}^2$ for two opposite values of the EMF ($+B_0$ and $-B_0$). An isolation ratio of 11.3 dB is experimentally observed, confirming non-reciprocal lasing.

Other cavities with deformed cavities are demonstrated and characterized in appendix 1.

3.6. Chapter Summary

In this chapter, we experimentally demonstrated non-reciprocal lasing from topological cavities of arbitrary geometries. The topological cavities are closed contours between hybrid photonic structures with distinct topological invariants and thus support unidirectional edge states circulating around the cavity. We made the topologically distinct structures from two PhCs with overlapping trivial and non-trivial band gaps at telecommunication

wavelengths. Cavities are implemented on structured InGaAsP MQWs, the semiconductor providing optical gain, bonded on a YIG substrate that breaks time-reversal symmetry in the devices. By evanescently coupling a waveguide to the topological cavity, stimulated emission from the one-way mode is coupled to a selected waveguide output with an isolation ratio as large as 11.3 dB. These results demonstrate the flexibility of topological cavities in photonic integration where information can robustly flow between sectors characterized by their topological invariants and will enable the investigation of non-trivial photonic devices. Furthermore, robust unidirectional waves in topological cavities could be used for generation of structured lights with very large topological charges that is the subject of discussion in the next chapter.

Chapter 3, in part, is a reprint of the material as it appears in B. Bahari, A. Ndao, F. Valini, A. E. Amili, Y. Fainman, and B. Kanté, “Experimental demonstration of non-reciprocal lasing in topological cavities of arbitrary geometries,” *Science* 358, 636-640 (2017), and B. Bahari, and B. Kanté, “Experimental demonstration of non-reciprocal lasing in topological cavities of arbitrary geometries,” United States patent (US Provisional Patent Application No. 62/540,809), 2017. The dissertation author was the primary researcher and author of this paper and patent.

References

1. C. L. Kane, and E. J. Mele, "Quantum spin hall effect in graphene," *Phys. Rev. Lett.* **95**, 226801 (2005).
2. C. L. Kane, and E. J. Mele, "Z₂ topological order and the quantum spin hall effect," *Phys. Rev. Lett.* **95**, 146802 (2005).
3. Z. Wang, Y. Chong, J. D. Joannopoulos, and M. Soljacic, "Observation of unidirectional backscattering-immune topological electromagnetic states," *Nature* **461**, 772 (2009).
4. A. B. Khanikaev, R. Fleury, S. H. Mousavi, and A. Alu, "Topologically robust sound propagation in an angular-momentum-biased graphene-like resonator lattice," *Nature Communications* **6**, 8260 (2015).
5. A. B. Khanikaev, S. H. Mousavi, W. -K. Tse, M. Kargarian, A. H. MacDonald, and G. Shvets, "Photonic topological insulators," *Nature Materials* **12**, 233 (2013).
6. Y. Plotnik, M. C. Rechtsman, D. Song, M. Heinrich, J. M. Zeuner, S. Nolte, Y. Lumer, N. Malkova, J. Xu, A. Szameit, Z. Chen, and M. Segev, "Observation of unconventional edge states in 'photonic graphene'," *Nature Materials* **13**, 57 (2014).
7. M. C. Rechtsman, J. M. Zeuner, Y. Plotnik, Y. Lumer, D. Podolsky, F. Dreisow, S. Nolte, M. Segev, A. Szameit, "Photonic Floquet topological insulators," *Nature* **496**, 196 (2013).
8. M. Hafezi, S. Mittal, J. Fan, A. Migdall, and J. M. Taylor, "Imaging topological edge states in silicon photonics," *Nature Photonics* **7**, 1001 (2013).
9. A. Slobozhanyuk, S. H. Mousavi, X. Ni, D. Smirnova, Y. S. Kivshar, and A. B. Khanikaev, "Three-dimensional all-dielectric photonic topological insulator," *Nature Photonics* **11**, 130 (2016).
10. A. Slobozhanyuk, A. N. Poddubny, A. E. Miroshnichenko, P. A. Belov, and Y. S. Kivshar, "Subwavelength Topological Edge States in Optically Resonant Dielectric Structures," *Phys. Rev. Lett.* **114**, 123901 (2015).

11. X. Cheng, C. Jouvaud, X. Ni, S. H. Mousavi, A. Z. Genack, and A. B. Khanikaev, “Robust reconfigurable electromagnetic pathways within a photonic topological insulator,” *Nature Materials* **15**, 542 (2016).
12. B. Bahari, R. Tellez-Limon, and B. Kante, “Topological terahertz circuits using semiconductors,” *Appl. Phys. Lett.* **109**, 143501 (2016).
13. M. Hafezi, E. A. Demler, M. D. Lukin, and J. M. Taylor, “Robust optical delay lines with topological protection,” *Nature Physics* **7**, 907 (2011).
14. B. Bahari, A. Ndao, F. Vallini, A. El Amili, Y. Fainman, and B. Kante, “Nonreciprocal lasing in topological cavities of arbitrary geometries,” *Science* **358**, 636 (2017).
15. P. St-Jean, V. Goblot, E. Galopin, A. Lemaître, T. Ozawa, L. Le Gratiet, I. Sagnes, J. Bloch, A. Amo, “Lasing in topological edge states of a one-dimensional lattice,” *Nature Photonics* **11**, 651 (2017).
16. G. Harari, M. A. Bandres, Y. Lumer, M. C. Rechtsman, Y. D. Chong, M. Khajavikhan, D. N. Christodoulides, M. Segev, “Topological insulator laser: Theory,” *Science* **359**, eaar4003 (2018).
17. M. A. Bandres, S. Wittek, G. Harari, M. Parto, J. Ren, M. Segev, D. N. Christodoulides, M. Khajavikhan, “Topological insulator laser: Experiments,” *Science* **359**, eaar4005 (2018).
18. M. Parto, S. Wittek, H. Hodaei, G. Harari, M. A. Bandres, J. Ren, M. C. Rechtsman, M. Segev, D. N. Christodoulides, and M. Khajavikhan, “Edge-mode lasing in 1D topological active arrays,” *Phys. Rev. Lett.* **120**, 113901 (2018).
19. H. Zhao, P. Miao, M. H. Teimourpour, S. Malzard, R. El-Ganainy, H. Schomerus, and L. Feng, “Topological hybrid silicon microlasers,” *Nature Communications* **9**, 981 (2018).
20. L. Bi, J. Hu, P. Jiang, D. H. Kim, G. F. Dionne, L. C. Kimerling, and C. A. Ross, “On-chip optical isolation in monolithically integrated non-reciprocal optical resonators,” *Nature Photonics* **5**, 758-762 (2011).

Chapter 4: Topological OAM

4.1. Introduction

The idea of an extrinsic orbital angular momentum (OAM) associated with light was proposed by Allen et al. in 1992 [1]. He showed that light beams with an azimuthal phase dependence of $\exp(i\ell\theta)$ carry an associated angular momentum which is independent of the polarization state. In this phase factor, ℓ indicates the topological charge and can carry any positive or negative integer values. Beams that possess orbital angular momentum, have found uses in many fields such as optical tweezers, image processing, quantum information and communications, phase contrast microscopy, spin speed detection, and spiral interferometry [2-9]. Helically phased beams can be generated with several different techniques such as using spiral phase plates, cylindrical lens converter, Q-Plates, planar metasurfaces, holograms, or spatial light modulation (SLM) [10-21]. However, most of the aforementioned generation techniques are challenging to implement when topological charges ℓ increase. The lack of a limit to the theoretically possible topological charge which a beam can possess, and the inherent orthogonality between different angular momentum states make beams with OAM very

appealing in a number of fields such as high capacity quantum communication, and quantum entanglement [22-26]. However, historically practical generation of large ℓ numbers has proven difficult. With many techniques limited by geometrical or manufacturing considerations such as spatial bandwidth (in the case of SLMs) or milling precision in the case of spiral phase plates. To date, there have been few attempts to generate large topological charges [25-27]. Among them, Fickler et al. used spiral phase plates with large OAM of up to $\ell=10,010$ [25]. In all of these approaches, the devices are bulky and/or non-integrated.

In the previous chapter, we developed topological cavities that can emit light in one-way, while they maintain their functionality when deforming the geometry of the cavity. Since the dispersion curve of the edge mode is in the scattered region of the band diagram (Fig. 3-2 and 3-7), thus the edge mode is a leaky mode, and it partially scatters out in the normal direction. Therefore, when we remove the trivial waveguide, the only way to emit amplified light is toward the normal axis, which means that laser devices switch from the in-plane mode to the out-of-plane mode. In this chapter, we demonstrate, for the first time, the creation of a chip integrable beam generator utilizing an integrated photonic topological ring resonator. We discuss how this leaky unidirectional wave can help to generate structured beams with very large

topological charges without using any secondary component. Also, since the structure is planar, we are able to integrate many of these concentric topological ring resonators to multiplex many different large OAM beams. We also study the lasing dynamic of the topological rings using second-order correlation measurement, which gives us enough insights about the functionality of the devices.

4.2. Theoretical Design of Topological Rings

Our approach to generating beams with OAM is based on using an active topological ring resonator. Ring resonators are able to excite whispering gallery modes (WGMs) with large angular momenta, but because these modes are excited in pairs, i.e., clock-wise (CW) and counter clock-wise (CCW), the net angular momenta usually sums to zero. Therefore, it is necessary to suppress the rotational symmetry of the system, e.g., by breaking parity-time symmetry at the exceptional point [28], to create a beam with net angular momentum. Once a unidirectional WGM is excited, it can be out-coupled by a proximate scattering element such as a grating with a periodic refractive index close to it [29].

Here we use a topological insulator edge waveguide (as the previous chapter) to excite one-way chiral edge states. In chiral edge states, the group

velocity is in one direction, which is as a result of topological properties of PhC structures with non-trivial band gaps [30-33].

In our device, which is presented schematically in Fig. 4-1, we use two distinct PhCs to form a ring resonator. Similar to the topological cavities that we studied before, the PhC that is inside the ring is a star-shaped unit cell with a square lattice, and it is designed to have a topologically non-trivial band gap. The PhC that is outside of the ring is an air hole unit cell with a triangular lattice, and it is designed to have a topologically trivial band gap. Both PhCs are made of InGaAsP MQWs that are bonded on a magnetic material of YIG. When the chiral edge state is excited at the interface between the two PhCs, since the Chern number difference between them is non-zero ($|\Delta C| = 1$), then the edge mode propagates in one direction either CW or CCW depending on the direction of EMF. The number of edge modes is equal to the Chern number difference of side walls [34]. Therefore, since the Chern number difference is one, only one edge mode can propagate at the interface of both PhCs, i.e., it is thus a single optical mode.

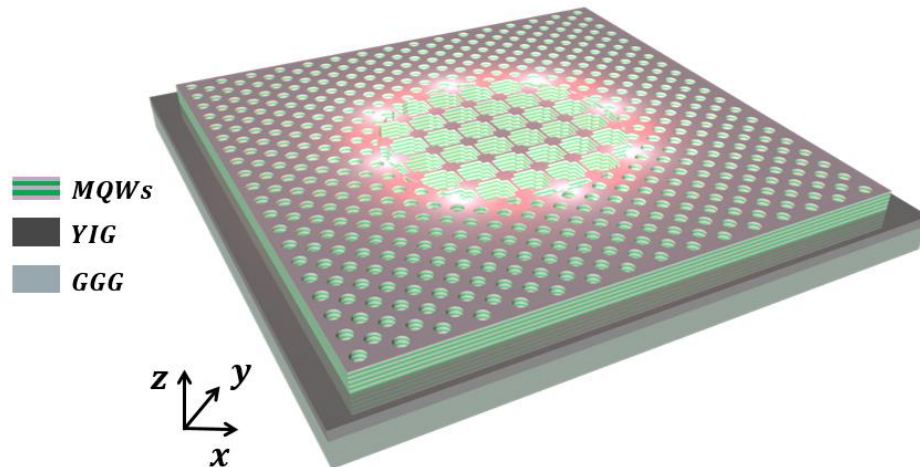


Figure 4-1 | Schematic of a topological ring formed at the interface of two PhCs. Both PhCs are patterned on InGaAsP MQWs, which is bonded on YIG grown on GGG. The PhC that is inside the ring is a star-shaped unit cell with a square lattice, and the PhC that is outside the ring is a triangular lattice unit cell with a cylindrical air hole at the center. The square lattice PhC has a non-trivial band gap while the triangular PhC has a large trivial band gap. Thus, the edge mode is unidirectional due to the distinct topological phase transitions at both PhCs. By optically pumping the entire structure, in the presence of an EMF, one-way edge mode with a large WGM number is excited and circulates inside the ring. The edge mode is bonded in the in-plane due to the photonic band gaps, but it can scatter out in the out-of-plane direction. Thus, as it amplifies inside the ring, it partially out-couples generating OAM beam with very large topological charge.

When both photonic crystal lattices are optically pumped, an edge mode which has a frequency within the band gap of both PhCs is excited and confined at the interface between the two crystals. However, since the crystals are not fully bounded in a direction normal to the plane of the crystal layer, the modes partially scatter out. In non-topological ring resonator designs with fully guided WGM [28,29], they have required a grating to create enough scattering into propagating fields. The current design is advantageous since

no additional complexity is required to create a radiative source because WGM is naturally a leaky mode. Therefore, the generated mode index is exactly the azimuthal number of the WGM, or more physically the number of optical periods around the resonator ring. It is, therefore, possible to generate very large topological charges (or ℓ numbers) in a confined space with a high mode purity. The topological charge can change as a function of the radius of the ring as shown in Fig. 4-2.

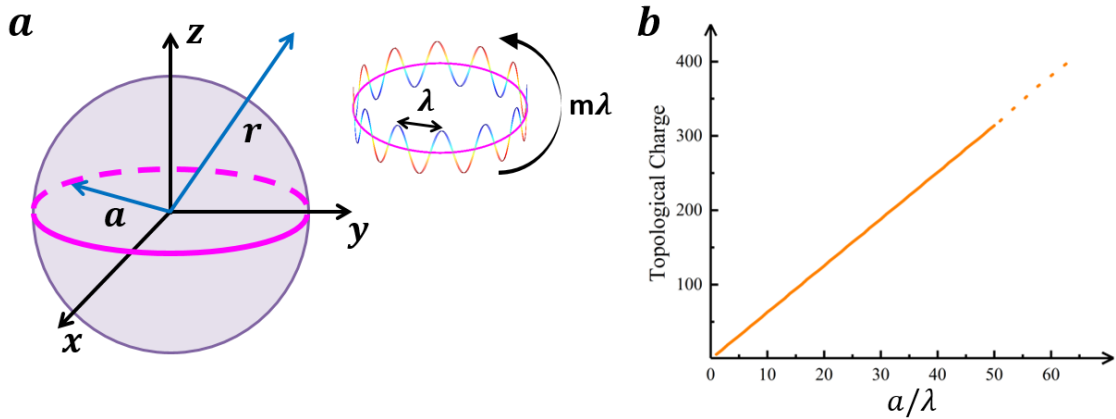


Figure 4-2 | (a) Schematic of a ring-resonator of radius a . The propagating mode can be in-plane or out-of-plane modes. The cavity length is $m\lambda$ (inset), where m is an integer representing the azimuthal order of the WGM and λ the guided wavelength in the ring. Since the cavity is leaky, the topological charge ℓ is the same as WGM order m . (b) Topological charge as a function of the normalized radius of the ring. By increasing the radius of ring, the order of the WGM increases, thus topological charge increases following the relation of $\ell = 2\pi a/\lambda$.

Figure 4-3a shows the field intensity distribution of the OAM mode for $\ell = 100$. By interfering this mode with another OAM beam with opposite charge

(i.e. $\ell = -100$), an interference pattern with fringes appears in which the number of fringes is 2ℓ (Fig. 4-3b).

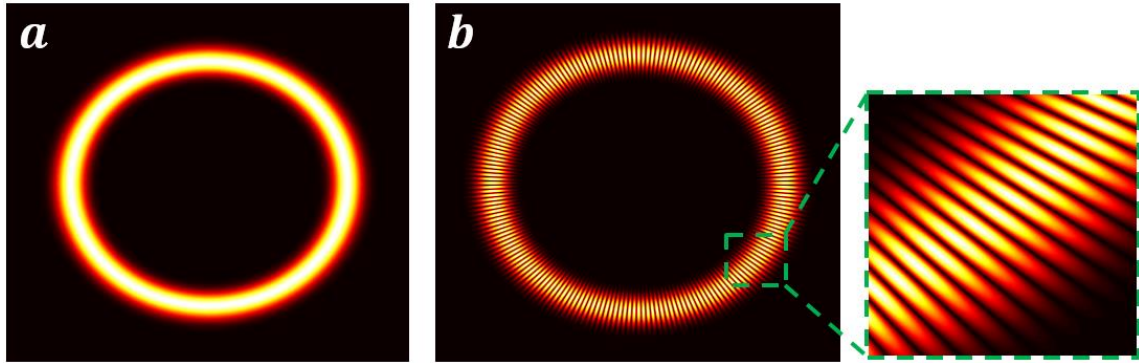


Figure 4-3 | (a) Field intensity profile of an OAM mode with $\ell = 100$. (b) The interference pattern of two OAM beams with the opposite ℓ numbers (i.e., ℓ and $-\ell$). The number of fringes in the interference pattern is equal to 2ℓ .

4.3. Device Fabrication

With the same fabrication process that was explained in detail in the previous chapter, the device structure is fabricated by electron beam lithography followed by dry etching to form both PhCs. The PhCs are subsequently bonded on a flat YIG substrate coated with a thin layer of polymethyl methacrylate. Finally, the InP substrate, on which InGaAsP is epitaxially grown, is removed by wet etching using hydrochloric acid. Figure 4-4 presents a top view SEM of a fabricated device. The fabrication is uniform over the entire area of the device.

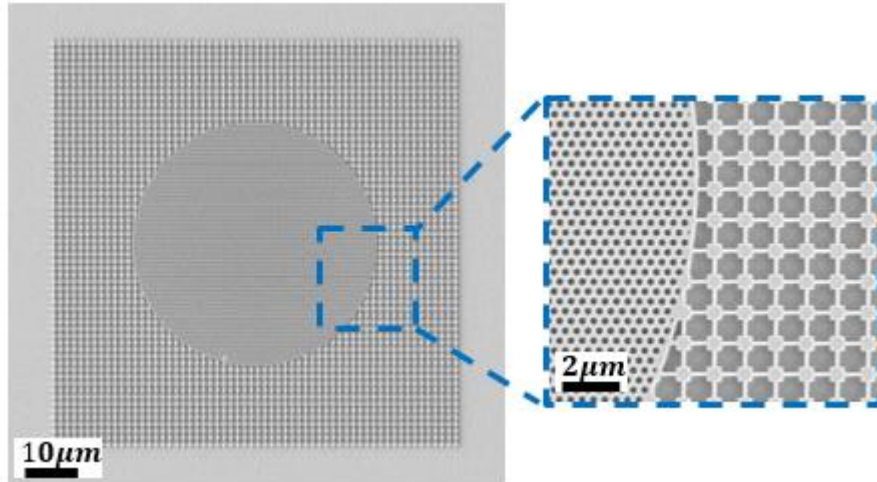


Figure 4-4 | Top view SEM of a topological ring formed by trivial and non-trivial PhCs. The structure is fabricated on InGaAsP by electron beam lithography followed by dry etching and then bonded on a YIG substrate with a thin layer of polymethyl methacrylate. The InP substrate is subsequently removed by wet etching using hydrochloric acid. In the inset, both trivial and non-trivial PhCs are seen clearly.

4.4. Device Characterization

To experimentally characterize the devices, a micro-photoluminescence setup is used. The sample is optically pumped from the top with a pulsed laser ($\lambda_{\text{pump}} = 1064 \text{ nm}$, $T = 12 \text{ ns}$ pulse at a repetition rate of 275 kHz). The size of the pump beam is controlled to cover the whole area of the device. The stimulated emission of the laser is collected using the same objective lens and directed toward a monochromator for spectrum analysis or toward IR camera for field intensity measurement.

4.4.1. Far-field and Interference Imaging

Figure 4-5 presents the far-field intensity and interference pattern of a topological ring shown in Fig. 4-4. The optical length of the ring resonator is optimized to obtain $\ell = 100$. Figure 4-5a shows the real space camera image of the far-field intensity of the device for a pump power density of $\rho = 1.03 \mu W/\mu m^2$. Clearly, an edge mode localized at the interface between the two PhCs is observed while the center is dark. By interfering the beam with its opposite ℓ number (i.e.,

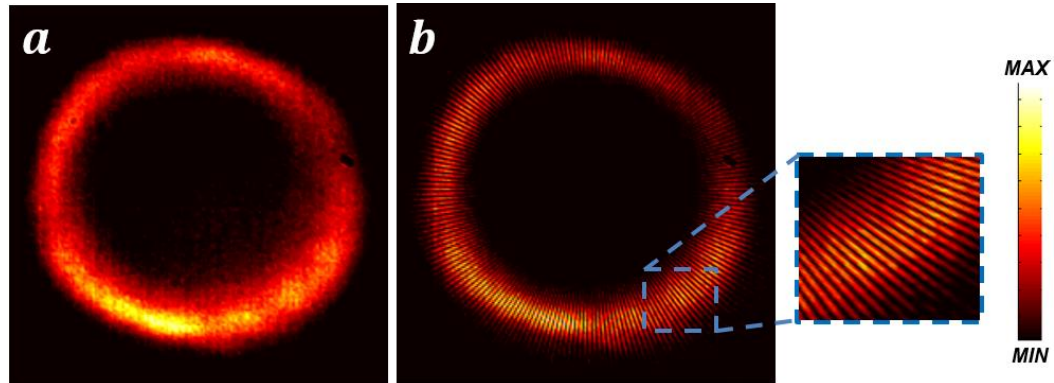


Figure 4-5 | (a) Real-space camera image of the emission from the topological ring when it is optically pumped from the top with an optical power density of $\rho = 1.03 \mu W/\mu m^2$ and EMF of $B_0 = +100 Oe$. (b) Interference pattern of the far-field emission with its opposite topological charge of $\ell = -100$. In the interference pattern, fringes appear because the beam carries orbital angular momentum, and the total number of fringes are 200 which means that topological charge is $\ell = 100$.

$\ell = -100$), fringes appear because beam carries orbital angular momentum (Fig. 4-5b). The number of fringes in Fig. 4-5b is 200 as it has topological charge of $\ell = 100$.

4.4.2. Photoluminescence Measurement

Figure 4-6 shows the photoluminescence spectrum of the optically pumped topological ring in the presence of EMF in three different regimes. The amplification and selection of a single mode at the wavelength of $\lambda = 1575 \text{ nm}$ are observed with increasing pump power. Figure 4-6b presents the log-scale output power as a function of the pump power density (light-light curve) and shows a characteristic lasing behavior.

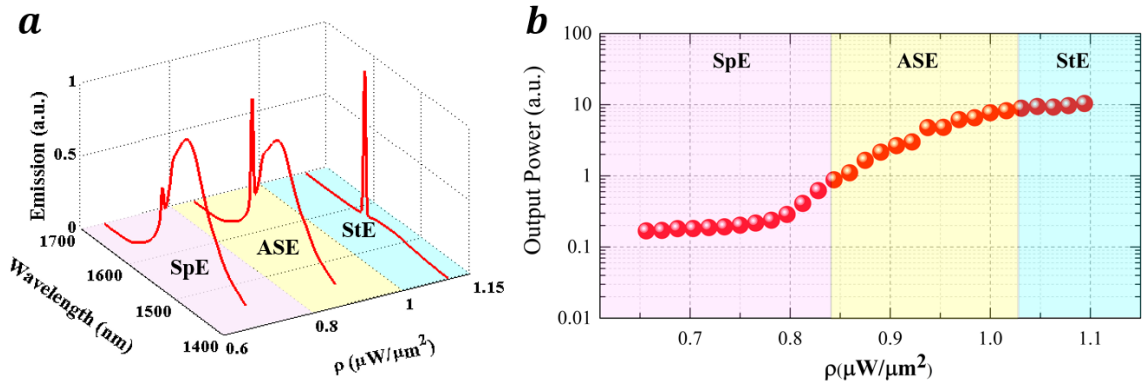


Figure 4-6 | (a) Photoluminescence of the topological ring for three different pump powers as a function of the wavelength. The topological ring is optically pumped with a pump laser ($\lambda_{pump} = 1064 \text{ nm}$) from the top, and the emission is collected using the same objective lens used for pumping on top of the ring. (b) Evolution of the output power as a function of pump power density. Red dots are experimental measurements of the output power for different pump power densities when the EMF is turned on. Three different highlighted areas are spontaneous emission (pink), amplified spontaneous emission (yellow), and stimulated emission (blue) ranges.

4.4.3. Second Order Correlation Measuring

To further investigate the coherent character and lasing characteristic of the cavity, we measured the second-order intensity correlation function of its

emission, $g^2(\tau) = \frac{\langle I(t)I(t+\tau) \rangle}{\langle I(t) \rangle^2}$, using a Hanbury Brown-Twiss interferometer (see appendix 2). $\langle I(t) \rangle$ represents the expectation value of the intensity at time t . Figure 4-7 shows the zero-delay of the normalized second-order intensity correlation function, $g^2(0)$, and the three different regimes of spontaneous emission (SpE), amplified spontaneous emission (ASE), and stimulated emission (StE) are evidenced. We observe the suppression of the photon bunching peak (visible in the ASE regime) in the StE regime, i.e., lasing action.

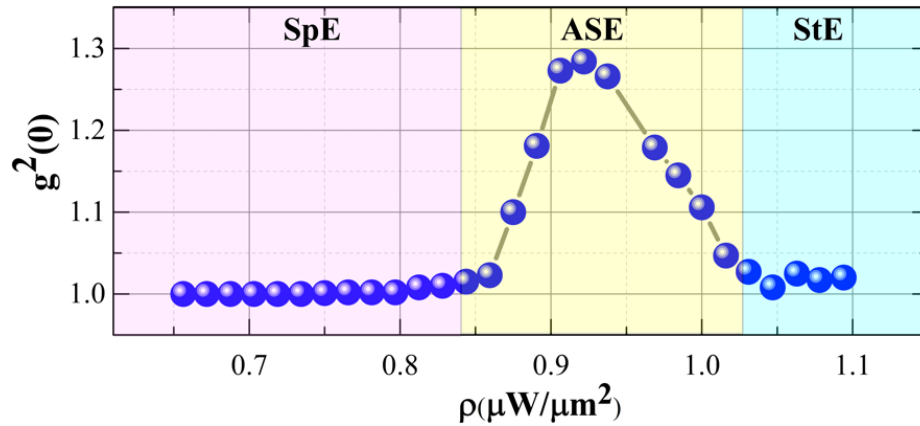


Figure 4-7 | Second-order intensity correlation at the zero-delay, $g^2(0)$. Clearly, the photon bunching peak (in the ASE regime of $g^2(0)$) is suppressed in the StE regime, demonstrating lasing action of the topological ring.

Figure 4-8 shows the experimental correlation histogram (Figs. 4-8a-e) and the corresponding normalized $g^2(\tau)$ (Fig. 4-8f-j) at five different pump power densities.

Due to nanosecond pulse pumping (290 kHz repetition rate, 6 ns pulse width), the correlation histogram inherently consists of many pulses corresponding to the optical pump pulses arriving, and the device is turning on. The time delay between neighboring pulses in Fig. 8a-e is approximately $3.4 \mu\text{s}$, which is consistent with the 290 kHz repetition rate of the pump laser. According to coherence theory, a photon bunching peak near zero-delay can be observed in $g^2(\tau)$ for a lasing device in the SpE and ASE regimes where the degree of coherence is low [35]. The width of the photon bunching peak is on the order of the coherence time [35], which is expected to be much smaller than the repetition period of the pump laser ($\sim 3.4 \mu\text{s}$). Therefore, the photon bunching peak will emerge only on top of the zero-delay pulse, making it taller than the non-zero-delay pulses (Fig. 4-8b-d). In the lasing regime, such a photon bunching peak is suppressed since coherent emission is achieved [35]. This is clearly demonstrated in Fig. 4-8e.

The photon bunching peak can be more readily observed in the normalized $g^2(\tau)$, which is obtained by dividing the zero-delay pulse by the mean of the non-zero-delay pulses. The mean is taken here to reduce the effect of shot noise in the experiment. Figure 4-8f-j show examples of the normalized $g^2(\tau)$ in the SpE (Fig. 4-8f), ASE (Fig. 4-8g-i) and StE (Fig. 4-8j) regimes of our topological laser. Evidently, the photon bunching peak

visible in the ASE regime is suppressed in the StE regime. However, contrary to theoretical predictions, the photon bunching is also absent in the SpE regime (Fig. 4-8a,f). This experimental phenomenon is primarily due to the timing uncertainty of our APDs', which is on the order of 100 ps. Since the coherence time in the SpE regime is much shorter than 100 ps, the averaging effect from the APDs renders the photon bunching peak invisible.

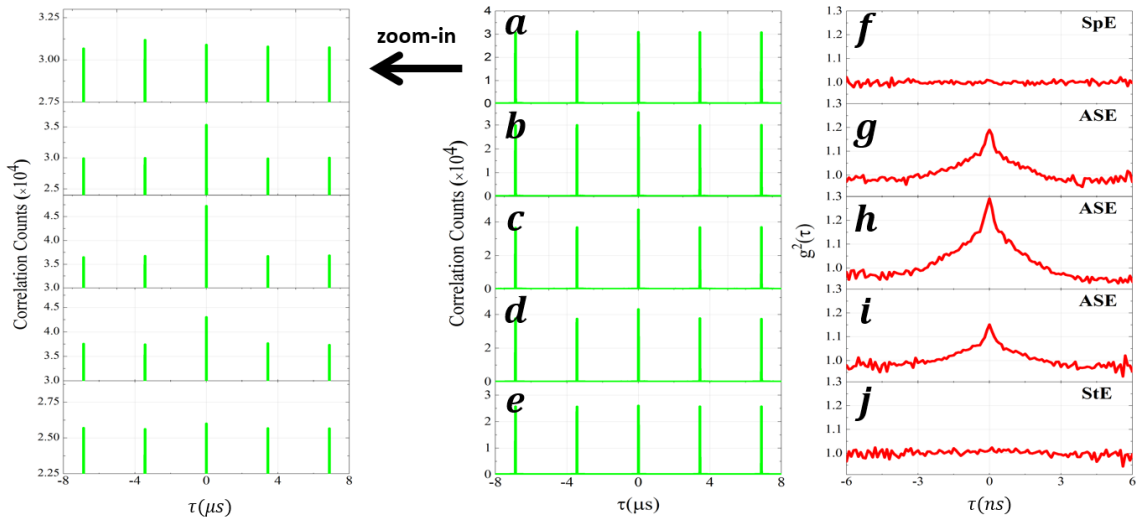


Figure 4-8 | Intensity correlation histograms (a-e), and the corresponding normalized $g^2(\tau)$ (f-j) in the SpE, ASE and StE regimes. The photon bunching peaks emerge in the ASE regime (b-d, g-i) signifying that stimulated emission begins to dominate in our topological laser as it transitions into the StE regime. At the highest pump power density (e,j), the photon bunching peak is suppressed due to lasing. In the SpE regime (a,f); however, the photon bunching peak is absent because the coherence time is too short to be resolved by the APDs.

4.4.4. Full Wave Half Maximum Measuring

Furthermore, the full width at half maximum (FWHM) of the zero-delay $g^2(\tau)$ pulse shrinks in the SpE regime, reaches a minimum in the ASE

regime, and broadens in the StE regime (Fig. 4-9). Such variations in the $g^2(\tau)$ pulse width is related to a nonlinear effect called delay threshold phenomenon or dynamical hysteresis, which occurs in a laser only when the peak intensity of a pump pulse is larger than the threshold intensity [36]. The distinct $g^2(\tau)$ width behaviors in the SpE and StE regimes signify that the suppression of the photon bunching peak (Fig. 4-7) at high pump intensity indeed originates from lasing instead of SpE. It is worth noting that the unity $g^2(0)$ in the SpE regime is due to the limited time resolution of the detection system as explained before [36].

Figure 4-7 was acquired by extracting the zero-delay value, i.e., $g^2(0)$, of the normalized $g^2(\tau)$ in a wide range of pump powers. By $g^2(0) \sim 1$ in both the SpE and StE regimes, confirms that our device indeed reached the lasing regime for two reasons. Firstly, the output power of our device continued to increase even at the highest pump intensities. Hence, it's impossible that the device reverses back to the SpE regime due to, for example, degradation as that should lead to a significant decline in the output power. Furthermore, we examined the FWHM of the $g^2(\tau)$ pulses as a function of the pump power (Fig. 4-9). In a previous study [36], it was demonstrated that when a laser is optically pumped with nanosecond pulses, its $g^2(\tau)$ pulse FWHM shrinks in the SpE regime, reaches a minimum in the

ASE regime and broadens in the StE regime. Such variations in the $g^2(\tau)$ pulse width is related to a nonlinear effect called the delay threshold phenomenon (DTP) or dynamical hysteresis (DH), which occurs in a laser only when the peak intensity of a pump pulse is larger than the threshold intensity [36,37]. Therefore, an indirect observation of DTP via the $g^2(\tau)$ pulse width unambiguously shows lasing. The measured $g^2(\tau)$ pulse FWHM of our topological laser is shown in Fig. 4-9. The trends of the FWHM in the SpE, ASE and StE regimes are fully consistent with previous work [36]. We further measured the $g^2(\tau)$ pulse FWHM of our pump laser at different pump powers to ensure that the shrinkage and broadening effects are not due to anomalies of the pump laser. Figure 4-9 clearly shows that the $g^2(\tau)$ pulse FWHM of the pump laser stays constant at all pump powers while that of the topological laser varies significantly. Consequently, the notable variation in the $g^2(\tau)$ pulse width results solely from the emission characteristics of our topological laser.

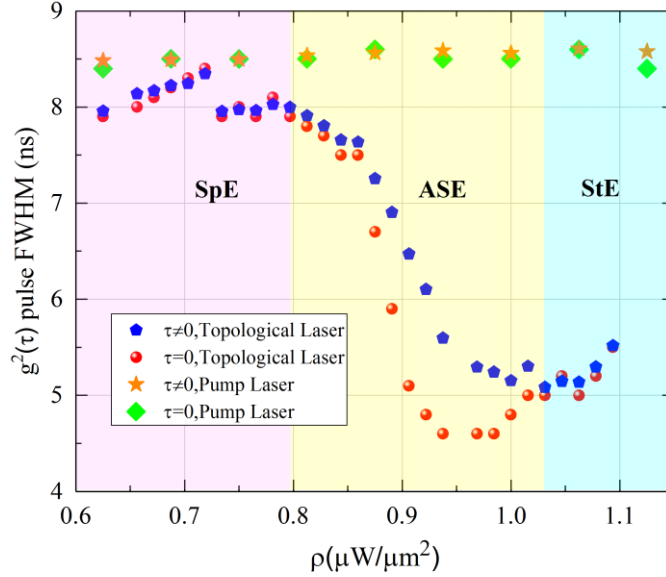


Figure 4-9 | The pulse FWHM of the topological device is plotted along with that of the pump laser. Evidently, the $g^2(\tau)$ width of the pump laser stays nearly constant while that of the topological laser varies significantly. Therefore, the device width variations are due solely to the distinctive emission statistics in the SpE, ASE and StE regimes of the topological laser, and are not correlated with the operation of the pump laser.

4.5. Multiplexing Multiple Topological Rings

By putting alternatively trivial and non-trivial PhCs in a concentric coaxial pattern as depicted in Fig. 4-10, we are able to generate different momentum states and multiplex the beams together as desired. Each concentric ring is operating at the same optical frequency (i.e. within the band gap of both PhCs), and has the same optical path length but with different topological charges (shown in Fig. 4-2b), which results in different sized cavities.

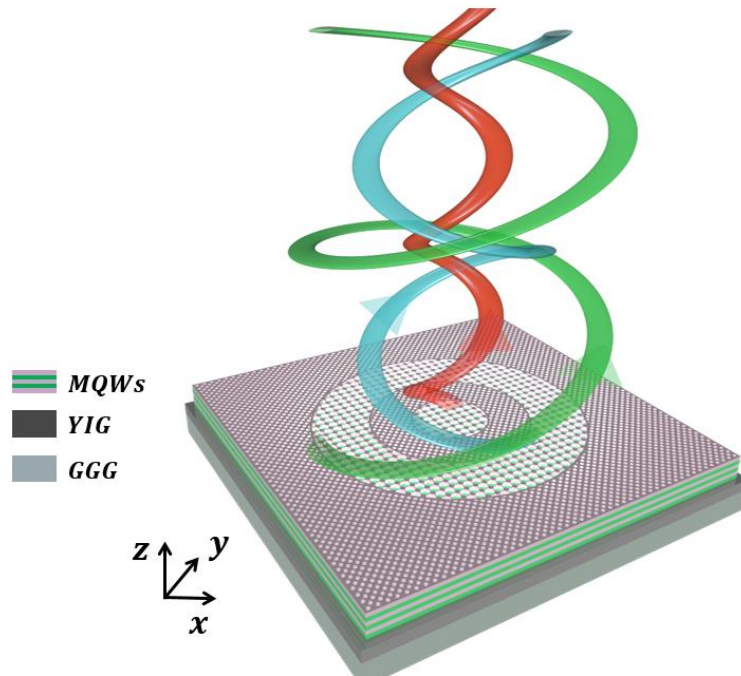


Figure 4-10 | Schematic of a topological multiplexer formed by placing three different topological rings in which trivial and non-trivial PhCs change alternatively in a concentric coaxial pattern. By pumping the whole structure, all the rings are excited with the same wavelength but with different topological charges realized by the radius of the ring, $a = \ell\lambda$, where ℓ and λ are topological charge and the optical wavelength of the ring, respectively.

By using the topological ring depicted in Fig. 4-1, we can integrate many concentric ring resonators to multiplex many different large OAM beams. Figure 4-11a-c shows the SEM images of three different planar rings designed for topological charges of 100, 156, and 276, for example. By combining these three rings we can multiplex all of them in one planar multi-ring structure (Fig. 4-11d).

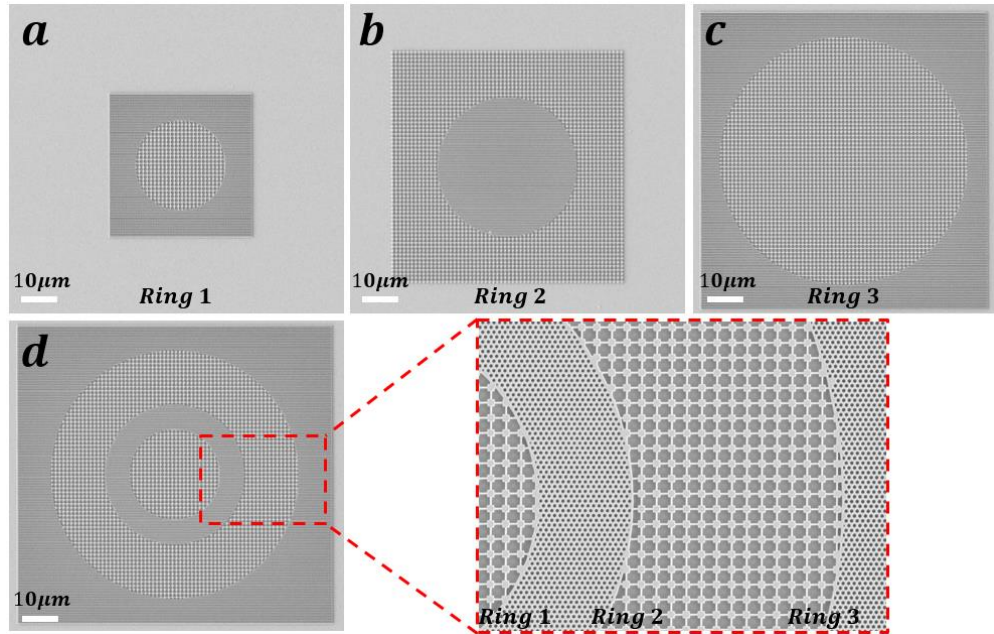


Figure 4-11 | Top view SEM images of three different topological rings designed for topological charges of 100, 156, and 276. In two rings shown in (a) and (c) the PhC inside the ring is a non-trivial PhC and the PhC outside of the ring is a trivial PhC. The structure shown in (b) is complementary of (a) and (c), i.e., PhC that is enclosed by the ring is a trivial PhC and elsewhere is a non-trivial PhC. (d) By merging all structures in (a-c) while they are concentric, we can multiplex three rings in the same planar platform.

Figure 4-12 show the far-field image of the topological rings, and clearly, all the OAM beams indicated in Fig. 4-12a-c are multiplexed in Fig. 4-12d without cross-talking with each other.

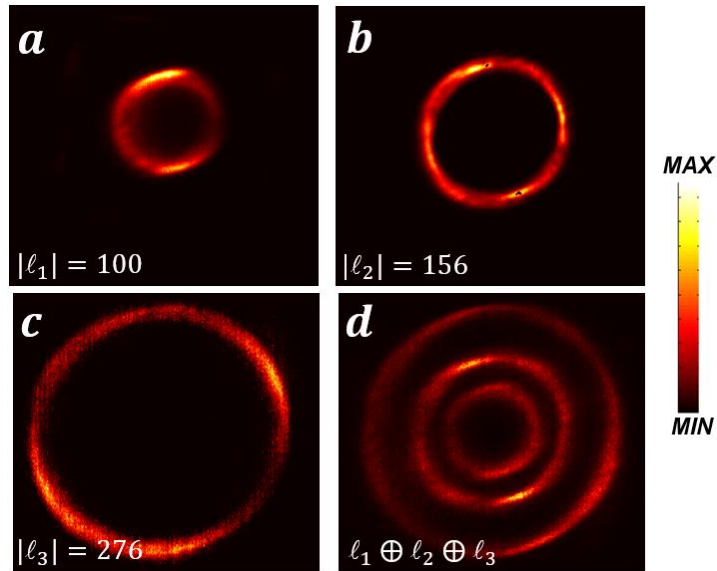


Figure 4-12 | (a-c) Real-space camera images of the rings when they optically pumped with an optical pump power density of $\rho = 1.03 \mu\text{W}/\mu\text{m}^2$. All three rings (a-c) are lasing and present clear ring-shape patterns (a-c) that are multiplexed (d) when three rings are merged concentrically.

Figure 4-13 and 4-14 present similar interference patterns that are measured for each ring shown in Fig. 4-12.

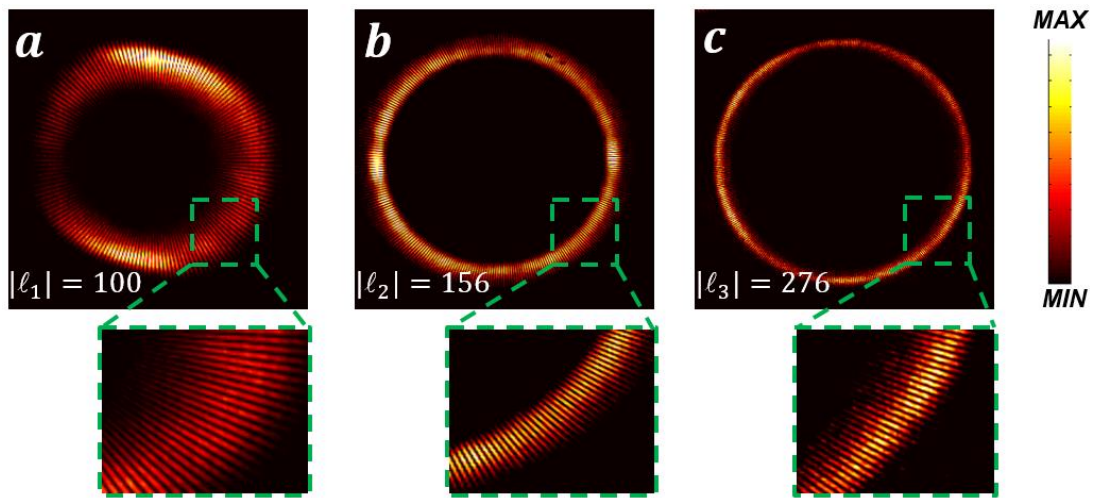


Figure 4-13 | Field intensity profile of the beam when it interferes with an OAM beam with the opposite ℓ number ($-\ell$). The total number of the fringes are 200 (a), 312 (b), and 552 (c).

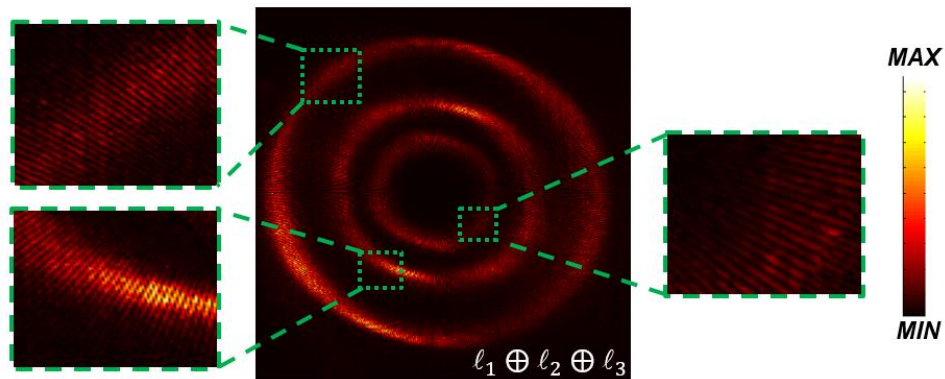


Figure 4-14 | Field intensity profile of the beam when it interferes with an OAM beam with the opposite ℓ number ($-\ell$). All three rings in Fig. 4-13 are multiplexed with the same number of fringes.

4.6. Chapter Summary

In conclusion, we experimentally demonstrated a photonic topological ring resonator that is able to generate beams with arbitrarily large OAM. The ring is formed by using two PhCs with distinct topological phase invariants, supporting a unidirectional chiral edge state in the ring. PhCs are made of

InGaAsP MQWs bonded on a YIG substrate that breaks time-reversal symmetry. By optically pumping the entire structure, stimulated emission from one-way edge mode is excited and amplified. Unlike conventional ring resonators that they need an additional grating to scatter out the WGM, in this topological ring the WGM partially out-couples as circulating inside the ring. Therefore, the OAM number is the same as WGM number, which is a very large value. We also integrated many of these planar topological rings with various topological charges when they have same center to multiplex different large OAM beams.

Our experimental results offer new all integrated and planar OAM light sources that are able to generate very large OAM beams useful for optical communications, and quantum mechanics. Furthermore, the planar geometry and small size of the device lend themselves to on-the-chip integration, multiplexing, and waveguiding applications.

Chapter 4, in part, is a reprint of the material as it appears in B. Bahari, L. Hsu, S. H. Pan, D. Preece, A. Ndao, A. El Amili, Y. Fainman, and B. Kanté, “Topological lasers generating and multiplexing topological light,” *arXiv:1904.11873* (2019), and B. Bahari, and B. Kanté, “Topological integration of unbounded orbital angular momentum laser,” United States

patent (Under process), 2018. The dissertation author was the primary researcher and author of this paper and patent.

References

1. L. Allen, M. W. Beijersbergen, R. J. C. Spreeuw, and J. P. Woerdman, "Orbital angular momentum of light and the transformation of Laguerre-Gaussian laser modes," *Phys. Rev. A* **45**, 8185 (1992).
2. M. Dienerowitz, M. Mazilu, P. J. Reece, T. F. Krauss, and K. Dholakia, "Optical vortex trap for resonant confinement of metal nanoparticles," *Optics Express* **16**, 4991 (2008).
3. L. Paterson, M. P. MacDonald, J. Arlt, W. Sibbett, P. E. Bryant, and K. Dholakia, "Controlled Rotation of Optically Trapped Microscopic Particles," *Science* **292**, 912-914 (2001).
4. H. He, N. R. Heckenberg, and H. Rubinsztein-Dunlop, "Optical Particle Trapping with Higher-order Doughnut Beams Produced Using High Efficiency Computer Generated Holograms," *J. Mod. Opt.* **42**, 217 (1995).
5. K. Crabtree, J. A. Davis, and L. Moreno, "Optical processing with vortex-producing lenses," *Appl. Opt.* **43**, 1360 (2004).
6. J. M. Hickmann, E. J. S. Fonseca, W. C. Soares, and S. Ch´ave Cerda, "Unveiling a Truncated Optical Lattice Associated with a Triangular Aperture Using Light's Orbital Angular Momentum," *Phys. Rev. Lett.* **105**, 053904 (2010).
7. S. Furhapter, A. Jesacher, S. Bernet, and M. R. Marte, "Spiral phase contrast imaging in microscopy," *Optics Express* **13**, 689 (2005).
8. M. P. J. Lavery, F. C. Speirits, S. Barnett, and M. J. Padgett, "Detection of a spinning object using light's orbital angular momentum," *Science* **341**, 537-540 (2013).
9. A. Jesacher, S. Furhapter, S. Bernet, and M. R. Marte, "Spiral interferogram analysis," *J. Opt. Soc. Am. A* **23**, 1400 (2006).

10. M. W. Beijersbergen, R. P. C. Coerwinkel, M. Kristensen, and J. P. Woerdman, "Helical-wavefront laser beams produced with a spiral phaseplate," *Opt. Commun.* **112**, 321 (1994).
11. M. Uchida, and A. Tonomura, "Generation of electron beams carrying orbital angular momentum," *Nature* **464**, 737-739 (2010).
12. M. W. Beijersbergen, L. Allen, H. E. L. O. Van Der Veen, and J. P. Woerdman, "Astigmatic laser mode converters and transfer of orbital angular momentum," *Opt. Commun.* **96**, 123 (1993).
13. G. Biener, A. Niv, V. Kleiner, and E. Hasman, "Formation of helical beams by use of Pancharatnam-Berry phase optical elements," *Opt. Lett.* **27**, 1875 (2002).
14. L. Marrucci, C. Manzo, and D. Paparo, "Optical spin-to-orbital angular momentum conversion in inhomogeneous anisotropic media," *Phys. Rev. Lett.* **96**, 163905 (2006).
15. N. Yu, P. Genevet, M. A. Kats, F. Aieta, J. P. Tetienne, F. Capasso, and Z. Gaburro, "Light propagation with phase discontinuities: generalized laws of reflection and refraction," *Science* **334**, 333–337 (2011).
16. D. Lin, P. Fan, E. Hasman, and L. M. Brongersma, "Dielectric gradient metasurface optical elements," *Science* **345**, 298-302 (2014).
17. Y. Gorodetski, N. Shitrit, I. Bretner, V. Kleiner, and E. Hasman, "Observation of optical spin symmetry breaking in nanoapertures," *Nano Lett.* **9**, 3016-3019 (2009).
18. V. Y. Bazhenov, M. V. Vasnetsov, and M. S. Soskin, "Laser beams with screw dislocations in their wavefronts," *JETP Lett.* **52**, 429 (1990).
19. A. B. Stilgoe, A. V. Kashchuk, D. Preece, and H. Rubinsztein-Dunlop, "An interpretation and guide to single-pass beam shaping methods using SLMs and DMDs," *J. Opt.* **18**, 65609 (2016).
20. N. R. Heckenberg, R. McDuff, C. P. Smith, and A. G. White, "Generation of optical phase singularities by computer-generated holograms," *Opt. Lett.* **17**, 221 (1992).

21. D. Preece, E. Yao, G. M. Gibson, R. Bowman, J. Leach, and M. J. Padgett, "A spatial light phase modulator with an effective resolution of 4 mega-pixels," *J. Mod Opt.* **55**, 2945 (2008).
22. J. Wang, J. Y. Yang, I. M. Fazal, N. Ahmed, Y. Yan, H. Huang, Y. Ren, Y. Yue, S. Dolinar, M. Tur, and A. E. Willner, "Terabit free-space data transmission employing orbital angular momentum multiplexing," *Nature Photonics* **6**, 488 (2012).
23. M. J. Willner, H. Huang, N. Ahmed, G. Xie, Y. Ren, Y. Yan, M. P. J. Lavery, M. J. Padgett, M. Tur, and A. E. Willner, "Reconfigurable orbital angular momentum and polarization manipulation of 100 Gbit/s QPSK data channels," *Opt. Lett.* **38**, 5240 (2013).
24. A. Mair, A. Vaziri, G. Weihs, and A. Zeilinger, "Entanglement of the orbital angular momentum states of photons," *Nature* **412**, 313-316 (2001).
25. R. Fickler, G. Campbell, B. Buchler, P. K. Lam, and A. Zeilinger, "Quantum entanglement of angular momentum states with quantum numbers up to 10,010," *PNAS* **113**, 13642 (2016).
26. R. Fickler, R. Lapkiewicz, W. N. Plick, M. Krenn, C. Schaeff, S. Ramelow, and A. Zeilinger, "Quantum entanglement of high angular momenta," *Science* **338**, 640 (2012).
27. Y. F. Chen, Y. C. Lin, W. Z. Zhuang, H. C. Liang, K. W. Su, and K. F. Huang, "Generation of large orbital angular momentum from superposed Bessel beams corresponding to resonant geometric modes," *Phys. Rev. A* **85**, 043833 (2012).
28. P. Miao, Z. Zhang, J. Sun, W. Walasik, S. Longhi, N. M. Litchinitser, and L. Feng, "Orbital angular momentum microlaser," *Science* **353**, 464-467 (2016).
29. X. Cai, J. Wang, M. J. Strain, B. Johnson-Morris, J. Zhu, M. Sorel, J. L. O'Brien, M. G. Thompson, and S. Yu, "Integrated Compact Optical Vortex Beam Emitters," *Science* **338**, 363-366 (2012).

30. F. D. M. Haldane, and S. Raghu, “Possible realization of directional optical waveguides in photonic crystals with broken time-reversal symmetry,” *Phys. Rev. Lett.* **100**, 013904 (2008).
31. S. Raghu, and F. D. M. Haldane, “Analogues of quantum-Hall-effect edge states in photonic crystals,” *Phys. Rev. A* **78**, 033834 (2008).
32. Z. Wang, Y. Chong, J. D. Joannopoulos, and M. Soljačić, “Observation of unidirectional backscattering-immune topological electromagnetic states,” *Nature* **461**, 772 (2009).
33. B. Bahari, R. Tellez-Limon, and B. Kanté, “Topological terahertz circuits using semiconductors,” *Appl. Phys. Lett.* **109**, 143501 (2016).
34. Y. Hatsugai, “Chern number and edge states in the integer quantum Hall effect,” *Phys. Rev. Lett.* **71**, 3697 (1993).
35. R. Loudon, *The Quantum Theory of Light* (Oxford Univ. Press, New York, ed. 3, 2000).
36. S. H. Pan, Q. Gu, A. El Amili, F. Vallini, and Y. Fainman, “Dynamic hysteresis in a coherent high-Beta nanolaser,” *Optica* **3**, 1260 (2016).
37. T. Erneux, P. Glorieux, *Laser Dynamics* (Cambridge Univ. Press, New York, 2010), pp. 155-171.

Chapter 5: Bound States in the Continuum

5.1. Introduction

Cavity resonators are primarily used for generating single frequency beams with high intensities. These resonators conventionally consist of two mirrors to provide multiple reflections of beams. By controlling specific parameters such as optical path of beams and reflectivity of mirrors, wave with a specific frequency will be trapped, and experiences a very large quality factor defined as [1]

$$Q = \omega \times \frac{\textit{stored energy inside the cavity}}{\textit{dissipated power inside the cavity}}$$

where ω is angular frequency. There are very different kinds of cavity resonators with different functionalities rather than only using two mirrors.

Cavities play a fundamental role in nanophotonics. One key parameter in a cavity is the quality factor, which shows the lifetime of a photon inside the cavity. In many applications, especially in laser, a cavity with a large quality factor is desirable. Photonic crystal cavities can present a large quality factor [2], which makes them an interesting platform for photonic systems.

Generally, PhCs can be classified based on the number of periodicity directions (i.e., 1D, 2D or 3D), and thickness of the non-periodic directions (i.e., finite or infinite).

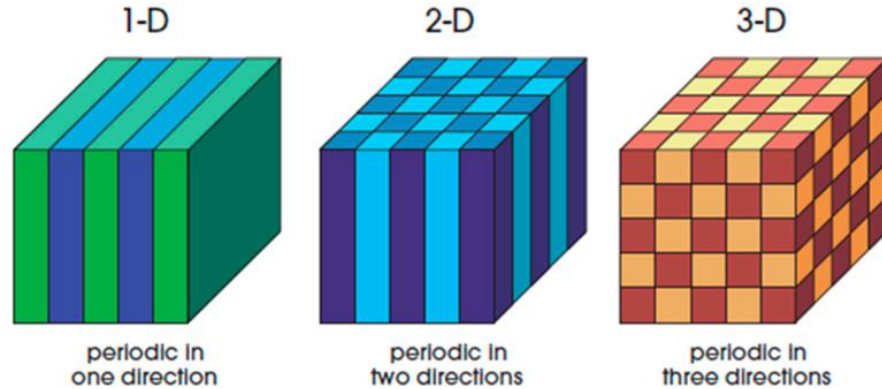


Figure 5-1 | schematic of 1D, 2D, and 3D PhCs (picture courtesy from reference [3]).

By assuming that there is no material loss, if the non-periodic directions have an infinite thickness, then eigenmodes of the PhC is purely real [3]. This means the quality factor of the modes which also is defined as, $Q = -2 \times Re\{\tilde{f}\}/Im\{\tilde{f}\}$, where \tilde{f} is complex eigenfrequency, is infinite. This happens simply because there is no scattering loss in the system. However, if non-periodic directions have finite thicknesses, then scattering loss can exist due to the diffractions [1]. In this case, in the band diagram there are two different regions that are separated by some lines called first diffraction limits (see Fig. 5-2). As shown in Fig. 5-2, in the gray area which also called light cone, the eigenmodes are purely real because these modes are below the first diffraction limit, and experience no diffraction and scattering loss. Therefore, the quality

factor of these modes is infinite, and we call those modes as “guided modes”. However, modes that are above this light cone (i.e., in the scattered or continuum region) have complex eigenmodes, which means that quality factor is a finite value. This is because these modes experience some sort of diffractions and scatter out of the system. Therefore, there are scattering losses. These modes are called “resonant or leaky modes”.

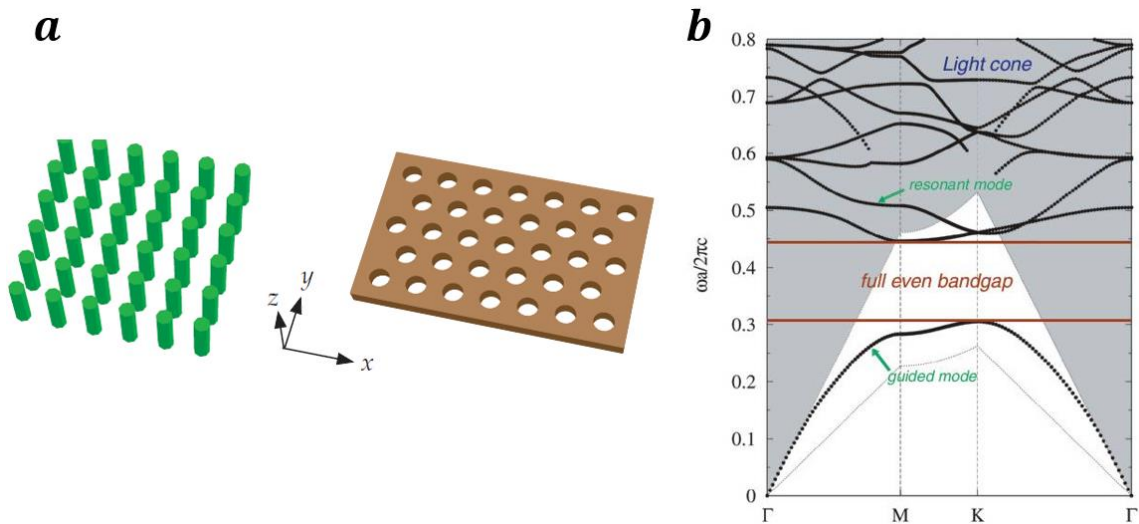


Figure 5-2 | (a) schematic of PhC slab with different configurations of either rod-base or hole-base, and different lattices of either square or triangular lattices (picture courtesy from ref. [3]). (b) Band diagram of a representative PhC slab. The white area is separated from the gray area using first diffraction limits indicating light cone. Modes sitting below the first diffraction limits are guided modes with real frequency and infinite quality factor, but mode beyond these limits are resonant modes with complex frequency and finite quality factors (picture courtesy from ref. [4]).

In 1929, von Neumann and Wigner demonstrated that the single-particle Schrodinger equation could have some embedded eigenvalues in the continuum of positive energy states, called bound states in continuum (BIC).

They showed the origin of these bound states using amplitude modulation of a free particle wave function [5]. Therefore, based on their demonstration, the potential was bounded and could be vanished at infinity. It was shown that destructive interference is the origin of this phenomena, and predicted in photonic systems [6], and experimentally demonstrated in the passive system [7] with applications in nanophotonic laser [8]. However, BIC singularities possess other peculiar features rather than only diverging quality factor due to the full confinement inside the structure.

In this chapter, we study the topological characteristics of BIC singularities and demonstrate theoretically and experimentally that BICs carry non-zero topological charges. This feature is the origin of tailored beam generation. Also, the position of the BIC singularities in reciprocal space is tunable under some specific conditions, which enables to change the beam direction in the real space. This is a unique characteristic that proposes the origin of a new type of non-mechanical beam steering technique that is quite different from conventional phase array systems studied by far [9-14]. Furthermore, in BIC devices it is possible to generate multiple beams at the same time thanks to the crystal symmetry of periodic structures. Combination of all these characteristics in a single-platform device enhances the

functionality of the light source, and can find many applications in optical communications, optical tweezers, sensors, and optical microscopy.

5.2. Theoretical Design of Extended PhC Cavity

Bound states in the continuums are singular points in the reciprocal space (or Brillouin zone) with a zero far-field intensity and a phase singularity. According to homotopy theory, for a singular point in a vector domain, there is a certain amount of vector winding for any closed path enclosed that singular point [15]. This amount indicates the strength of the singularity, and also called “topological charge”. Brillouin zone is a vector domain and a far-field polarization can be assigned to each point inside this domain. BIC points are singularities within this domain that are center of polarization vortices with non-zero topological charges calculated by [16]:

$$q = \frac{1}{2\pi} \oint_C \nabla_k \phi(k) \cdot dk, \quad (5-1)$$

where $\phi(k) = \text{arg}[c_x(k) + ic_y(k)]$, and c_x (c_y) is x (y) component of the averaged field, $\langle u_k \rangle$, and u_k is defined as the periodic part of the Floquet-Bloch modes, $E(r, k) = e^{ik \cdot r} u_k(r)$ with $u_k(r + p) = u_k(r)$, where p is periodicity.

At the BIC singularity, the far-field is zero due to the destructive interference of the resonant modes from different unit cells that have the same

amplitude but different Floquet-Bloch phases. By detuning the effective refractive index of unit cells uniformly, the momentum whose destructive interference happens will change. This is a fundamental key that is used for tuning the direction of emission beam as it will be discussed in the following.

An important question left is about polarization state at BIC point. As mentioned, at BIC points the far-field amplitude tends to be zero, thus theoretically it is meaningless to define a polarization state for these points. However, it can be shown for points so closed to a BIC singularity. This is especially can be done in an active system (laser), because when the system is pumped, eventually, a mode with the largest quality factor (i.e. BIC mode) that experiences larger effective mode gain starts to amplify and lase. Therefore, the far-field profile and polarization state can be evaluated.

Figure 5-3 presents a PhC slab made of InGaAsP MQWs that is bonded on a glass substrate using a resist of polymethyl methacrylate (PMMA).

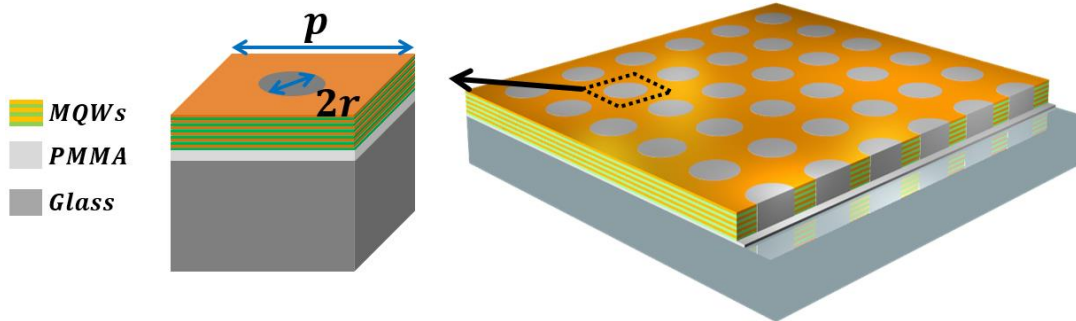


Figure 5-3 | schematic of the PhC slab made of InGaAsP MQWs bonded on a glass substrate using a PMMA resist. PhC has a square lattice with a periodicity of p , and radius of holes r .

5.2.1. Band Diagram Calculation

Dispersion band diagram and quality factor of this structure are plotted in Fig. 5-4. In these plots, modes of the PhC are calculated using finite element method. There are three modes in the gain bandwidth of the InGaAsP. Mode 1 is a single mode while modes 2 and 3 are degenerated modes. By changing the radius of holes uniformly over the whole structure, all three modes shift spectrally. The quality factor of mode 1 is theoretically infinite at the center of the Brillouin zone (Γ point) and independent of the radius of holes as mode 1 is symmetry protected and we call it Γ -locked mode. This type of mode, which usually referred to as band-edge mode, necessarily emits normal to the surface [9]. Modes 2 and 3, which are resonant modes, can only have infinite quality factors if all radiation channels destructively interfere to form singular states at reciprocal space points.

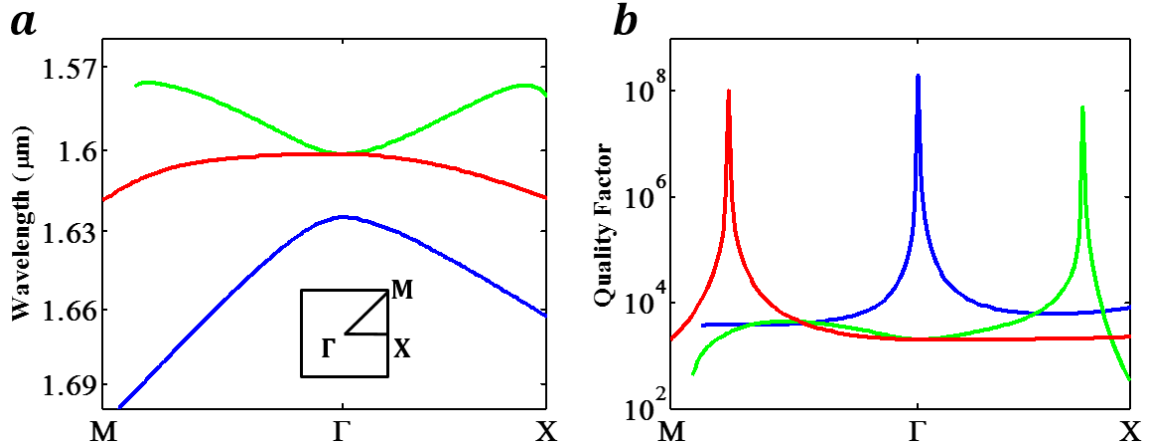


Figure 5-4 | Band diagram (a) and quality factor (b) of the square lattice PhC with a periodicity of $p = 950 \text{ nm}$, and radius of holes $r = 200 \text{ nm}$. Band diagram is calculated along the irreducible Brillouin zone. Blue mode is a single mode with a large quality factor always at Γ point (Γ -locked), while the other two modes are degenerated modes with a large quality factor that can move away from the Γ point.

5.2.2. Vortex Behavior of BIC Singularities

Although the far-field polarization does not exist right at these singular points, but it can be defined for points very close to the singularities. For example, let's consider mode 3 (green mode in Fig. 5-4b). As shown in the Brillouin zone (Fig. 5-5a) for every point close to the BIC singularity, there is a linear polarization but at different directions. The polarization at BIC point should be defined in a way that polarization continuity maintains by moving at different directions. This means that there is a polarization collapse right at BIC points, and this polarization (at a very close point to BIC) is a superposition of all neighboring polarizations. As it is demonstrated in Fig. 5-

5b, the far-field polarization is linear for a point away from BIC point. However, as we move toward the BIC point, the far-field polarization

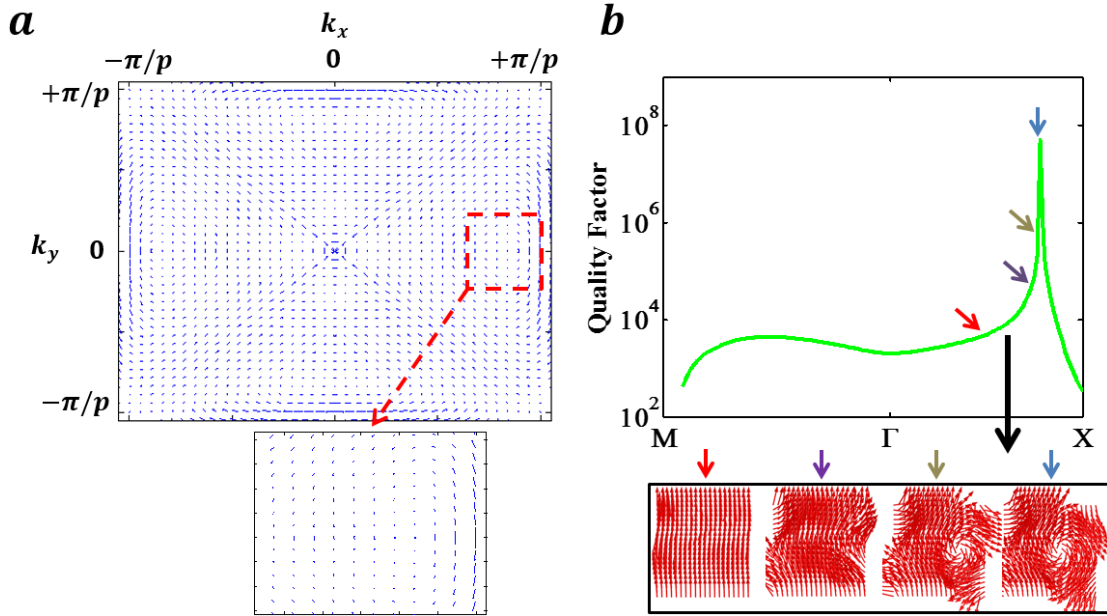


Figure 5-5 | (a) Polarization map of the PhC within the Brillouin zone at different momentum pairs (k_x, k_y) . At each point, polarization is linear but with different orientations. As moving toward BIC singularities (indicated by red dots), the size of the vectors (polarization amplitudes) decrease due to the vanishing far-field. Around the BIC singularity, there is a polarization rotation (vortex) due to the non-zero topological charge. Since there is one time vector winding, thus the topological charge is one. (b) Quality factor of mode 3 along irreducible Brillouin zone with a BIC singularity along ΓX . For points away from BIC the far-field polarization is linear, but as moving toward BIC singularity, the far-field polarization tends to be become vortex shape.

gradually changes to be vortex shape following the similar pattern of the vortex in Fig. 5-5a. The topological charge or winding number of this vortex can be calculated using eq. (5-1).

5.2.3. Robustness of BIC Singularities

These BIC singular states are robust vortex centers carrying non-zero topological charges (see Appendix 3), and a continuous change of effective refractive index (or physical parameters of a system) continuously tunes the destructive interference condition away from the Γ point, resulting in steering of mode 2 along ΓM and mode 3 along ΓX (see Fig. 5-6). Perturbing such modes, for example by varying the radius of holes of an array (static steering) or by using phase-changed materials (dynamic steering), is a method to deflect emission beams without using additional components, such as phase arrays [10-12], liquid crystals [13], acousto-optics [14], or breaking the symmetry of the system to generate an artificial band-edge mode [9]. In this system, all holes have the same size in an array, and the required phase shift to steer the light is naturally provided by the phase-offset between Floquet-Bloch harmonics of the periodic structure (see Appendix 4). It is worth noting that the broken σ_z symmetry and the finite size of the realized samples limit the quality factor of modes 2 and 3 to very large but not infinite values, forming quasi-bound states in continuum [17].

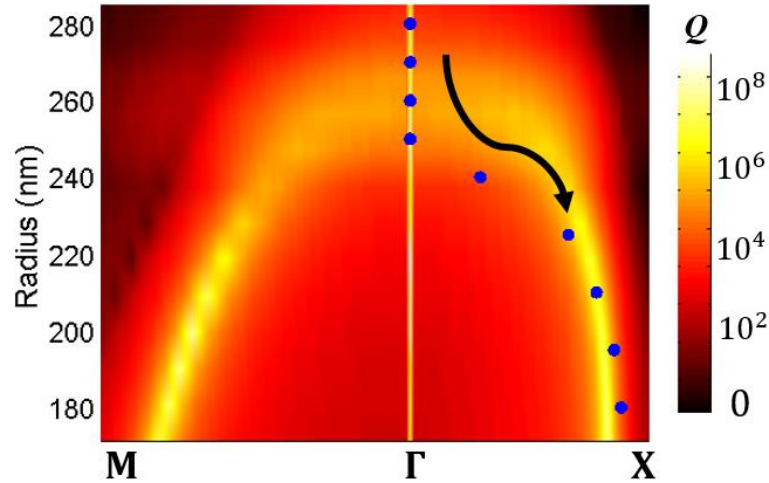


Figure 5-6 | Quality factor of modes 1-3 as a function of the radius of holes in reciprocal space (k-space). The quality factors of modes 1, 2 and 3 are singular in k-space, at a point for mode 1 (Γ -locked), and along lines for mode 2 (steering along ΓM) and mode 3 (steering along ΓX). Modes 2 and 3 can thus continuously steer as a function of the radius of holes. The quality factor of mode 1 is singular for all radii of holes because mode 1 is symmetry-protected while mode 2 and 3 become singular for holes radii smaller than $R \sim 250 \text{ nm}$. Blue dots correspond to steering prediction based on effective mode calculation (see Appendix 5).

5.3. Device Fabrication and Characterization

The sample is made of structured InGaAsP MQWs epitaxially grown on an InP substrate. The structure is fabricated by electron beam lithography followed by dry etching to form holes and thus constitutes a PhC. The PhC is subsequently bonded on a flat glass substrate coated with a thin layer of PMMA. During the bonding process, PMMA infiltrates holes of the PhC. Finally, the InP substrate is removed by wet etching using hydrochloric acid. Figure 5-7 shows a top SEM view of a device, illustrating the uniformity of

the holes in the structure. Several devices with a range of radius of holes were fabricated.

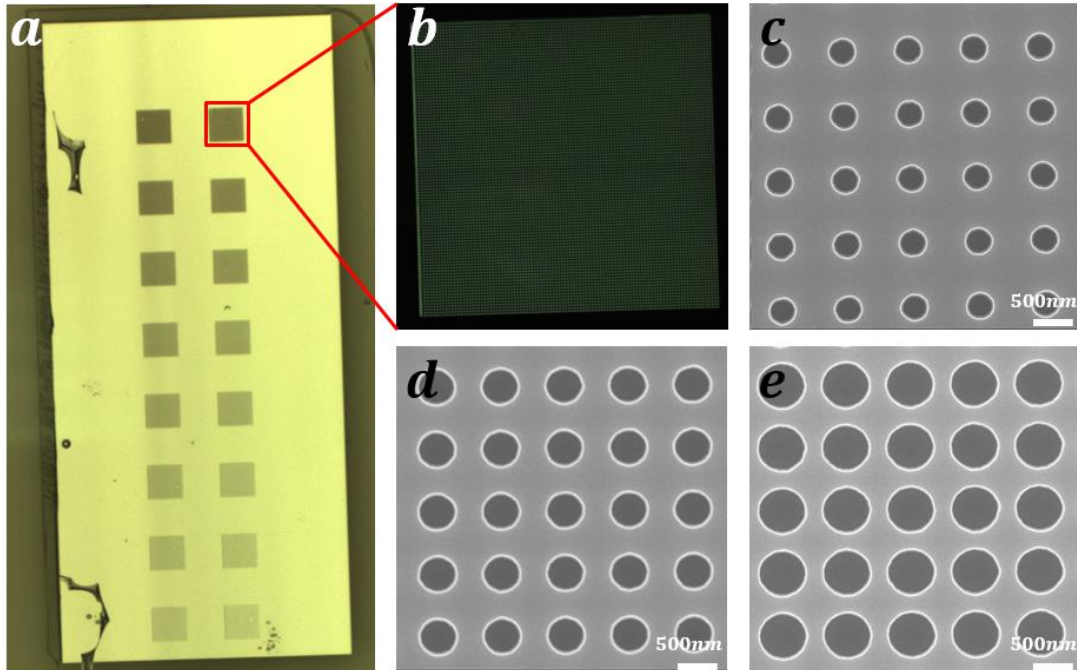


Figure 5-7 | (a) Microscope image of the fabricated PhC arrays. The sample contains different 200×200 arrays with the radii between $180 - 350 \text{ nm}$. The big pad (shiny surface) with all the arrays, is InGaAsP. Some InP residues are visible on the left side of the InGaAsP pad, but not on the arrays. (b) Dark field microscope image showing the zoom-in image of one of the arrays. (c-e) SEM image of the different arrays with different radii, 180 nm (c), 250 nm (d), and 350 nm (e).

5.4. Device Characterization

5.4.1. Photoluminescence Measurement

The measurements are performed using a micro-photoluminescence setup in which the reciprocal space is obtained by Fourier transforming the image plane (see Appendix 5). The devices are optically pumped with a pulsed

laser ($\lambda_{pump} = 1064 \text{ nm}$, $T = 12 \text{ ns}$ pulse at a repetition rate $f = 275 \text{ kHz}$).

The evolution of the output power as a function of the pump power (light-light curve) for a representative sample confirms the threshold behavior and a clear transition from spontaneous emission to lasing (Fig. 5-8).

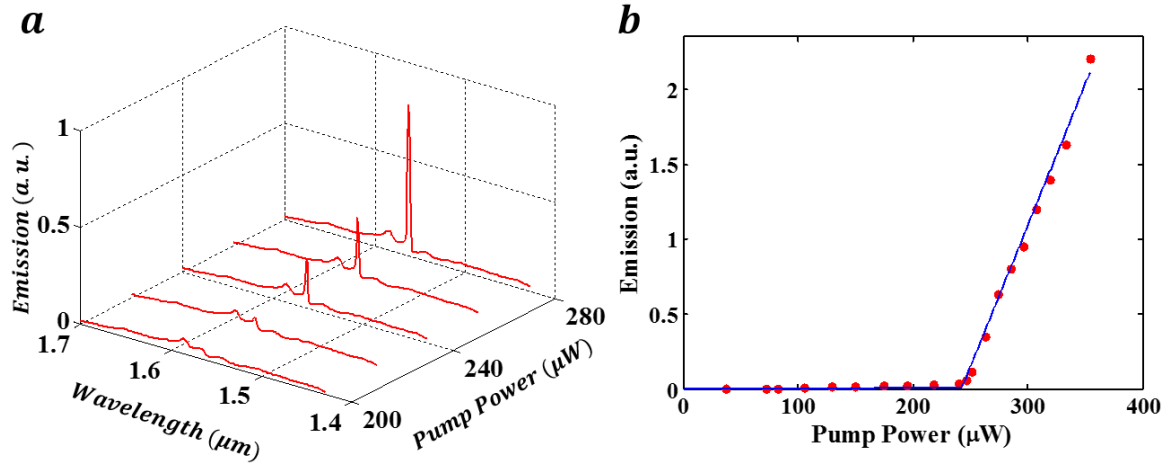


Figure 5-8 | (a) The emission power evolution as a function of the pump power in a broader wavelength range for a sample with a periodicity of $p = 950 \text{ nm}$, and radius of holes $r = 280 \text{ nm}$. By increasing the pump power, eventually, one mode starts to lase with reduced line-width. (b) Output power as a function of the average pump power (light-light curve) around the lasing wavelength. The red dots are experimental measurements of the output power for different pump powers. The blue solid lines are linear fits to the data in spontaneous and stimulated emission regimes and clearly show a threshold behavior, i.e. lasing.

5.4.2. Band Diagram Characterization

The band diagram of the device is experimentally measured by pumping the device with a high-energy laser and collecting the photoluminescence at different angles around the wavelength of $1.6 \mu\text{m}$. Figure 5-9 presents the band diagram measurement result (color plot) that is compared with

simulation (dotted points are from Fig. 5-4b), and there is a good agreement between theory and experiment.

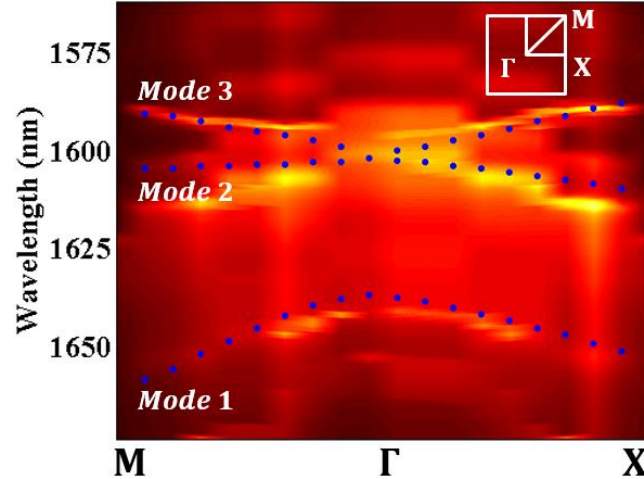


Figure 5-9 | Experimental (color plot) and theoretical (blue dots) band diagrams measured/calculated along the ΓX and the ΓM directions. The experimental band diagram is measured by pumping the structure with a high-energy laser and collecting the photoluminescence at different angles, and it is compared with theoretical calculations shown in Fig. 5-4a. A good agreement is observed between the theoretical band diagram and experiments.

5.4.3. Steering behavior

Figure 5-10 presents reciprocal space images of the emission of four samples with decreasing radii. The center of the image represents the center of the Brillouin zone i.e., $k_x = k_y = 0$ (Γ point). For $R = 250 \text{ nm}$, the PhC supports only the Γ -locked mode. Figure 5-10a confirms normal emission from this sample. As the radius is decreased below $R = 250 \text{ nm}$, the steering of four lasing beams along ΓX is observed. They correspond mode 3, which has a large quality factor along ΓX , and the four beams stem from the four-

fold symmetry of the crystal (invariance under 90° rotation). The number of beams can be controlled by the symmetry of the crystal as well as by boundary conditions (see Appendix 6). The steering angle further increases by decreasing the radius as seen in Fig. 5-10b-d. The emission angles are extracted from the reciprocal space images and the numerical aperture of the collecting objective.

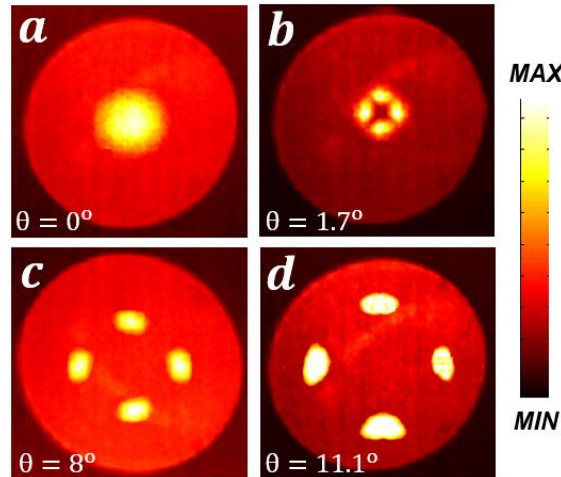


Figure 5-10 | Experimental k-space images of the emission from lasers with different radii. The distance of the bright spots to the center represents the in-plane wave-vector or equivalently the angle, and it increases as the radius of holes is decreased from $r = 250 \text{ nm}$ (a), to $r = 240 \text{ nm}$ (b), $r = 225 \text{ nm}$ (c), and $r = 190 \text{ nm}$ (d), clearly demonstrating the lasing angles of $\theta = 0^\circ$, $\theta = 1.7^\circ$, $\theta = 8^\circ$, and $\theta = 11.1^\circ$, respectively. The maximum observable angle in k-space imaging is given by the numerical aperture (NA) of the objective lens (NA = 0.4). The four-fold symmetry of the structure implies that any singularity is invariant under 90° rotation and this is confirmed by the four observed bright spots.

Blue dots in Fig. 3 represent the experimental emission angles, and as can be seen, lasing occurs in directions of predicted high quality factors. The

operating mode is selected by its spatial overlap with the optical gain and switches from mode 1 to mode 3 for $R \sim 250 \text{ nm}$ (see Appendix 5).

5.4.4. Polarization Vortex

Singular states resulting from full destructive interference carry a quantized topological charge (order of singularity) that can be controlled by the topology of the structure and mathematically refer to modes with singular far-field phase whose order can be identified by the far-field polarization twisting around the singular point in reciprocal space [15] or real space [18]. Figures 5-11a-f represent the experimental (a-c) and theoretical (d-f) far-fields of devices emitting at different angles. In these figures, all other three emission beams are filtered by using the knife-edge technique [19]. For $R = 180 \text{ nm}$ and $R = 225 \text{ nm}$, mode 3 (Γ X-beaming), emits at an angle with a tilted doughnut-shaped pattern confirming off-normal emission. For $R = 250 \text{ nm}$, only mode 1 (Γ -locked), emits with a doughnut-shaped far-field. To experimentally demonstrate the vortex nature of these emissions, we used a half-wave plate in combination with a linear polarizer in the path of the laser emission. Therefore, we observed a two-lobe intensity pattern (Fig. 5-11g-i), which refers to one time polarization winding (i.e., the topological charge of 1). By rotating the linear polarizer, the two-lobe pattern also rotates.

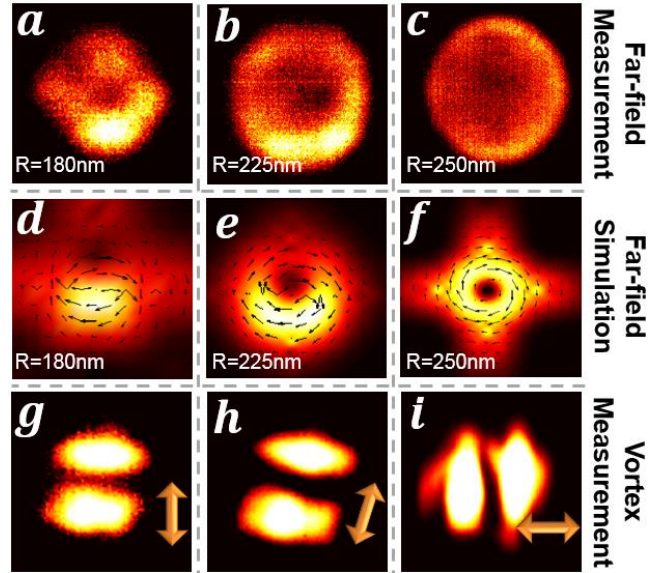


Figure 5-11 | Far-field radiation pattern measurements (a-c) and corresponding simulations (d-f) of the vortex lasers for three different radii, $r = 180 \text{ nm}$ (a,d), $r = 225 \text{ nm}$ (b,e), and $r = 250 \text{ nm}$ (c,f). By reducing the radius of holes, the far-field beam, which is doughnut-shaped, starts to beam. (g-i) Far-field intensity patterns of the emission beams after passing through a linear polarizer when the angle of the polarizer is (g) 0° , (h) 30° , and (i) 90° . Two-lobe pattern is due to the polarization twisting with the topological charge of 1.

5.4.5. Topological Charge Conservation

Singularities are always created in pairs due to charge conservation [15].

This is evident in Fig. 5-6 where a high quality factor mode that steers along ΓM is predicted. However, this mode was not observed so far as it experiences less effective gain than the ΓX -steering mode (see appendix 5). Since the existence of this mode is guaranteed by topology, it should be possible to observe lasing and steering along ΓM if the pump power is increased.

Figures 5-12 present the evolution of the reciprocal space image as a function of the pump power for samples supporting all three singular modes. For $R = 190 \text{ nm}$, Fig. 5-12a clearly shows lasing along ΓX . As the pump power is increased, four additional spots appear along ΓM (Fig. 5-12b-c). Similarly, for $R = 225 \text{ nm}$, additional spots appear (at a smaller angle) as the pump power is increased (Fig. 5-12d-f). These results demonstrate steering along ΓM . Normally at even higher pump powers lasing could be observed from mode 1 as well, but in our experiments, the threshold pump power of this mode was above the damage threshold of the InGaAsP MQWs. For the device to be a single mode laser with an independent steering angle, it would need to be operated below the threshold of mode 2.

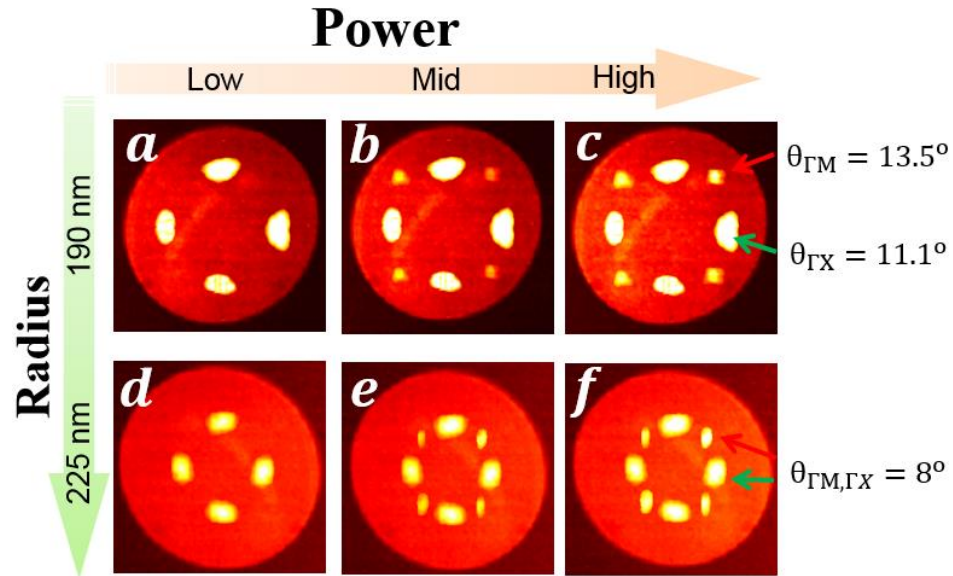


Figure 5-12 | Reciprocal space images of the vortex laser when the only mode lasing is the one beaming along ΓX (mode 3) (a,d). This mode has a topological charge of +1, and, topology guarantees the existence of another mode with the opposite charge in the system, as charges are created in pairs. As the power is increased, it reaches the threshold of the mode beaming along ΓM (mode 2) that also starts to lase (b,e) as evident from the four additional bright spots (four-fold symmetry) in k -space appearing at 45° to the previous lasing spots. Increasing the pump power further, increases the emission power of the lasing modes, making them brighter (c,f). In our system, the threshold of the mode steering along ΓM (mode 2) is larger than the threshold of the mode beaming along ΓX (mode 3). For pump powers smaller than the threshold of mode 2, the mode beaming along ΓX is the only mode lasing in the device. The relative threshold of the modes is governed by their effective gain that depends not only on the modes distribution in the device but also the gain spectrum of the MQWs. For $r = 190 \text{ nm}$, the emission angle of mode 2 is 13.5° and the emission angle of mode 3 is 11.1° . For $r = 225 \text{ nm}$, the emission angle of modes 2 and 3 is 8° , demonstrating beaming, both along ΓX and ΓM .

5.4.6. Wavelength Scaling

The modes can be further identified by their wavelength scaling. In Fig. 5-13, the continuous lines represent the theoretical prediction of the

wavelength of each mode with large quality factor as a function of the radius of holes. Dots represent

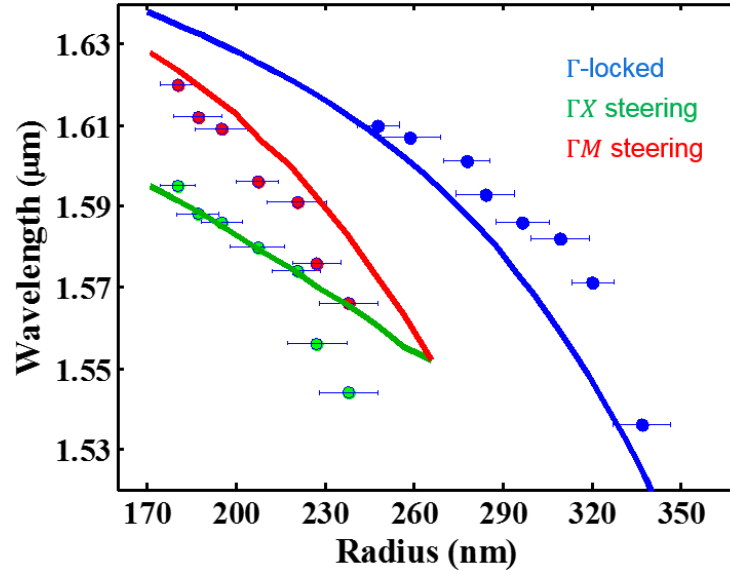


Figure 5-13 | Lasing wavelength as a function of the radius of holes from 180 nm to 350 nm. Each point corresponds to a device with a specific radius. Error bars indicate the standard deviation of radii measured from fabricated devices. Solid lines represent the wavelength of the singularities (resonances with large quality factor shown in Fig. 5-6) of mode 1 (blue), mode 2 (red), and mode 3 (green) for different radii of the holes. The good agreement between theory and experiment constitutes an additional identification of the modes.

measured wavelengths of emissions from the lasers and a good agreement with theory is observed.

5.5. Chapter Summary

In this chapter, we demonstrated topological light sources that generate and steer multiple coherent vortex beams. The devices are PhC arrays of holes made in InGaAsP MQWs that is bonded on a glass substrate using photoresist

of PMMA. All lasers operate at BIC singularities where destructive interference occurs between radiative channels of the PhC, and the required phase shift to steer the light is naturally provided by the phase offset between Floquet-Bloch harmonics of the periodic structure. By tuning the radius of holes continuously, the position of the BIC point moves along a line in direction of the crystal symmetry, which means that emission beams steer. For this, no additional mechanical component or breaking symmetry of the crystal is needed. BIC singularities carry non-zero topological charges. Thus beams are vortex beams with polarization windings that are proportional to the topological charge number. We also demonstrated that topological charges are created in pairs. Dynamic steering of the current device can be implemented using phase changed materials, which changes the refractive index continuously for a given radius of holes. The proposed scalable and steerable vortex light source paves the way to explore the new generation of light sources useful for optical tweezers with more flexibilities due to the non-mechanical platform and generation of tailored beams. Moreover, it can find applications in multiple other areas such as biological sensing, microscopy, astronomy, and high-capacity communications.

Chapter 5, in part, is a reprint of the material as it appears in B. Bahari, F. Vallini, T. Lepetit, R. Tellez-Limon, J. Park, A. Kodigala, Y. Fainman, and B. Kanté, “Integrated and steerable vortex lasers using bound states in continuum,” *arXiv:1707.00181* (2017), and B. Bahari, and B. Kanté, “Photonic generation and steering of coherent vortex beams,” United States patent (US Provisional Patent Application No. 62/506,765), 2016. The dissertation author was the primary researcher and author of this paper and patent.

References

1. A. Yariv, and P. Yeh, “Photonics: Optical Electronics in Modern Communications,” (6th edition, Oxford University Press, 2007).
2. K. Sakoda, “*Optical Properties of Photonic Crystals*,” (2nd edition, Springer, 2001).
3. J. D. Joannopoulos, S. G. Johnson, J. N. Winn, and R. D. Meade “*Photonic Crystals: Molding the Flow of Light*,” (2nd edition, Princeton University Press, 2008).
4. C. Jamois, R. B. Wehrspohn, J. Schilling, F. Muller, R. Hillebrand, and W. Hergert, “Silicon-based photonic crystal slabs: two concepts,” *IEEE Journal of Quantum Electronics* **38**, 805 (2002).
5. J. von Neumann, and E. Wigner, “On some peculiar discrete eigenvalues,” *Phys. Z.* **30**, 467 (1929).
6. D. C. Marinica, A. G. Borisov, and S. V. Shabanov, “Bound states in the continuum in photonics,” *Phys. Rev. Lett.* **100**, 183902 (2008).

7. C. W. Hsu, B. Zhen, J. Lee, S. L. Chua, S. G. Johnson, J. D. Joannopoulos, and M. Soljacic, "Observation of trapped light within the radiation continuum," *Nature* **499**, 188 (2013).
8. A. Kodigala, T. Lepetit, Q. Gu, B. Bahari, Y. Fainman, and B. Kante, "Lasing action from photonic bound states in continuum," *Nature* **541**, 196 (2017).
9. Y. Kurosaka, S. Iwahashi, Y. Liang, K. Sakai, E. Miyai, W. Kunishi, D. Ohnishi, and S. Noda, "On-chip beam-steering photonic-crystal lasers," *Nature Photonics* **4**, 447 (2010).
10. J. Sun, E. Timurdogan, A. Yaacobi, E. Shah Hosseini, and M. R. Watts, "Large-scale nanophotonic phased array," *Nature* **493**, 195 (2013).
11. H. Abediasl, and H. Hashemi, "Monolithic optical phased-array transceiver in a standard SOI CMOS process," *Opt. Exp.* **23**, 6509 (2015).
12. J. K. Doylend, M. J. R. Heck, J. T. Bovington, J. D. Peters, L. A. Coldren, and J. E. Bowers, "Two-dimensional free-space beam steering with an optical phased array on silicon-on-insulator," *Opt. Exp.* **19**, 21595 (2011).
13. P. McManamon, "An overview of optical phased array technology and status," *Proc. of SPIE* **5947**, 59470I-1 (2005).
14. J. Mur, B. Kavcic, and I. Poberaj, "Fast and precise Laguerre–Gaussian beam steering with acousto-optic deflectors," *Applied Optics* **52**, 6506 (2013).
15. N. D. Mermin, "The topological theory of defects in ordered media," *Rev. Mod. Phys.* **51**, 591 (1979).
16. B. Zhen, C. W. Hsu, L. Lu, A. D. Stone, and M. Soljacic, "Topological Nature of Optical Bound States in the Continuum," *Phys. Rev. Lett.* **113**, 257401 (2014).
17. H. Nakamura, N. Hatano, S. Garmon, and T. Petrosky, "Quasibound States in the Continuum in a Two Channel Quantum Wire with an Adatom," *Phys. Rev. Lett.* **99**, 210404 (2007).

18. C. Yang, Y. Chen, S. Wu, and Y. Fuh, "Independent Manipulation of Topological Charges and Polarization Patterns of Optical Vortices," *Scientific Reports* **6**, 31546 (2016).
19. M. A. C. de Araujo, R. Silva, E. de Lima, D. P. Pereira, and P. C. de Oliveira, "Measurement of Gaussian laser beam radius using the knife-edge technique: improvement on data analysis," *Applied Optics* **48**, 393 (2009).

Chapter 6: Summary and Outlook

In this thesis, we have studied, both theoretically and experimentally, a new type of light sources (lasers) based on topological singularities of, 1) Topological insulators (TIs), and 2) Bound states in the continuum (BIC). These topological behaviors are ubiquitous and, in every structure, ranging from a single particle to random and periodic systems. We studied the topological characteristics in periodic structures to design a new type of cavity resonators called topological cavities. Unlike conventional lasers that are based on semiconductor and cavity resonators to confine light with a large quality factor; topological cavities not only confine the light, but also manipulate the emission characteristics in different ways while giving the possibility of denser packaging.

The thesis started with topological insulators. We theoretically investigated topological structures using Quantum Hall effect, and numerically analyzed two-dimensional photonic systems. We designed topological waveguides using hybrid photonic crystals, and demonstrated that they are robust to any kind of disorders. Then, topological and non-topological (or conventional) cavities are studied and it was demonstrated that how

topology can be used as an extra degree of freedom to design robust non-reciprocal cavity resonators with smaller footprints and large isolation ratios.

Then we designed three-dimensional topological cavities using hybrid PhCs in an active platform for making integrated topological lasers. In our design, we used gain material of InGaAsP multiple quantum wells, which is a gain material at telecommunication wavelength range. We also used magnetic material of Yttrium Iron Garnet (YIG) to break time-reversal symmetry. Various topological cavities with arbitrary geometries are demonstrated. All cavities emit (in-plane) light in one direction with a sufficiently large isolation ratio (>10 dB).

The edge mode inside the topological cavities is leaky mode, which means that as it propagates inside the cavity, partially scatters out of it without using any secondary component such as gratings. We used this feature and removed the trivial waveguide in the previous design so that light can only emit in the normal direction. Therefore, unidirectional whispering gallery mode (WGM) emits outside generating orbital angular momentum (OAM) beam. The OAM beam carries a very large topological charge ℓ , same as WGM order m , i.e., $\ell = m$. We also demonstrated that it is possible to multiplex multiple of these topological cavities concentrically in a planar form

while each ring has different topological charge specified by the radius of ring. None of the multiplexed beam cross talk.

The second topological light source that we investigated is based on BIC singularities. We theoretically studied that BIC points are singularities in reciprocal space, and they have some unique topological characteristics. We demonstrated that BIC singularities are robust vortex centers (with non-zero topological charges) in the reciprocal space whose position can be tuned continuously. As a result, when it is designed in an active platform, we can make a topological light source that emits several vortex lights with tunable angles. Unlike conventional phase arrays that work based on controlling every single element in a system, in BIC lasers the required phase off-set between every unit cell of the PhC is provided by in-plane Floquet-Bloch waves. Therefore, by controlling the effective mode index of the PhC uniformly (either statically or dynamically) with a single knob, the emission beam can steer. Our experimental demonstration is useful for many applications, especially in the optical communications, fully non-mechanical LIDARs and optical tweezers.

Following to this thesis, there are few directions that worth to be explored in the future. Demonstration of the topological laser is very sensitive to fabrication and characterization process due to the small gyromagnetism of

the YIG material. Therefore, it has a quite challenging bonding process. Topological lasers are robust to any kind of in-plane disorder due to the full band gap in this direction. However, it is not robust to any vertical disorders. Any deviation in the normal direction such as non-uniform bonding, a wavy surface, or defect can remove the non-trivial band gap. As a result, it affects the functionality of the topological laser. To solve this problem, one possible solution is to enhance the gyromagnetism using magneto-optical metamaterials instead of YIG, because using this technique, the magnetization can enhance at least two orders of magnitudes.

Other interesting topological lasers are based on Quantum Spin-Hall effect. This kind of lasers require no magnetic material, and it is possible to open a larger band gap using this technique. As a result, they require fewer fabrication challenges and material losses. Thus the output power also can be enhanced to get high power lasers.

Regarding BIC lasers, one of its main advantages is steering beams using only one degree of freedom, i.e., detuning the effective refractive index of entire PhC uniformly. Thus using phase changed materials with a wide range of refractive index tunability can help to make dynamic steering. Furthermore, the lasers can be implemented electrically-pumped, which is more interesting in terms of practical applications, especially for LIDARs.

Appendix 1

A1.1. Other Arbitrary Geometry Cavities

Figure A1-1 shows the SEM images of the two different cavities with different random geometries.

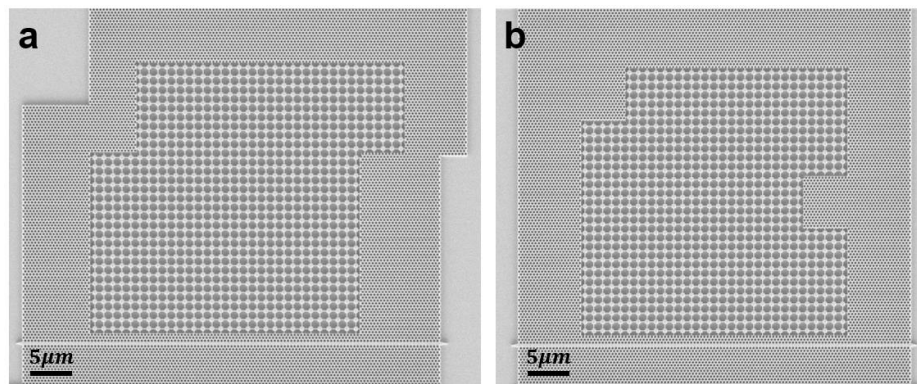


Figure A1-1 | (a,b) Top view SEM of a fabricated topological cavity with random geometry formed by the trivial and non-trivial PhCs. The optical length of the cavities is the same as the square cavity.

A1.2. Field Intensity Imaging

Figure A1-2 represents real space camera images of the surface of two different cavities shown in Fig. a1-1. As shown, when cavities are pumped in the presence of an EMF, edge modes are excited around the cavities nicely following the deformed edges of cavities.

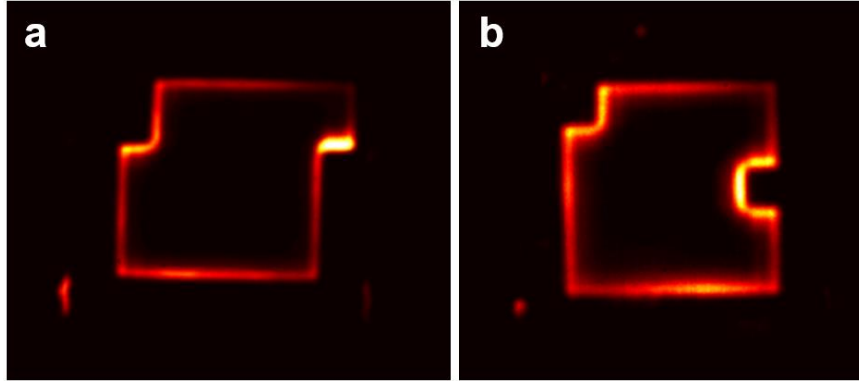


Figure A1-2 | IR camera image of two different cavities with arbitrary shapes shown in Fig. A1-1a (a), and Fig. A1-1b (b). Pumping cavities in the presence of an EMF leads to the excitation of edge modes around the cavities that nicely follows the contours of the deformed cavities.

A1.3. Photoluminescence Measurement

The emission spectrum for forward and backward biases of the EMF, and the isolation ratio for each of cavities (shown in Fig. A1-1) are presented in Fig. A1-3 and A1-4.

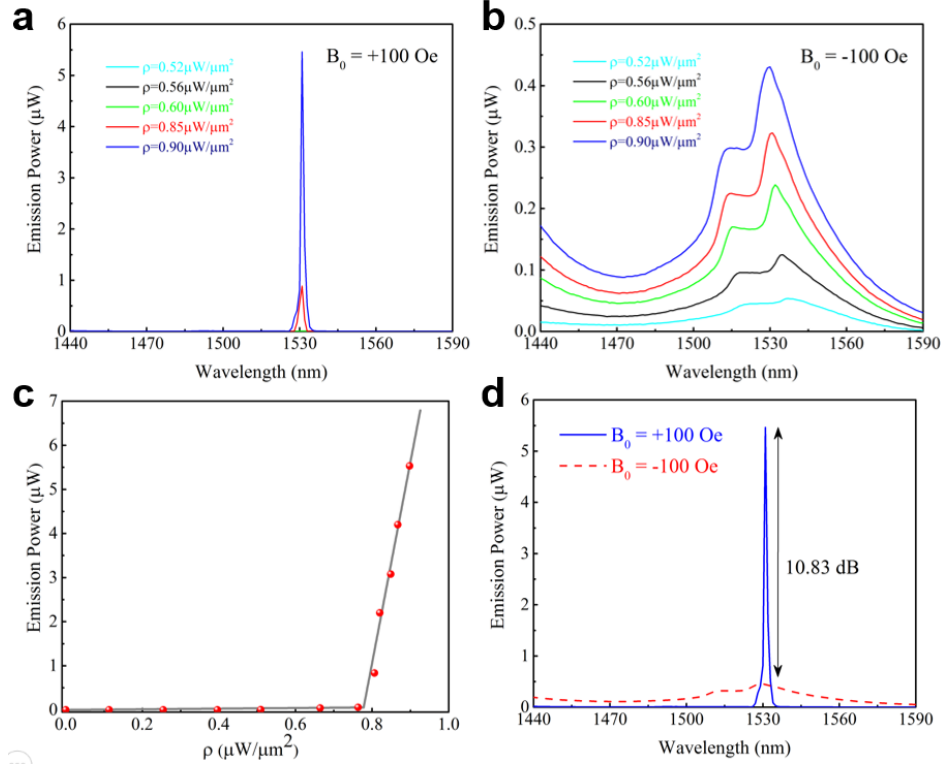


Figure A1-3 | Emission spectra of the cavity shown in Fig. A1-1a with an EMF of $B_0 = +100$ Oe (a), and $B_0 = -100$ Oe (b). (c) Evolution of the output power as a function of the pump power density. The red dots represent the experimental measurements of the output power for different pump power densities when the EMF is turned on ($B_0 = +100$ Oe). Gray solid lines represent linear fits to the data in spontaneous and stimulated emission regimes and clearly show a threshold behavior, i.e., lasing. (d) The isolation ratio between two ends of the waveguide is 10.83 dB.

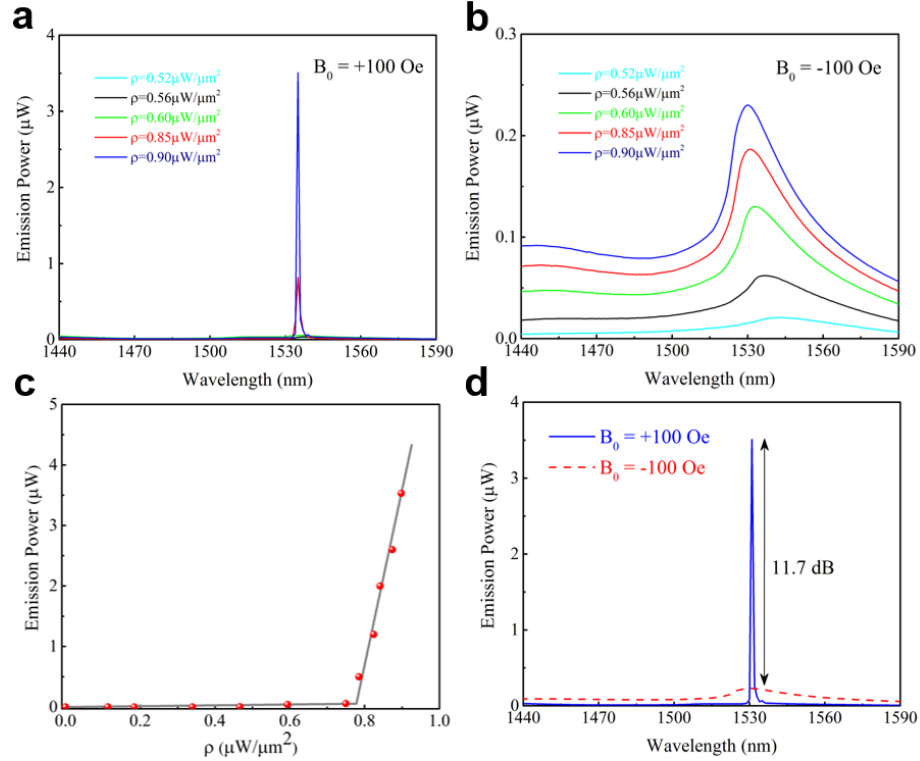


Figure A1-4 | Emission spectra of the cavity shown in Fig. 3-18b with an EMF of $B_0 = +100$ Oe (a), and $B_0 = -100$ Oe (b). (c) Evolution of the output power as a function of the pump power density. The red dots represent the experimental measurements of the output power for different pump power densities when the EMF is turned on ($B_0 = +100$ Oe). Gray solid lines represent linear fits to the data in spontaneous and stimulated emission regimes and clearly show a threshold behavior, i.e., lasing. (d) The isolation ratio between two ends of the waveguide is 11.7 dB.

Appendix 2

A2.1. Second Order Correlation Measurement

To characterize our topological lasers, we measured the second-order intensity correlation function, $g^2(\tau) = \frac{\langle I(t)I(t+\tau) \rangle}{\langle I(t) \rangle^2}$, with a Hanbury Brown-Twiss (HBT) interferometer. Here, $\langle I(t) \rangle$ represents the expectation value of the intensity at time t . Figure 4-9 in chapter 4 shows the experimental correlation histogram (Figs. 4-9a-e) and the corresponding normalized $g^2(\tau)$ (Fig. 4-9f-j) at five different pump power densities.

Due to nanosecond pulse pumping (290 kHz repetition rate, 6 ns pulse width), the correlation histogram inherently consists of many pulses corresponding to the optical pump pulses arriving, and the device is turning on. The time delay between neighboring pulses in Fig. 4-9a-e is approximately $3.4 \mu\text{s}$, which is consistent with the 290 kHz repetition rate of the pump laser. According to coherence theory, a photon bunching peak near zero-delay can be observed in $g^2(\tau)$ for a lasing device in the SpE and ASE regimes where the degree of coherence is low [1]. The width of the photon bunching peak is on the order of the coherence time [1], which is expected to be much smaller than the repetition period of the pump laser ($\sim 3.4 \mu\text{s}$). Therefore, the photon

bunching peak will emerge only on top of the zero-delay pulse, making it taller than the non-zero-delay pulses (Fig. 4-9b-d). In the lasing regime, such a photon bunching peak is suppressed since coherent emission is achieved [1]. This is clearly demonstrated in Fig. 4-9e.

The photon bunching peak can be more readily observed in the normalized $g^2(\tau)$, which is obtained by dividing the zero-delay pulse by the mean of the non-zero-delay pulses. The mean is taken here to reduce the effect of shot noise in the experiment. Figure 4-9f-j show examples of the normalized $g^2(\tau)$ in the SpE (Fig. 4-9f), ASE (Fig. 4-9g-i) and StE (Fig. 4-9j) regimes of our topological laser. Evidently, the photon bunching peak visible in the ASE regime is suppressed in the StE regime. However, contrary to theoretical predictions, the photon bunching is also absent in the SpE regime (Fig. 4-9a,f). This experimental phenomenon is primarily due to the timing uncertainty of our APDs', which is on the order of 100 ps. Since the coherence time in the SpE regime is much shorter than 100 ps, the averaging effect from the APDs renders the photon bunching peak invisible.

Figure 4-8 in chapter 4 was acquired by extracting the zero-delay value, i.e., $g^2(0)$, of the normalized $g^2(\tau)$ in a wide range of pump powers. By $g^2(0) \sim 1$ in both the SpE and StE regimes, confirms that our device indeed reached the lasing regime for two reasons. Firstly, the output power of our

device continued to increase even at the highest pump intensities. Hence, it's impossible that the device reverses back to the SpE regime due to, for example, degradation as that should lead to a significant decline in the output power.

References

1. R. Loudon, *The Quantum Theory of Light* (Oxford Univ. Press, New York, ed. 3, 2000).

Appendix 3

A3.1. Vortex Behavior of BIC Singularities

To analyze the structure, we used a finite-element simulation tool (COMSOL Multiphysics) to perform eigenmode calculations. Simulations are performed on a unit cell with periodic boundary conditions, and for every momentum (k_x, k_y) in the 1st Brillouin zone, the complex eigen-frequencies are computed. Figure A3-1 shows the quality factor map in the 1st Brillouin zone for all three modes shown in the chapter 5. Mode 1 has a large quality factor at the center of the 1st Brillouin zone (Γ point), while modes 2 and 3 have large quality factors along ΓM and ΓX directions, respectively.

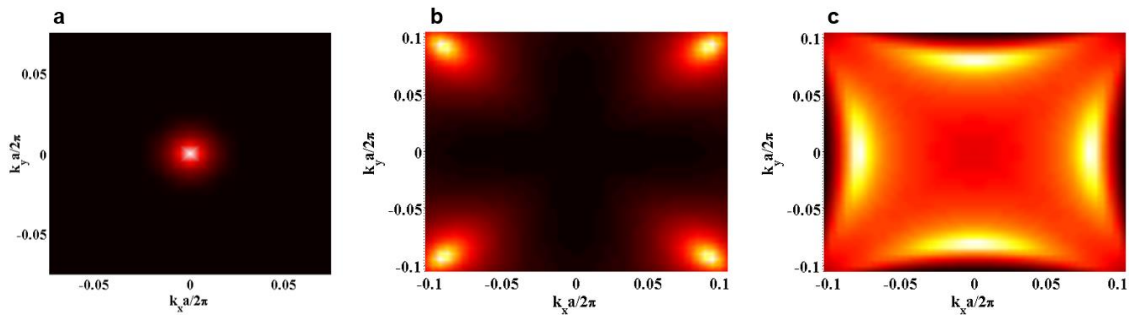


Figure A3-1 | Quality factor map in the Brillouin zone for modes 1 (a), 2 (b), and 3 (c). For the simulation, we used a unit cell with periodic boundary conditions in the xy -plane, and perfectly matched layers (PML) in the normal direction. The substrate is glass, while the cladding is air. PMMA used for bonding the InGaAsP onto glass and it infiltrates into the holes.

Far-field amplitudes and polarizations were extracted from simulations. To calculate the topological charge associated to a singular point, we use the far-field information to calculate the polarization rotation on any arbitrarily closed loop, which encloses the singular point in the Brillouin zone. The topological charge is calculated using eq. (5-3). The topological charges of -1, -1, and +1 were obtained for modes 1, 2, and 3, respectively.

From near-fields, the far-field was calculated by using near-to-far field transformation. Since we pumped uniformly a large area (more than 50×50), we repeated the unit cell field profile in a large area to emulate the experiment. It is important to note that the Floquet-Bloch phase, $e^{ik \cdot r}$, should be accounted for when repeating the unit cell field profile. Above $R = 250 \text{ nm}$, the laser is operating on mode 1, while below this radius it operates on mode 3. Figure A3-2 shows the far-field pattern of the laser in which mode 1 is emitting normal to the surface and is doughnut-shaped (Fig. A3-2a), while mode 3 is emitting at an angle, and is tilted doughnut-shaped (Fig. A3-2b).

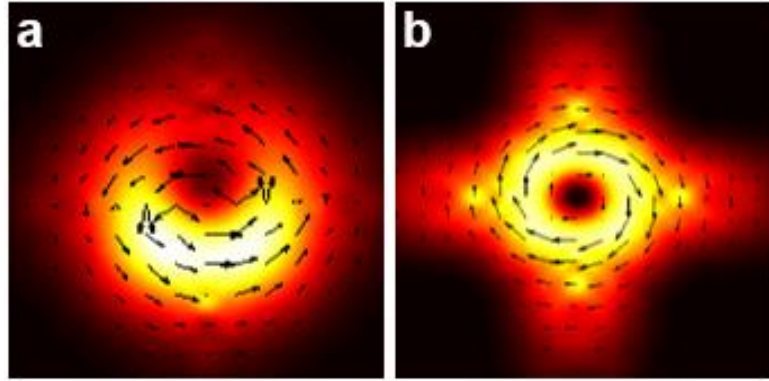


Figure A3-2 | Far-field patterns of the (a) mode 1, and (b) mode 3. To calculate the far-field profile, we extracted the near-field information from each eigenmode, and repeated it in a large area by taking into account of the Floquet-Bloch phase. Then by using near-to-far field transformation, the far-field patterns were calculated.

Appendix 4

A4.1. Rigorous Coupled Wave Analysis (RCWA)

To show the origin of BIC singularities due to the destructive interference of different Floquet-Bloch waves, we employ rigorous coupled wave analysis (RCWA) method [1]. Using RCWA, we can calculate all Floquet-Bloch waves and their relevant out-coupling coefficients inside the PhC slab.

The starting point is with Maxwell's equations:

$$\nabla \times E = -j\omega\mu \tilde{H}, \quad (\text{A4-1})$$

$$\nabla \times \tilde{H} = j\omega\epsilon E, \quad (\text{A4-2})$$

where $\tilde{H} = -j \sqrt{\frac{\mu_0}{\epsilon_0}} H$ is the normalized magnetic field. For a periodic structure along xy-plane, the material parameter can be express with the Fourier expansion

$$\epsilon_r(x, y) = \sum_{m=-\infty}^{\infty} \sum_{n=-\infty}^{\infty} a_{m,n} e^{j\left(\frac{m2\pi}{\Lambda_x}x + \frac{n2\pi}{\Lambda_y}y\right)}, \quad (\text{A4-3})$$

$$\mu_r(x, y) = \sum_{m=-\infty}^{\infty} \sum_{n=-\infty}^{\infty} b_{m,n} e^{j\left(\frac{m2\pi}{\Lambda_x}x + \frac{n2\pi}{\Lambda_y}y\right)}, \quad (\text{A4-4})$$

where Λ_x and Λ_y are periodicity along x and y directions respectively. $a_{m,n}$ and $b_{m,n}$ are the Fourier coefficients as

$$a_{m,n} = \frac{1}{\Lambda_x \Lambda_y} \int_{-\frac{\Lambda_x}{2}}^{\frac{\Lambda_x}{2}} \int_{-\frac{\Lambda_y}{2}}^{\frac{\Lambda_y}{2}} \epsilon_r(x, y) e^{-j\left(\frac{m2\pi}{\Lambda_x}x + \frac{n2\pi}{\Lambda_y}y\right)} dx dy, \quad (\text{A4-5})$$

$$b_{m,n} = \frac{1}{\Lambda_x \Lambda_y} \int_{-\frac{\Lambda_x}{2}}^{\frac{\Lambda_x}{2}} \int_{-\frac{\Lambda_y}{2}}^{\frac{\Lambda_y}{2}} \mu_r(x, y) e^{-j\left(\frac{m2\pi}{\Lambda_x}x + \frac{n2\pi}{\Lambda_y}y\right)} dx dy. \quad (\text{A4-6})$$

The Fourier expansion of the fields are

$$U_q(x, y, z) = \sum_{m=-\infty}^{\infty} \sum_{n=-\infty}^{\infty} S_q(m, n, z) e^{-j(k_x(m)x + k_y(n)y)}, \quad (\text{A4-7})$$

where $U = (E, H)$, $q = (x, y, z)$, $S = f$ for electric field ($U = E$) and $S = g$ for magnetic field ($U = H$), and the transverse components of the wave-vector are

$$k_x(m) = k_{x,inc} + \frac{m2\pi}{\Lambda_x}, \quad (\text{A4-8})$$

$$k_y(n) = k_{y,inc} + \frac{n2\pi}{\Lambda_y}. \quad (\text{A4-9})$$

We need longitudinal component of the wave-vector for: 1) calculating diffraction efficiencies, and 2) calculating the eigenmodes of homogeneous layer analytically. Thus

$$k_z(m, n) = \sqrt{\epsilon_r \mu_r k_0^2 + k_x^2(m) + k_y^2(n)}. \quad (\text{A4-10})$$

By substituting eq. (A54-10) into eq. (A4-1), (A4-2) and after some manipulation we find

$$\begin{aligned}
& -j\tilde{k}_y(n)g_z(m, n, \tilde{z}) - \frac{dg_y(m, n, \tilde{z})}{d\tilde{z}} = \\
& \sum_{q=-\infty}^{\infty} \sum_{r=-\infty}^{\infty} a_{m-q, n-r} f_x(q, r, \tilde{z}), \tag{A4-11}
\end{aligned}$$

$$\begin{aligned}
& \frac{dg_x(m, n, \tilde{z})}{d\tilde{z}} + j\tilde{k}_x(m)g_z(m, n, \tilde{z}) = \\
& \sum_{q=-\infty}^{\infty} \sum_{r=-\infty}^{\infty} a_{m-q, n-r} f_y(q, r, \tilde{z}), \tag{A4-12}
\end{aligned}$$

$$\begin{aligned}
& -j\tilde{k}_x(m)g_y(m, n, \tilde{z}) + j\tilde{k}_y(m)g_x(m, n, \tilde{z}) = \\
& \sum_{q=-\infty}^{\infty} \sum_{r=-\infty}^{\infty} a_{m-q, n-r} f_z(q, r, \tilde{z}), \tag{A4-13}
\end{aligned}$$

$$\begin{aligned}
& -j\tilde{k}_y(n)f_z(m, n, \tilde{z}) - \frac{df_y(m, n, \tilde{z})}{d\tilde{z}} = \\
& \sum_{q=-\infty}^{\infty} \sum_{r=-\infty}^{\infty} b_{m-q, n-r} g_x(q, r, \tilde{z}), \tag{A4-14}
\end{aligned}$$

$$\begin{aligned}
& \frac{df_x(m, n, \tilde{z})}{d} + j\tilde{k}_x(m)f_z(m, n, \tilde{z}) = \\
& \sum_{q=-\infty}^{\infty} \sum_{r=-\infty}^{\infty} b_{m-q, n-r} g_y(q, r, \tilde{z}), \tag{A4-15}
\end{aligned}$$

$$\begin{aligned}
& -j\tilde{k}_x(m)f_y(m, n, \tilde{z}) + j\tilde{k}_y(m)f_x(m, n, \tilde{z}) = \\
& \sum_{q=-\infty}^{\infty} \sum_{r=-\infty}^{\infty} b_{m-q, n-r} g_z(q, r, \tilde{z}), \tag{A4-16}
\end{aligned}$$

where $\tilde{k}_x = \frac{k_x}{k_0}$, $\tilde{k}_y = \frac{k_y}{k_0}$, $\tilde{k}_z = \frac{k_z}{k_0}$, $\tilde{z} = k_0 z$.

Starting with the first equation:

$$-j\tilde{\mathbf{K}}_y \mathbf{g}_z - \frac{d}{d\tilde{z}} \mathbf{g}_y = \llbracket \epsilon_r \rrbracket \mathbf{f}_x, \quad (\text{A4-17})$$

where

$$\tilde{\mathbf{K}}_y = \begin{bmatrix} \tilde{k}_y(1,1) & \cdots & 0 \\ \vdots & \ddots & \vdots \\ 0 & \cdots & \tilde{k}_y(M,N) \end{bmatrix}, \quad (\text{A4-18})$$

$$\mathbf{g}_z = \begin{bmatrix} g_z(1,1) \\ \vdots \\ g_z(M,N) \end{bmatrix}, \quad (\text{A4-19})$$

$$\mathbf{g}_y = \begin{bmatrix} g_y(1,1) \\ \vdots \\ g_y(M,N) \end{bmatrix}, \quad (\text{A4-20})$$

$$\mathbf{f}_x = \begin{bmatrix} f_x(1,1) \\ \vdots \\ f_x(M,N) \end{bmatrix}. \quad (\text{A4-21})$$

Same procedure is for the other equations

$$-j\tilde{\mathbf{K}}_y \mathbf{g}_z - \frac{d}{d\tilde{z}} \mathbf{g}_y = \llbracket \epsilon_r \rrbracket \mathbf{f}_x, \quad (\text{A4-22})$$

$$\frac{d}{d\tilde{z}} \mathbf{g}_x + j\tilde{\mathbf{K}}_x \mathbf{g}_z = \llbracket \epsilon_r \rrbracket \mathbf{f}_y, \quad (\text{A4-23})$$

$$\tilde{\mathbf{K}}_x \mathbf{g}_y - \tilde{\mathbf{K}}_y \mathbf{g}_x = j \llbracket \epsilon_r \rrbracket \mathbf{f}_z, \quad (\text{A4-24})$$

$$-j\tilde{\mathbf{K}}_y \mathbf{f}_z - \frac{d}{d\tilde{z}} \mathbf{f}_y = \llbracket \mu_r \rrbracket \mathbf{g}_x, \quad (\text{A4-25})$$

$$\frac{d}{d\tilde{z}}\mathbf{f}_x + j\tilde{\mathbf{K}}_x\mathbf{f}_z = \llbracket\mu_r\rrbracket\mathbf{g}_y, \quad (\text{A4-26})$$

$$\tilde{\mathbf{K}}_x\mathbf{f}_y - \tilde{\mathbf{K}}_y\mathbf{f}_x = j\llbracket\mu_r\rrbracket\mathbf{g}_z. \quad (\text{A4-27})$$

By eliminating longitudinal components, \mathbf{f}_z and \mathbf{g}_z

$$\tilde{\mathbf{K}}_y\llbracket\mu_r\rrbracket^{-1}(\tilde{\mathbf{K}}_x\mathbf{f}_y - \tilde{\mathbf{K}}_y\mathbf{f}_x) - \frac{d}{d\tilde{z}}\mathbf{g}_y = \llbracket\epsilon_r\rrbracket\mathbf{f}_x, \quad (\text{A4-28})$$

$$\frac{d}{d\tilde{z}}\mathbf{g}_x + \tilde{\mathbf{K}}_x\llbracket\mu_r\rrbracket^{-1}(\tilde{\mathbf{K}}_x\mathbf{f}_y - \tilde{\mathbf{K}}_y\mathbf{f}_x) = \llbracket\epsilon_r\rrbracket\mathbf{f}_y, \quad (\text{A4-29})$$

$$\tilde{\mathbf{K}}_y\llbracket\epsilon_r\rrbracket^{-1}(\tilde{\mathbf{K}}_x\mathbf{g}_y - \tilde{\mathbf{K}}_y\mathbf{g}_x) - \frac{d}{d\tilde{z}}\mathbf{f}_y = \llbracket\mu_r\rrbracket\mathbf{g}_x, \quad (\text{A4-30})$$

$$\frac{d}{d\tilde{z}}\mathbf{f}_x + \tilde{\mathbf{K}}_x\llbracket\epsilon_r\rrbracket^{-1}(\tilde{\mathbf{K}}_x\mathbf{g}_y - \tilde{\mathbf{K}}_y\mathbf{g}_x) = \llbracket\mu_r\rrbracket\mathbf{g}_y. \quad (\text{A4-31})$$

By manipulating these equations and writing in a matrix format

$$\frac{d}{d\tilde{z}}\begin{bmatrix} \mathbf{g}_x \\ \mathbf{g}_y \end{bmatrix} = \mathbf{Q}\begin{bmatrix} \mathbf{f}_x \\ \mathbf{f}_y \end{bmatrix}, \quad (\text{A4-32})$$

$$\frac{d}{d\tilde{z}}\begin{bmatrix} \mathbf{f}_x \\ \mathbf{f}_y \end{bmatrix} = \mathbf{P}\begin{bmatrix} \mathbf{g}_x \\ \mathbf{g}_y \end{bmatrix}, \quad (\text{A4-33})$$

where

$$\mathbf{Q} = \begin{bmatrix} \tilde{\mathbf{K}}_x\llbracket\mu_r\rrbracket^{-1}\tilde{\mathbf{K}}_y & \llbracket\epsilon_r\rrbracket - \tilde{\mathbf{K}}_x\llbracket\mu_r\rrbracket^{-1}\tilde{\mathbf{K}}_x \\ \tilde{\mathbf{K}}_y\llbracket\mu_r\rrbracket^{-1}\tilde{\mathbf{K}}_y - \llbracket\epsilon_r\rrbracket & -\tilde{\mathbf{K}}_y\llbracket\mu_r\rrbracket^{-1}\tilde{\mathbf{K}}_x \end{bmatrix}, \quad (\text{A4-34})$$

$$\mathbf{P} = \begin{bmatrix} \tilde{\mathbf{K}}_x\llbracket\epsilon_r\rrbracket^{-1}\tilde{\mathbf{K}}_y & \llbracket\mu_r\rrbracket - \tilde{\mathbf{K}}_x\llbracket\epsilon_r\rrbracket^{-1}\tilde{\mathbf{K}}_x \\ \tilde{\mathbf{K}}_y\llbracket\epsilon_r\rrbracket^{-1}\tilde{\mathbf{K}}_y - \llbracket\mu_r\rrbracket & -\tilde{\mathbf{K}}_y\llbracket\epsilon_r\rrbracket^{-1}\tilde{\mathbf{K}}_x \end{bmatrix}, \quad (\text{A4-35})$$

We can solve eq. (A4-32), (A4-33) as

$$\frac{d^2}{d\tilde{z}^2} \begin{bmatrix} f_x \\ f_y \end{bmatrix} = \mathbf{PQ} \begin{bmatrix} f_x \\ f_y \end{bmatrix}, \quad (\text{A4-36})$$

$$\frac{d^2}{d\tilde{z}^2} \begin{bmatrix} f_x \\ f_y \end{bmatrix} - \mathbf{\Omega}^2 \begin{bmatrix} f_x \\ f_y \end{bmatrix} = 0, \quad (\text{A4-37})$$

where $\mathbf{\Omega}^2 = \mathbf{PQ}$.

The solution of this equation is as

$$\begin{bmatrix} f_x(\tilde{z}) \\ f_y(\tilde{z}) \end{bmatrix} = e^{-\mathbf{\Omega}\tilde{z}} \mathbf{s}^+(0) + e^{\mathbf{\Omega}\tilde{z}} \mathbf{s}^-(0), \quad (\text{A4-38})$$

where $\mathbf{s}^+(0)$ and $\mathbf{s}^-(0)$ are trivial values for this differential equation, and \pm are indicating forward (+) and backward (−) propagations, and

$$e^{\mathbf{\Omega}\tilde{z}} = \mathbf{W}e^{\lambda\tilde{z}}\mathbf{W}^{-1}, \quad (\text{A4-39})$$

where \mathbf{W} and λ are Eigen-vector matrix and diagonal Eigen-value matrix calculated from $\mathbf{\Omega}^2$ matrix and

$$e^{\lambda\tilde{z}} = \begin{bmatrix} e^{\sqrt{\lambda_1^2}\tilde{z}} & \dots & 0 \\ \vdots & \ddots & \vdots \\ 0 & \dots & e^{\sqrt{\lambda_N^2}\tilde{z}} \end{bmatrix}. \quad (\text{A4-40})$$

Thus

$$\begin{bmatrix} f_x(\tilde{z}) \\ f_y(\tilde{z}) \end{bmatrix} = \mathbf{W}e^{-\lambda\tilde{z}} \mathbf{c}^+ + \mathbf{W}e^{\lambda\tilde{z}} \mathbf{c}^-, \quad (\text{A4-41})$$

where

$$\mathbf{c}^+ = \mathbf{W}^{-1}\mathbf{s}^+(0), \quad (\text{A4-42})$$

$$\mathbf{c}^- = \mathbf{W}^{-1}\mathbf{s}^-(0). \quad (\text{A4-43})$$

Similarly

$$\begin{bmatrix} g_x(\tilde{z}) \\ g_y(\tilde{z}) \end{bmatrix} = -\mathbf{V}e^{-\lambda\tilde{z}}\mathbf{c}^+ + \mathbf{V}e^{\lambda\tilde{z}}\mathbf{c}^-, \quad (\text{A4-44})$$

where $\mathbf{V} = \mathbf{Q}\mathbf{W}\lambda^{-1}$.

Combining two equations of (A4-41) and (A4-44) we have

$$\begin{bmatrix} f_x \\ f_y \\ g_x \\ g_y \end{bmatrix} = \begin{bmatrix} W & W \\ -V & V \end{bmatrix} \begin{bmatrix} e^{-\lambda\tilde{z}} & 0 \\ 0 & e^{\lambda\tilde{z}} \end{bmatrix} \begin{bmatrix} c^+ \\ c^- \end{bmatrix}, \quad (\text{A4-45})$$

By solving these equations, the amplitudes of different Floquet-Bloch waves (i.e., Fourier coefficients) are calculated. Figure A4-1 shows the quality factor for three modes along the irreducible Brillouin zone edges. When solving RCWA for modes exactly at BIC singularities, each pair of coefficients have the same amplitude but opposite phases, which results in destructive interference at the far-field.

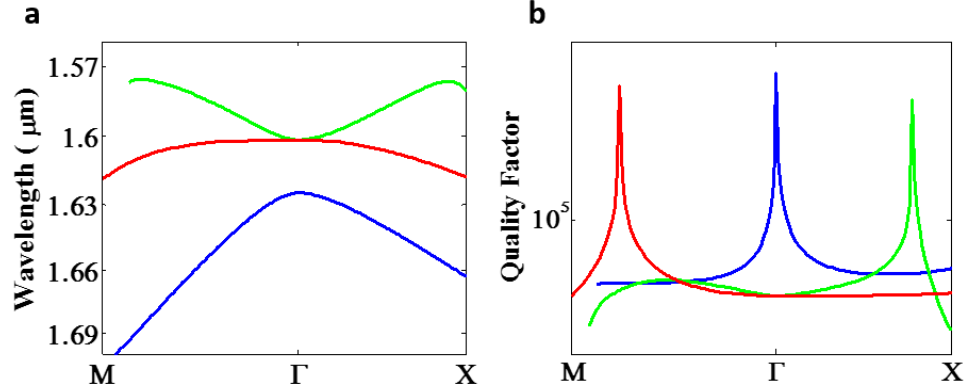


Figure A4-1 | (a) Dispersion band diagram and (b) quality factor of the PhC when the periodicity and radius of holes are 950 nm, and 200 nm, respectively.

For mode 1 (blue mode) right at BIC point (i.e., at Γ point), the Fourier coefficients are asymmetric (Fig. A4-2). It means that different Floquet-Bloch waves destructively interfere at the far-field resulting in a zero far-field intensity.

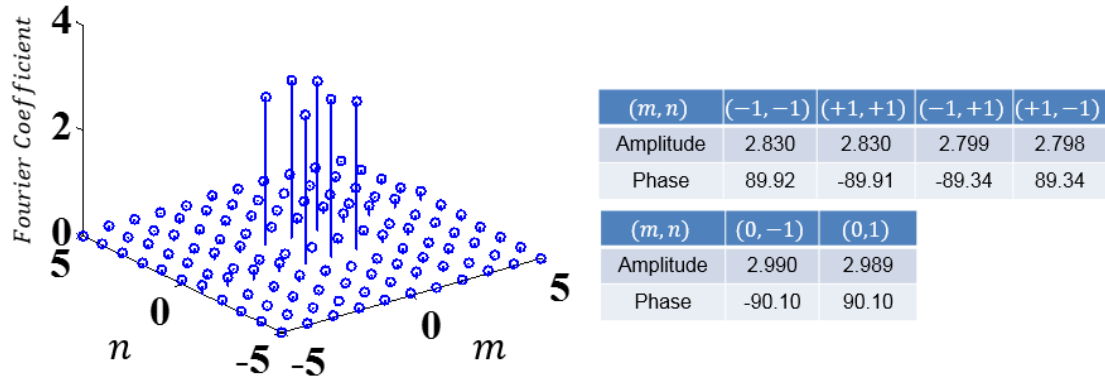


Figure A4-2 | Fourier coefficients of the mode 1 at Γ point. Amplitudes and phases of the dominant Floquet-Bloch waves are listed in the table. Clearly, each pair of the waves have the same amplitude but with π out-of-phase, resulting in destructive interference at the far-field.

Similarly for mode 3 (green mode), if we calculate Fourier coefficients for BIC point along ΓX direction, we find asymmetric coefficients (Fig. A4-3), but for a point away from BIC point the coefficients are not asymmetric

(Fig. A4-4). Therefore, at BIC point Floquet-Bloch waves destructively interfere at far-field, but away from BIC point, far-field is not zero.

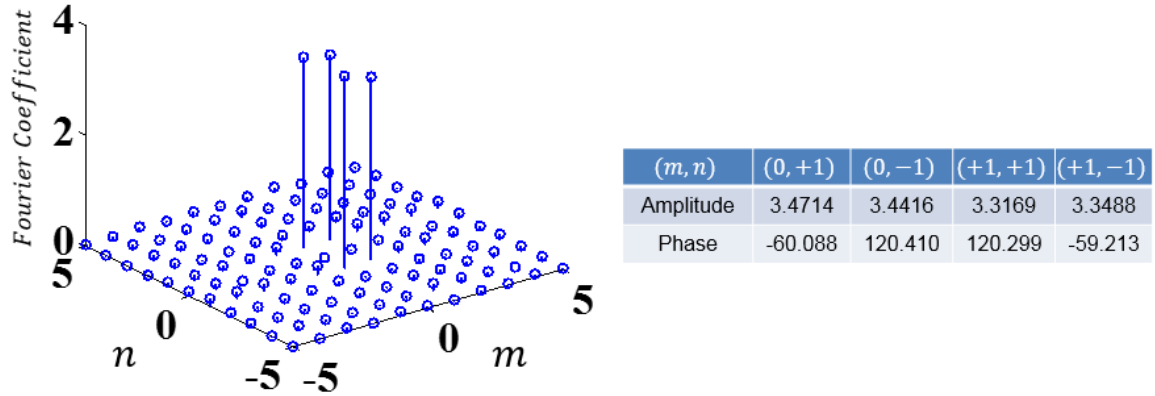


Figure A4-3 | Fourier coefficients of the mode 3 at BIC singularity along ΓX direction. Amplitudes and phases of the dominant Floquet-Bloch waves are listed in the table. Clearly, each pair of the waves have the same amplitude but with π out-of-phase, resulting in destructive interference at the far-field.

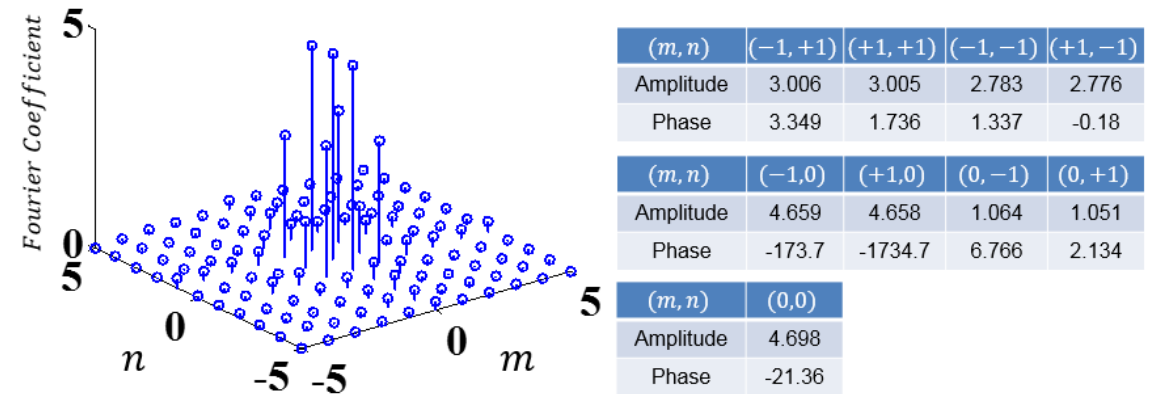


Figure A4-4 | Fourier coefficients of the mode 3 at a non-BIC point along ΓX direction. Amplitudes and phases of the dominant Floquet-Bloch waves are listed in the table. By choosing any of these sets, destructive interference does not happen, which means that far-field is not zero.

Reference

1. Moharam, M. G. & GaylordZhen, T. K. Rigorous coupled-wave analysis of planar-grating diffraction. *J. Opt. Soc. Am.* **71**, 811-818 (1981).

Appendix 5

A5.1. Experiment Setup

Figure A5-1 shows the schematic of the set-up used to characterize our samples. We use a high-energy laser source with a wavelength of 1064 nm as a pump beam to induce population inversion in the InGaAsP. By using an attenuator and a power detector, the power of the pump laser illuminating the sample is finely controlled. Also, the spot width of the pump laser, which initially is 3 mm², is reduced and collimated using two lenses (lenses 1 and 2) before reaching the objective lens. We use an objective lens with a numerical aperture and magnification of 0.4 and $\times 20$, respectively, to pump the sample and collect the emission simultaneously. The emitted power from the sample, which is in the wavelength range of 1400-1700 nm, is directed to the monochromator (CVI Digikrom DK480) in conjunction with a cooled InGaAs detector in lock-in detection configuration. In the same set-up, by using a removable mirror in the path of the emission beam, we can direct the light to an infrared camera for real space or reciprocal space imaging by putting the camera in the real plane or Fourier plane, respectively.

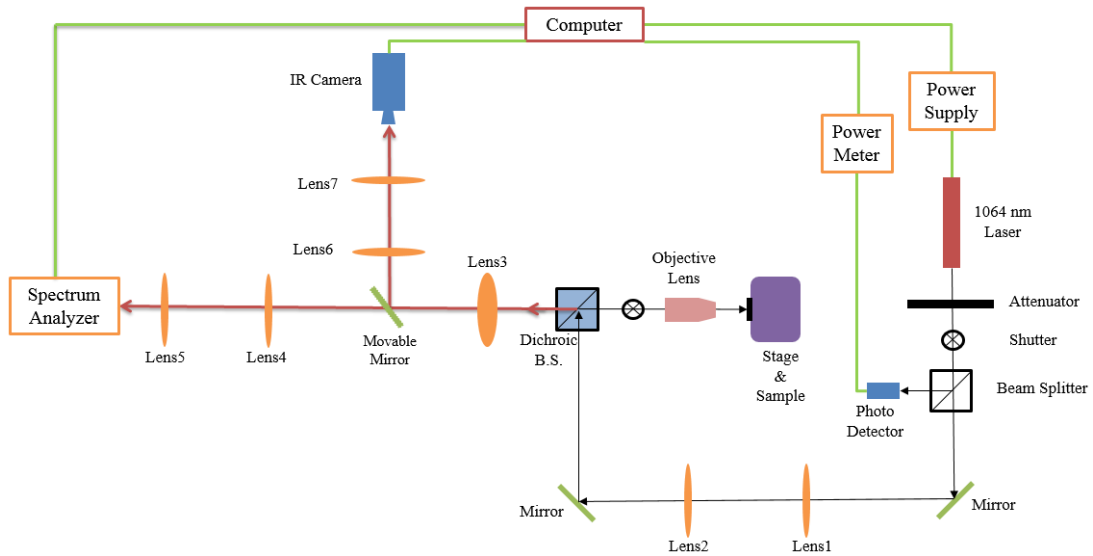


Figure A5-1 | Schematic of the set-up used for measurements. The incident pump power on the samples is finely controlled using a photodetector, and the emission from the samples is directed to a monochromator for photoluminescence measurements. Real space and reciprocal space imaging are performed by directing the emission toward the camera. The configuration shown in the figure is for real space imaging.

A5.2. Effective Mode Gain

For larger radii ($R > 250 \text{ nm}$), mode 1 is the only one with a large quality factor. However, for radii below $R = 250 \text{ nm}$, modes 2 and 3 also have large quality factors and gain competition then takes place. In the gain spectrum, mode 3 experiences more gain because it has a shorter wavelength compared to the other two modes, and mode 1 experiences less gain because it has a longer wavelength (Fig. A5-2a). Additionally, the field intensity confinement inside the gain material for mode 3 is larger than mode 1 and 2 (Fig. A5-2b), which ultimately results in a larger effective gain for mode 3

(Fig. A5-2c). Therefore, mode 3 lases with a smaller threshold power compared to the other modes. By increasing the pump power, mode 2 also starts lasing. However, the threshold power of mode 1 is comparable to the damage threshold of the gain material for small radii.

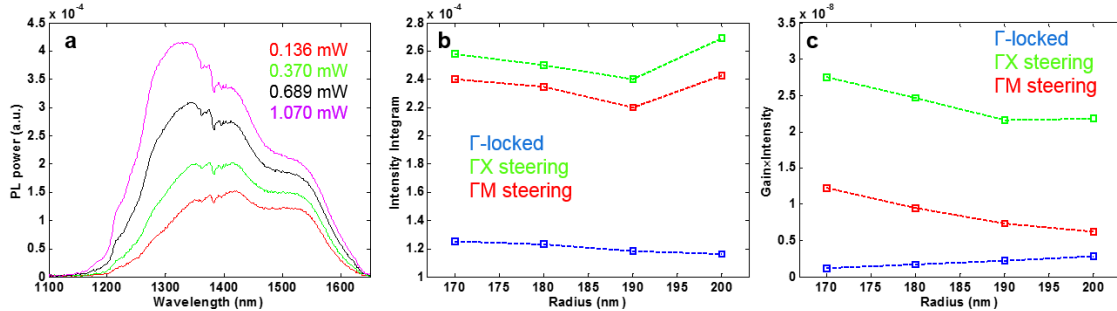


Figure A5-2 | (a) Gain spectrum measurement of the unpatterned InGaAsP, bonded on a glass substrate using PMMA, as a function of pump power. (b) Calculated integrated intensity of modes 1-3 inside the volume of the gain material (InGaAsP) in a unit cell. (c) Multiplication of the gain and the intensity of the field inside the gain material to evaluate the effective gain for modes 1-3. Mode 3 has larger effective gain than the other modes in a radius range of 170-200 nm, where all three modes have large quality factors.

A5.3. Far-field Patterns

Figure A5-3 shows far-field measurements for arrays with different radii. To measure the far-field pattern, we place the movable mirror, shown in Fig. A5-1, to direct the emission beam toward the camera. The measured far-field patterns agree with simulations shown in Fig. A3-2. By using a half-wave plate and a linear polarizer in the path of the emission beam, we observe a two-lobed intensity pattern that rotates by rotating the polarizer.

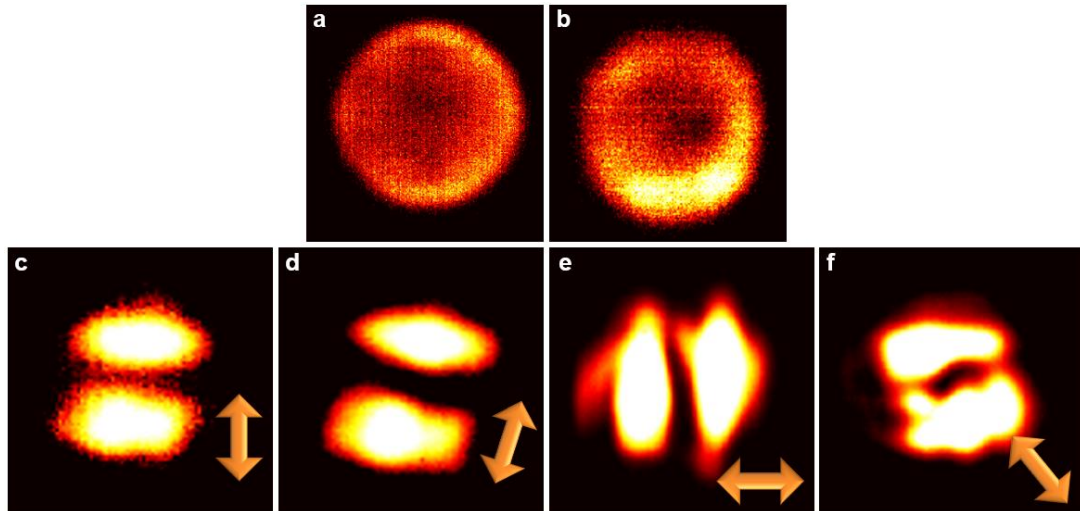


Figure A5-3 | Far-field measurements of two different arrays with radii of (a) 250 nm, and (b) 225 nm. To measure the far-field patterns, we put the movable mirror in the emission path to direct the beam to the camera. For the array with a radius of 250 nm (shown), the insertion of a half-wave plate and a linear polarizer in the emission path of the lasers with an angle of (c) 0° , (d) 30° , (e) 90° , and (f) -45° results in the observation of two-lobe shaped patterns coming from doughnut-shaped mode. The arrows in the inset show the direction of the polarizer.

Appendix 6

A6.1. Controlling the Number of beams using Boundaries

The fabricated arrays are quite large arrays with dimensions of 200×200 unit cells. The four-fold symmetry, i.e., invariance under 90° rotation implies that any singular state in reciprocal space must have the same symmetry. Consequently, four beams in the emission are observed (Fig. 5-10). However, by controlling, for example, the in-plane feedback between the Floquet-Bloch waves in certain directions we can actually control the number of beams. For instance, by choosing crystals with different symmetries/dimensionalities, e.g., 1D crystal, which is invariant under 180° rotation (two-fold symmetry), two beams instead of four beams should be observed. Another possible method, which we used here, is to control the in-plane feedback by bringing certain boundaries closer. We fabricated several arrays with different sizes of unit cells in x and y directions, 10×200 , 15×200 , and 25×200 . The in-plane feedback along the short direction is drastically reduced, almost suppressed, while it remains the same in the long direction.

It is worth noticing that emitted beams do not destructively interfere with each other to cancel the vortex because the four beams lasing along the four

equivalent ΓX directions carry the same topological charges but in four different directions. They are only canceled when the radius is close to the $R \sim 250 \text{ nm}$, and mode 2 (lasing along ΓM), which has the opposite topological charge, becomes degenerate with mode 3.

Figure A6-1 shows SEM images of arrays with different sizes.

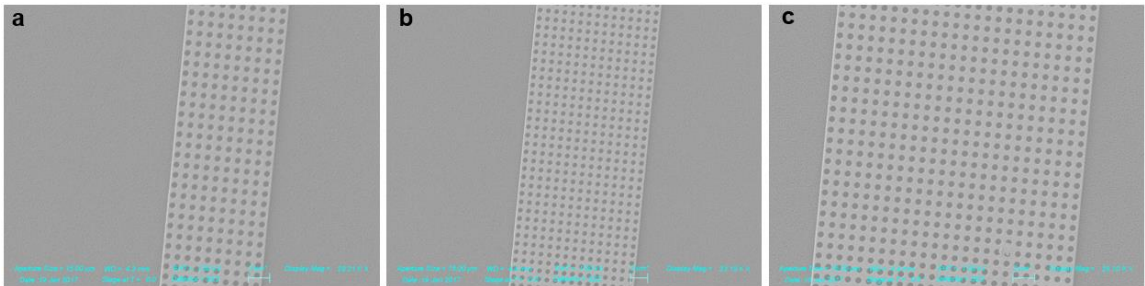


Figure A6-1 | SEM image of arrays with dimensions of (a) 10×200 , (b) 15×200 , and (c) 25×200 .

We performed reciprocal space imaging (Fig. A6-2), which reveals that for 10×200 , and 15×200 arrays there are only two beams rather than four beams along ΓX . However, arrays of 25×200 are large enough to induce sufficient in-plane feedback along both directions of periodicity to enable lasing.

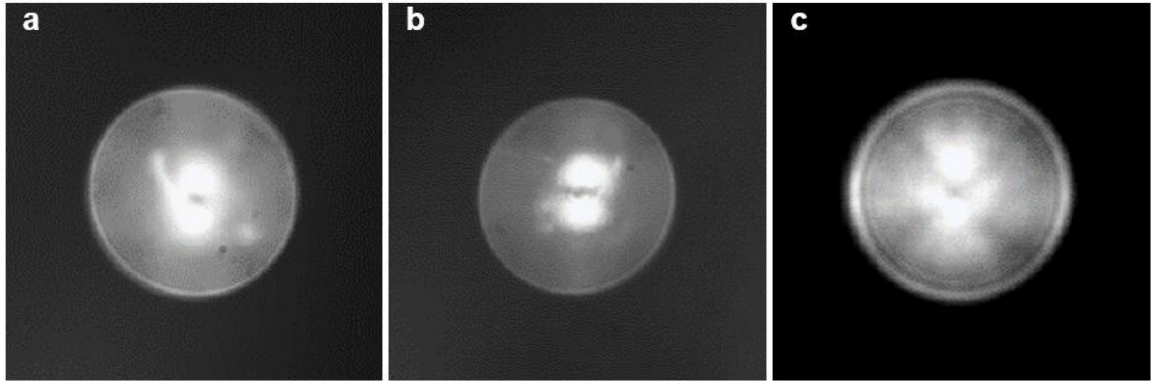


Figure A6-2 | Reciprocal space measurement for finite arrays with dimensions of (a) 10×200 , (b) 15×200 , and (c) 25×200 . The measurement was done by placing the camera in the Fourier plane. The imaging angle is limited by the numerical aperture (NA) of the objective lens ($NA=0.4$). For the arrays of 10×200 (a) and 15×200 (b) there are two beams along ΓX directions, but for the array of 25×200 (c) there are four beams along four equivalent ΓX directions. The two beams along the vertical axis are brighter than the other two along the horizontal axis. By increasing the size of the array (>25 unit cells), all the four spots tend to become the same.